

High Energy Resummation at Hadronic Colliders



Jack J. Medley

A thesis submitted in fulfilment of the requirements
for the degree of Doctor of Philosophy
to the
University of Edinburgh

March 2016

9 Abstract

10 Abstract abstract abstract abstract abstract abstract abstract abstract abstract
11 abstract abstract abstract abstract abstract abstract abstract abstract abstract
12 abstract abstract abstract abstract abstract abstract abstract abstract abstract
13 abstract abstract abstract abstract abstract abstract abstract abstract abstract
14 abstract abstract abstract abstract abstract abstract abstract abstract abstract
15 abstract abstract abstract abstract abstract abstract abstract abstract abstract
16 abstract abstract abstract abstract abstract abstract abstract abstract abstract
17 abstract abstract abstract abstract abstract abstract abstract abstract abstract
18 abstract abstract abstract abstract.

¹⁹ Declaration

²⁰ Except where otherwise stated, the research undertaken in this thesis was the unaided
²¹ work of the author. Where the work was done in collaboration with others, a significant
²² contribution was made by the author.

²³

J. Medley

²⁴

March 2016

²⁵ Acknowledgements

²⁶ Cheers guys!

Contents

²⁷	Abstract	i
²⁸	Declaration	ii
²⁹	Acknowledgements	iv
³⁰	Contents	vi
³¹	List of figures	x
³²	List of tables	xiii
³³		
³⁴	1 Introduction	1
³⁵	1.1 A Little History	1
³⁶	1.2 Thesis Outline	2
³⁷	2 Quantum Chromodynamics at hadronic colliders	5
³⁸	2.1 The QCD Lagrangian	5
³⁹	2.2 The Partonic Cross-Section	7
⁴⁰	2.3 Divergences and Regularisation	12
⁴¹	2.3.1 Ultraviolet divergences	12
⁴²	2.3.2 Infrared and collinear divergences	13
⁴³	2.3.3 Regularising divergences	14
⁴⁴	2.4 Renormalising the QCD Lagrangian	15
⁴⁵	2.5 The QCD Beta function	15
⁴⁶	2.6 QCD Factorisation at Hadronic Colliders	17
⁴⁷	2.7 From Partons to Jets	18
⁴⁸	2.8 Perturbative QCD and Resummation	20
⁴⁹	2.8.1 Fixed-order Perturbation	20
⁵⁰	2.8.2 An Example Fixed-Order Calculation	21
⁵¹	2.8.3 Resumming Higher-Order Corrections	34
⁵²	2.9 Parton showers for Monte-Carlo generators	34
⁵³	2.10 Spinor-Helicity Notation	34
⁵⁴	2.10.1 Spinor-Helicity Calculations with Massive Partons	35
⁵⁵	2.11 Monte Carlo Techniques	40
⁵⁶	2.11.1 One Dimensional Integration	40

57	2.11.2 Higher Dimensional Integration	42
58	2.11.3 Variation Reduction Techniques	43
59	3 High Energy QCD	49
60	3.1 The High Energy Limit of $2 \rightarrow 2$ QCD scattering	49
61	3.1.1 Mandelstam Variables in the High Energy Limit	49
62	3.1.2 HE limit of the three-gluon vertex	50
63	3.1.3 At Leading Order in α_s	50
64	3.1.4 At Next-to-Leading Order in α_s	51
65	3.1.5 High Energy Jets ‘Currents’	51
66	3.1.6 Effective Vertices For Real Emissions	51
67	3.2 High Energy Jets	51
68	3.2.1 The Multi-Regge Kinematic limit of QCD amplitudes	51
69	3.2.2 Logarithms in HEJ observables	51
70	3.2.3 HEJ currents	51
71	3.2.4 High Energy Phase-space Integration	51
72	4 Z/γ^*+Jets at the LHC	53
73	4.1 Z -jets	55
74	4.1.1 Formulation in terms of currents	58
75	4.1.2 To High Multiplicity Final States	58
76	4.1.3 Z^0 Emission Interference	58
77	4.1.4 Photonic Interference	58
78	4.1.5 The $2 \rightarrow n$ Matrix Element	58
79	4.1.6 The Differential Z/γ Cross-Section	58
80	4.2 Regularising the Z/γ^* +Jets Matrix Element	58
81	4.2.1 Soft Emissions	58
82	4.2.2 $V^2(q_{tj}, q_{t(j+1)})$ Terms	59
83	4.2.3 $V(q_{ti}, q_{t(i+1)}) \cdot V(q_{bi}, q_{b(i+1)})$ Terms	60
84	4.2.4 Integration of soft diverences	61
85	4.2.5 Virtual Emissions	62
86	4.2.6 Cancellation of Infrared Contributions	63
87	4.2.7 Example: $2 \rightarrow 4$ Scattering	66
88	4.3 Subtractions and the λ_{cut} scale	68
89	4.4 Z/γ^* +Jets at the ATLAS Experiment	68
90	4.4.1 CMS - Z + Jets Measurements	73
91	5 High Multiplicity Jets at ATLAS	77
92	6 The W^\pm to Z/γ^* Ratio at ATLAS	83
93	7 Z/γ^*+Jets at 100TeV	85
94	8 Conclusions and Outlook	93
95	A The Faddeev-Popov Trick	95

CONTENTS

96	Bibliography	97
97	Publications	100

CONTENTS

List of Figures

99	2.1	The evolution of α_s over several orders of magnitude in the scale of the process Q^2 . The data points fitted are of varying degrees of formal accuracy ranging from next-to-leading order in α_s (NLO) to next-to-next-to-next-to-leading order in α_s (N^3LO). Fig. from [20].	17
100	2.2	Simulations of the average number of jets as a function of the sum of the transverse momenta in the event, H_T , for inclusive dijets at a 7TeV LHC.	22
101	2.3	Feynman diagrams for calculating the $O(\alpha_s)$ correction to $\gamma^* \rightarrow q\bar{q}$. Fig. (2.3a) is the leading order contribution. Figs. (2.3b - 2.3d) are the virtual corrections and lastly figs. (2.3e - 2.3f) are the real emission contributions.	23
102	2.4	A simple importance sampling example (see equation 2.126). The integrand, $f(x)$, is shown in blue, the importance sampling distribution is shown in green and, for comparison, the uniform probability density function used in the naive case of no importance sampling is also shown (in red).	45
103	2.5	The absolute value squared of the Z^0 propagator for a range of values of the invariant mass squared of the Z^0 , p_Z^2 . We can see it is strongly peaked at the Z^0 mass and, as such, is an ideal candidate for using importance sampling.	46
104	2.6	Recent parton distribution function fits from the HERA experiment. The observed variation in $f(x_{a/b}, Q^2)$, especially at high $x_{a/b}$, can be exploited when computing the equation ?? by using an importance sampling approach	47
105	4.1	The possible emission sites for a neutral weak boson.	56
106	4.2	Examples of diagrams contributing to $2 \rightarrow 4$ scattering. In fig. 4.2a the p_2 has been drawn with a dashed line to denote it is not resolvable. In fig. 4.2b the final state momenta have been labelled in a seemingly strange way - this was done to make clear the cancellation when working through the algebra.	67
107	4.3	The effect of varying λ_{cut} on the differential distribution in the rapidity gap between the two leading jets in p_\perp with the $N_{jet} = 2, 3, 4$ exclusive selections shown from left to right. $\lambda_{cut} = 0.2$ (red), 0.5 (blue), 1.0 (green), 2.0 (purple).	69

LIST OF FIGURES

131 4.4	These plots show the inclusive jet rates from (a) HEJ and (b) other theory descriptions and data [3]. HEJ events all contain at least two jets and do not contain matching for 5 jets and above, so these bins are not shown.	72
135 4.5	These plots show the invariant mass between the leading and second-leading jet in p_T . As in Fig. 4.4, predictions are shown from (a) HEJ and (b) other theory descriptions and data [3]. These studies will inform Higgs plus dijets analyses, where cuts are usually applied to select events with large m_{12}	72
140 4.10	The transverse momentum distribution of the third hardest jet in inclusive dijet events in [51], compared to (a) the predictions from HEJ and (b) the predictions from other theory descriptions.	74
143 4.6	The comparison of (a) HEJ and (b) other theoretical descriptions and data [3] to the distribution of the absolute rapidity different between the two leading jets. HEJ and Blackhat+Sherpa give the best description. .	75
146 4.7	These plots show the differential cross section in the ratio of the leading and second leading jet in p_T from (a) HEJ and (b) other theory descriptions and data [3].	75
149 4.8	The inclusive jet rates as given by (a) the HEJ description and (b) by other theoretical descriptions, both plots compared to the CMS data in [51].	76
152 4.9	The transverse momentum distribution of the second hardest jet in inclusive dijet events in [51], compared to (a) the predictions from HEJ and (b) the predictions from other theory descriptions.	76
155 5.1	78
156 5.2	78
157 5.3	79
158 5.4	79
159 5.5	80
160 5.6	80
161 5.7	81
162 5.8	81
163 7.1	12a	87
164 7.2	12a	88
165 7.3	11a	89
166 7.4	11b	90
167 7.5	91
168 7.6	92

List of Tables

169	1.1	The fermion content of the standard model.	2
170	2.1	A graphical summary of the Feynman rules. The solid lines indicate a fermion (anti-fermion) propagator with momentum flowing parallel (anti-parallel) to the direction of the arrow. Similarly for the dashed lines which represent the ghost (anti-ghost) propagating and lastly the twisted lines depict a propagating gluon. As in the preceding equations i and j represent fundamental colour indices, a and b represent adjoint colour indices and, where present, f and f' represent fermion flavour. All Greek indices are Lorentz indices.	10
171	2.2	The Monte-Carlo approximation to equation 2.126 as we vary the number of sampled points, N , shown in the naive sampling case and in the importance sampled case.	44
172	4.1	The total cross-sections for the 2, 3 and 4 jet exclusive rates with associated statistical errors shown for different values of the regularisation parameter λ_{cut} . The scale choice was the half the sum over all traverse scales in the event, $H_T/2$	68
173	4.2	Cuts applied to theory simulations in the ATLAS Z -plus-jets analysis results shown in Figs. 4.4–4.7.	70
174	4.3	Cuts applied to theory simulations in the CMS Z -plus-jets analysis results shown in Figs. 4.8–4.10	73
175			
176			
177			
178			
179			
180			
181			
182			
183			
184			
185			
186			
187			
188			
189			

¹⁹⁰ **Chapter 1**

¹⁹¹ **Introduction**

¹⁹² **1.1 A Little History**

¹⁹³ The Standard Model is a gauge quantum field theory describing three of the four
¹⁹⁴ observed fundamental forces - with the inclusion of gravity remaining elusive. Its local
¹⁹⁵ gauge structure is given by:

$$SU(3)_c \times SU(2)_L \times U(1)_Y. \quad (1.1)$$

¹⁹⁶ The subscripts on the groups are simply a convenient notation. The ‘c’ on $SU(3)$
¹⁹⁷ indicates that it is the strong ‘colour’ coupling being described. The ‘L’ on $SU(2)$
¹⁹⁸ indicates that all right-handed states are in the trivial representation of the group
¹⁹⁹ and the ‘Y’ on the $U(1)$ indicates that this is the hypercharge group and not the
²⁰⁰ electromagnetic group. The $SU(3)_c$ group describes the strong nuclear force (Quantum
²⁰¹ Chromodynamics or QCD) and its 8 gauge generators give us the massless spin-1 gluons,
²⁰² $G_a^\mu(x)$, $a = 1, \dots, 8$, present in the standard model. There are three weak boson states,
²⁰³ $W_a^\mu(s)$, $a = 1, \dots, 3$, associated with the $SU(2)_L$ group and a further one, $B^\mu(x)$, which
²⁰⁴ comes from the $U(1)_Y$ group.

²⁰⁵ The only remaining boson to complete the standard model arises from the complex
²⁰⁶ scalar Higgs field whose ground state is not invariant under the action of $SU(2)_L \times$
²⁰⁷ $U(1)_Y$. This field breaks the standard model gauge symmetry to

$$SU(3)_c \times U(1)_{em}, \quad (1.2)$$

where the $U(1)_{em}$ refers to the electromagnetic charge. After this ‘Spontaneous Symmetry Breaking’ occurs three of the four aforementioned bosons, $W_a^\mu(s)$ and $B^\mu(x)$ acquire mass and combinations of them are physically realised as the experimentally observer electroweak boson; The massive states W^\pm, Z^0 and the massless photon, γ . The photon and the Z^0 bosons are of particular importance in the work that follows.

The fundamental particle content of the Standard Model also includes fermions. These are spin-1/2 particles which obey the spin-statistics theorem (and hence the Pauli exclusion principle) and comprise, along with the gluons which binds the nucleus together, all known visible matter in the universe. The fermions are structured in three so-called ‘generations’, shown in tab. 1.1 and can be further subdivided into quarks and leptons. Quarks are colour triplets under QCD but are also charged under the electroweak group. The up (u), charm (c) and top (t) quarks have electric charge $+\frac{2}{3}$ while the down (d), strange (s) and bottom (b) quarks have $-\frac{1}{3}$. Leptons are singlets under $SU(3)$ and so do not couple to the strong sector. The charged leptons e, μ and τ have electric charge -1 and the neutrinos are neutral.

	First Generation	Second Generation	Third Generation
Quarks	u, d	c, s	$t,$
Leptons	e, ν_e	μ, ν_μ	τ, ν_τ

Table 1.1: The fermion content of the standard model.

1.2 Thesis Outline

The aim of this thesis is to detail the importance of a certain class of perurbatively higher-order terms in events with QCD radiation in the final state. In particular we will consider corrections to parton-parton collisions with a Z^0 or γ in association with high energy QCD radiation in the final state.

In chapter 2 I will begin by introducing quantum chromodynamics, the theory of the strong sector in the standard model, and detail how we might use this to calculate physical observables (such as cross-sections and differential distributions) at hadron colliders such as the Large Hadron Collider. I will discuss how these observables fall prey to divergences in QCD-like quantum field theories with massless states and mention briefly how such divergences can be handled. I will then describe how the computationally expensive integrals derived in subsequent chapters may be efficiently evaluated using Monte-Carlo techniques.

In chapter 3 the details of QCD in the ‘High Energy’ limit are discussed. After

237 completing a few instructive calculations we will see how, in this limit, the traditional
238 fixed-order perturbation theory view of calculating cross-sections fades as another
239 subset of terms, namely the ‘Leading Logarithmic’ terms in $\frac{s}{t}$, become more important.
240 I will discuss previous work in the High Energy limit of QCD and how this can be used to
241 factorise complex parton-parton scattering amplitudes into combinations of ‘currents’
242 which, when combined with gauge-invariant effective gluon emission terms can be used
243 to construct approximate high-multiplicity matrix elements.

244 In chapter 4 the work of the previous chapter is extended to the case where there is
245 a massive Z^0 boson or an off-shell photon, γ^* , in the final state. A ‘current’ for this
246 process is derived and the complexities arising from two separate sources of interference
247 are explored. This new result for the matrix element is compared to the results obtained
248 from a Leading Order (in the strong coupling, α_s) generator **MadGraph** at the level of the
249 matrix element squared in wide regions of phase space is seen to be in exact agreement.
250 This result must then be regularised to treat the divergences discussed in chapter 2 and
251 this process is presented. The procedure for matching this regularised result to Leading
252 Order results is shown and the importance of the inclusion of these non-resummation
253 terms is discussed. Lastly three comparisons of the High Energy Jets Z+Jets Monte-
254 Carlo generator to recent experimental studies **ATLAS** and **CMS** at the LHC are shown.

255 From here we use the results of chapter 4, and the resulting publicly available Monte
256 Carlo package, to compare our description to a recent experimental prediction of the
257 ratio of the $W^\pm + \text{jets}$ rate to the $Z/\gamma^* + \text{jets}$ rate. Our predictions are compared against
258 next-to-leading order (in α_s) results from **NJet** and leading order results from **MadGraph**.

259 In chapter ?? we apply the massive spinor-helicity to the production of a $t\bar{t}$ pair in
260 hadronic collisions. Using the **PySpinor** package we calculate values for the full-mass
261 matrix element and compare them to leading-order (in α_s) results from **MadGraph**. This
262 is a process in which the leading logarithmic contribution starts at one order higher
263 than in previous work and so the effects of the resummation are not as expected to be as
264 crucial as in the case of chapter 4 - however at large values for the centre-of-mass energy
265 (such as that a future high energy circular collider) these ‘next-to-leading’ logarithms
266 will once again lead to the breakdown of fixed-order perturbation theory.

267 In chapter 5 we discuss the results of a lengthy study of jet production from the **ATLAS**
268 collaboration. This analysis was a thorough look at BFKL-like dynamics in proton-
269 proton colliders and the HEJ predictions are seen to describe the data well in the
270 regions of phase-space where we know the effects of our resummation become relevant.
271 We compare the predictions from both standalone HEJ and HEJ interfaced with
272 **ARIADNE**, a parton shower based on a dipole-cascade model. Although the interface to

- 273 ARIADNE increases the computational complexity significantly; we see that the Sudakov
274 logarithms added by significantly improve the description of data.
- 275 In chapter 7, with a study of $Z/\gamma^* + \text{Jets}$ at a centre-of-mass energy of 100TeV relevant
276 for the discussion of the next wave of high energy particle physics experiments (such
277 as any Future Circular Collider) which are of great interest to the community at large.
278 We see that the higher-order perturbative terms are much larger at 100TeV relative to
279 7TeV data and predictions. Moreover, the regions of phase-space relevant for this thesis;
280 that of high energy wide-angle QCD radiation is especially enhanced and, therefore
281 resumming these contributions will be essential for precision physics at any ‘Future
282 Circular Collider’.
- 283 Finally, in chapter 8 I summarise the results of the above chapters and provide a short
284 outlook for future work.

²⁸⁵ **Chapter 2**

²⁸⁶ **Quantum Chromodynamics at
hadronic colliders**

²⁸⁸ **2.1 The QCD Lagrangian**

²⁸⁹ We obtain the QCD Lagrangian by considering the spin- $\frac{1}{2}$ Dirac Lagrangian for the
²⁹⁰ case of a fermionic fields ψ each with mass m :

$$\mathcal{L}_D = \bar{\psi}_i (i\cancel{D} - m)_{ij} \psi_j, \quad (2.1)$$

²⁹¹ where ψ_i is itself a vector of 3 fermion fields in the fundamental representation of $SU(3)$
²⁹² with $i = 1, \dots, 3^1$. This is manifestly invariant under the *global* $SU(3)$ transformation

$$\psi_i \rightarrow e^{i\alpha^a T_{ij}^a} \psi_j \quad (2.2)$$

²⁹³ where $a = 1, \dots, 8$, α^a are constant and T^a are the generators of the $SU(3)$ group. We
²⁹⁴ choose to promote this *global* symmetry to a *local* one by relaxing the constraint that
²⁹⁵ α^a are constant and instead allow them to depend on a space-time coordinate i.e.

$$\alpha^a = \alpha^a(x^\mu). \quad (2.3)$$

¹The choice of 3 here is, again, well experimentally verified. Here we will work explicitly with the gauge group $SU(3)$ although many of the results which follow can be derived with a more general special unitary group $SU(N_c)$.

²⁹⁶ This breaks the $SU(3)$ symmetry but we can recover the required invariance by
²⁹⁷ replacing the usual partial derivative term with a ‘covariant derivative’ defined by:

$$\mathcal{D}_{ij}^\mu = \partial_{ij}^\mu - ig_s A^{\mu a} T_{ij}^a, \quad (2.4)$$

²⁹⁸ where g_s is the QCD coupling constant and A_μ^a is the QCD gauge field associated with
²⁹⁹ the gluon. With this replacement the local $SU(3)$ invariance of eq. (2.1) is recovered.
³⁰⁰ We must also include the effect of the kinetic term for the gluon field in our theory.
³⁰¹ We do this by considering the field-strength tensor for A_μ^a , $F_{\mu\nu}^a$ which is given by:

$$F_{\mu\nu}^a = \partial_\mu A_\nu^a - \partial_\nu A_\mu^a + g_s f^{abc} A_\mu^b A_\nu^c \quad (2.5)$$

³⁰² where f^{abc} are constants which define the algebra of the $SU(3)$ group and are given by

$$T^a T^b - T^b T^a = i f^{abc} T^c. \quad (2.6)$$

³⁰³ eq. (2.6) is what makes QCD fundamentally different from Quantum Electrodynamics
³⁰⁴ (QED): the simple fact that the generators of the underlying group *do not* commute
³⁰⁵ makes performing calculations in QCD significantly more complicated than it’s Abelian
³⁰⁶ cousin QED.

³⁰⁷ In summary then, the QCD Lagrangian is given by

$$\mathcal{L}_{\text{QCD (classical)}} = -\frac{1}{4} F_{\mu\nu}^a F^{a\mu\nu} + \sum_{f=1}^6 \bar{\psi}_i^{(f)} (i \not{D} - m_f)_{ij} \psi_j^{(f)}, \quad (2.7)$$

³⁰⁸ where we have now generalised to the experimentally proven case of 6 ‘flavours’ of quark
³⁰⁹ in our model (outlined previously in tab. (1.1)). This is referred to as the ‘classical’
³¹⁰ QCD Lagrangian since we have not included quantum effects such as loop corrections.
³¹¹ The full ‘quantum’ Lagrangian is as follows [57]:

$$\mathcal{L}_{\text{QCD}} = \sum_{f=1}^6 \bar{\psi}_i^{(f)} (i \not{D}^{ij} - m_f)_{ij} \psi_j^{(f)} - \frac{1}{4} F_{\mu\nu}^a F^{a\mu\nu} - \frac{(\partial^\mu A_\mu^a)^2}{2\xi} + (\partial^\mu \bar{c}^a) \mathcal{D}_\mu^{ab} c^b, \quad (2.8)$$

³¹² where \mathcal{D}_μ is the covariant derivative in the adjoint representation given by

$$\mathcal{D}_\mu^{ab} = \delta^{ab}\partial_\mu - g_s f^{abc} A_\mu^c. \quad (2.9)$$

313 The final two terms arise from the treatment of a degeneracy in the QCD path integral
 314 which is caused by the gauge symmetry we enforced earlier - as a result we are only
 315 able to define a gluon propagator once we have “fixed the gauge” which is achieved by
 316 the penultimate term in eq. (2.8). ξ is a free parameter in this process and, as we will
 317 see when we come to define the gluon propagator, it’s choice *defines* a specific gauge
 318 (see Appendix A). The final term is a mathematical quirk of this process and c and
 319 \bar{c} represent the resulting QCD “ghost” and “anti-ghost” fields respectively. They are
 320 unphysical since they are spin-1 anti-commuting fields.

321 2.2 The Partonic Cross-Section

322 Now we have a complete Lagrangian for QCD we can begin to move towards physical
 323 observables. The first step towards this is the Lehman-Symanzik-Zimmerman (LSZ)
 324 reduction formula. This gives us a relation between the scattering amplitude from some
 325 initial state into some final state, $\langle f|i\rangle \equiv \langle f|S|i\rangle$ where S is the scattering matrix, and
 326 a time-ordered vacuum expectation operator of a product of fields. Here we briefly
 327 present the argument behind the LSZ formula for the case of $2 \rightarrow 2$ scattering using
 328 scalar phi-cubed theory for simplicity (but this generalises to more complex theories).
 329 The Lagrangian for this theory is given by:

$$\mathcal{L}_{\text{phi-cubed}} = \frac{1}{2}\partial^\mu\phi\partial_\mu\phi + \frac{m^2}{2}\phi^2 - \frac{g}{6}\phi^3. \quad (2.10)$$

330 We can Fourier expand the field, $\phi(x)$, in terms of its annihilation and creating operators
 331 as follows:

$$\phi(x) = \int \frac{d^4k}{2E(2\pi)^3} \left(a(\vec{k})e^{ik\cdot x} + a^\dagger(\vec{k})e^{-ik\cdot x} \right), \quad (2.11)$$

332 and inverting this we find the following form for the creation operator $a^\dagger(\vec{k})$:

$$a^\dagger(\vec{k}) = i \int d^3x e^{-ix\cdot k} (\partial_0 - E) \phi(x), \quad (2.12)$$

333 We expect that as time flows forward to $+\infty$ (or backwards to $-\infty$) the field, $\phi(x)$,

³³⁴ become asymptotically free and therefore we can neglect any interaction effects in these
³³⁵ extremes. From eq. (2.12) it is straightforward to show that:

$$a^\dagger(\vec{k}, t = \infty) - a^\dagger(\vec{k}, t = -\infty) = i \int d^4x e^{-ix \cdot k} (\partial^2 + m^2) \phi(x). \quad (2.13)$$

³³⁶ Clearly this would be zero if we only consider the free theory where $g = 0$ in eq. (2.10)
³³⁷ - intuitively this is correct since once we remove any interaction terms a state we create
³³⁸ at $t = -\infty$ should flow to $t = \infty$ unaltered. However, more generally for an interacting
³³⁹ theory it will be non-zero and eq. (2.13) gives us a relationship between asymptotically
³⁴⁰ free initial and final states. Using eq. (2.13) (and its hermitian conjugate) we can begin
³⁴¹ to look at the scattering from a 2 particle initial state $|i\rangle$ to some 2 particle final state
³⁴² $|f\rangle$, $k_1 + k_2 \rightarrow k'_1 + k'_2$, this is given by:

$$\langle i|j\rangle \equiv \langle 0|T \left(a(k'_1, \infty) a(k'_2, \infty) a^\dagger(k'_1, -\infty) a^\dagger(k'_2, -\infty) \right) |0\rangle, \quad (2.14)$$

³⁴³ where T denotes the time-ordered product of operators. After substituting for the a
³⁴⁴ and a^\dagger operators and seeing that the time-ordering means that all of the remaining
³⁴⁵ annihilation/creation operators end up acting on a vacuum state which they annihilate
³⁴⁶ we are left with:

$$\begin{aligned} \langle i|j\rangle = i^4 \int d^4x'_1 d^4x'_2 d^4x_1 d^4x_2 & e^{ik'_1 \cdot x'_1} (\partial_{x'_1}^2 + m^2) e^{ik'_2 \cdot x'_2} (\partial_{x'_2}^2 + m^2) \times \\ & e^{ik_1 \cdot x_1} (\partial_{x_1}^2 + m^2) e^{ik_2 \cdot x_2} (\partial_{x_2}^2 + m^2) \times \\ & \langle 0|T (\phi(x'_1)\phi(x'_2)\phi(x_1)\phi(x_2)) |0\rangle. \end{aligned}$$

³⁴⁷ This is the LSZ reduction formula for $2 \rightarrow 2$ scattering in a phi-cubed theory. It reduces
³⁴⁸ the problem of finding scattering amplitudes to the calculation of time-ordered problem
³⁴⁹ of fields under the assumption that we may treat the fields at $t = \pm\infty$ as free.
³⁵⁰ The next step is to see how we can calculate these time-ordered products. This is most
³⁵¹ conveniently done by taking functional derivatives of the QCD path integral given by:

$$\mathcal{Z}[J, \eta, \bar{\eta}, \chi, \bar{\chi}] = \int \mathcal{D}A \mathcal{D}\psi \mathcal{D}\bar{\psi} \mathcal{D}c \mathcal{D}\bar{c} e^{i \int d^4x (\mathcal{L}_{QCD} + A^{a\mu} J_\mu^a + \bar{\psi}^a \eta^a + \bar{\eta}^a \psi^a + \bar{c}^a \chi^a + \bar{\chi}^a c^a)}, \quad (2.15)$$

³⁵² where $J^{a\mu}$, η^a , $\bar{\eta}^a$, χ^a and $\bar{\chi}^a$ are ‘source’ terms which we target with functional

353 derivatives and we have left the sum over quark flavours implicit. In order to proceed
 354 we break down eq. (2.1) into a free Lagrangian, $\mathcal{L}_{\text{QCD},0}$, and an interacting Lagrangian,
 355 $\mathcal{L}_{\text{QCD},I}$ as follows:

$$\begin{aligned}
 \mathcal{L}_{\text{QCD}} &= \mathcal{L}_{\text{QCD},0} + \mathcal{L}_{\text{QCD},I}, \\
 \mathcal{L}_{\text{QCD},0} &= \bar{\psi}_i (i\cancel{\partial} - m)_{ij} \psi_j - \frac{1}{4} (\partial_\mu A_\nu^a - \partial_\nu A_\mu^a) (\partial^\mu A^\nu{}^a - \partial^\nu A^\mu{}^a) \\
 &\quad - \frac{(\partial^\mu A_\mu^a)^2}{2\xi} + (\partial^\mu \bar{c}^a) (\partial_\mu c^a), \\
 \mathcal{L}_{\text{QCD},I} &= g_s \bar{\psi}^i T_{ij}^a \gamma^\mu \psi^j - \frac{g_s}{2} f^{abc} (\partial_\mu A_\nu^a - \partial_\nu A_\mu^a) A^{b\mu} A^{c\nu} \\
 &\quad - \frac{g_s^2}{4} f^{abe} f^{cde} A_\mu^a A_\nu^b A^{c\mu} A^{d\nu} - g_s f^{abc} \partial^\mu \bar{c}^a c^b A_\mu^c.
 \end{aligned}$$

356 We can then rewrite eq. (2.15) as a combination of functional derivatives acting on the
 357 free QCD path integral, \mathcal{Z}_0 as:

$$\begin{aligned}
 \mathcal{Z}[J, \eta, \bar{\eta}, \chi, \bar{\chi}] &= \exp \left[i \int d^4x \mathcal{L}_{\text{QCD},I} \left(\frac{\delta}{i\delta J^{\mu a}}, \frac{\delta}{i\delta \eta^a}, \frac{\delta}{i\delta \bar{\eta}^a}, \frac{\delta}{i\delta \xi^a}, \frac{\delta}{i\delta \bar{\xi}^a} \right) \right] \\
 &\quad \times \mathcal{Z}_0[J, \eta, \bar{\eta}, \chi, \bar{\chi}],
 \end{aligned} \tag{2.16}$$

358 where \mathcal{Z}_0 is identical to eq. (2.15) but with the free Lagrangian, in place of the full
 359 Lagrangian. We can solve \mathcal{Z}_0 exactly which yields us the propagators for the gluons,
 360 quarks and ghosts. Respectively:

$$\langle 0 | A_a^\mu(x) A_b^\nu(y) | 0 \rangle = \int \frac{d^4k}{(2\pi)^4} e^{-ik \cdot (x-y)} \delta_{ab} \frac{i}{k^2} \left(g^{\mu\nu} - (1-\xi) \frac{k^\mu k^\nu}{k^2} \right), \tag{2.17a}$$

$$\langle 0 | \bar{\psi}_i^{(f)}(x) \psi_j^{(f')}(y) | 0 \rangle = \int \frac{d^4k}{(2\pi)^4} e^{-ik \cdot (x-y)} \delta_{ij} \delta_{ff'} \frac{i(\not{k} + m)}{k^2 - m^2}, \tag{2.17b}$$

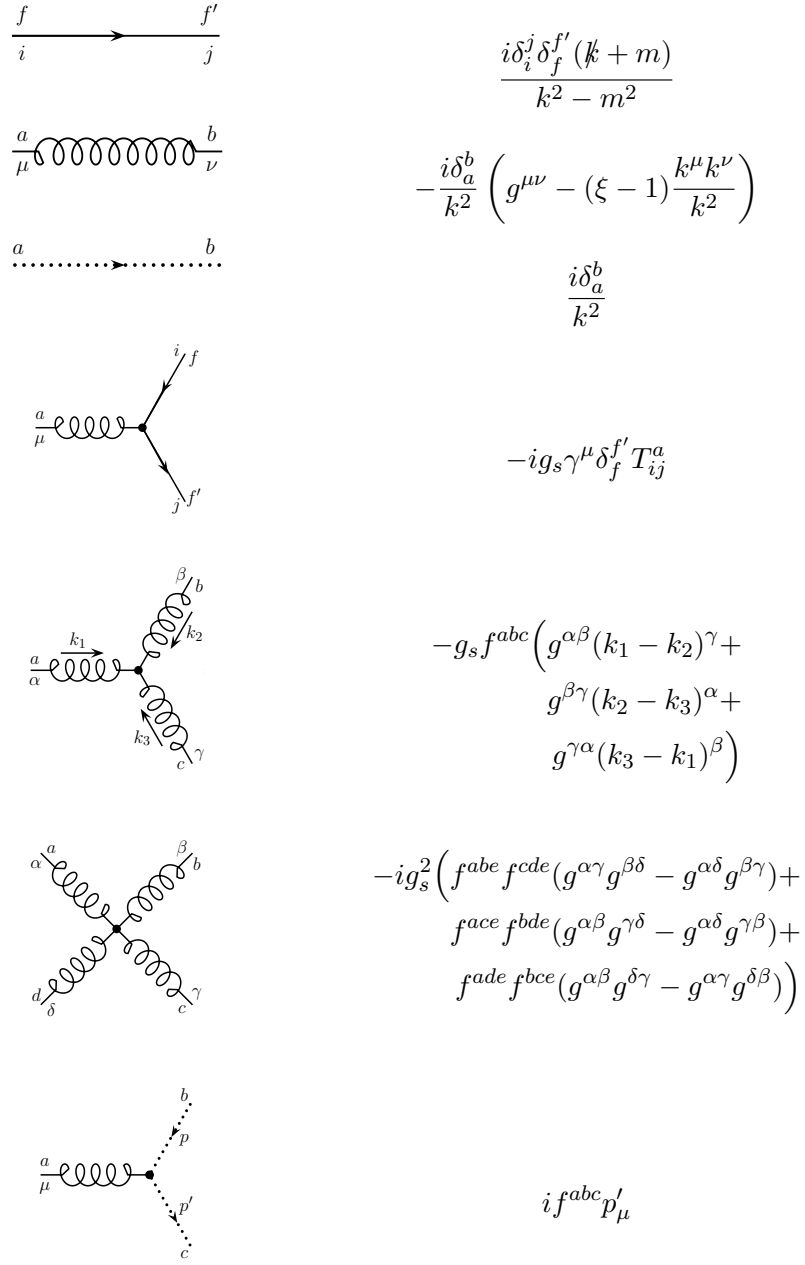
$$\langle 0 | \bar{c}_a(x) c_b(y) | 0 \rangle = \int \frac{d^4k}{(2\pi)^4} e^{-ik \cdot (x-y)} \delta_{ab} \frac{i}{k^2}. \tag{2.17c}$$

361 We can read off the remaining QCD vertex factors directly from the interaction
 362 Lagrangian (or - more rigorously derive them by Taylor expanding eq. (2.16) and
 363 disregarding any irrelevant diagrams such as those where no scattering occurs or those
 364 with bubble contributions).

365 The full set of rules for the vertices and propagators are summarised in tab. (2.1). The

³⁶⁶ remaining *Feynman rules* may be summarised as:

Table 2.1: A graphical summary of the Feynman rules. The solid lines indicate a fermion (anti-fermion) propagator with momentum flowing parallel (anti-parallel) to the direction of the arrow. Similarly for the dashed lines which represent the ghost (anti-ghost) propagating and lastly the twisted lines depict a propagating gluon. As in the preceding equations i and j represent fundamental colour indices, a and b represent adjoint colour indices and, where present, f and f' represent fermion flavour. All Greek indices are Lorentz indices.



- 367 1. Incoming external lines with spin s and momentum p are given a factor of $u_i^{(s)}(p)$
 368 or $\bar{v}_i^{(s)}(p)$ for quarks or anti-quarks. Similarly outgoing external quark or anti-
 369 quark lines get a factor $\bar{u}_i^{(s)}(p)$ or $v_i^{(s)}(p)$. If the external particles are not coloured
 370 the procedure is the same but of course the spinors will no longer be $SU(3)$
 371 fundamental vectors. External gluons with momentum p , polarisation ϵ and
 372 colour a are replaced by $\epsilon^a(p)$ or $\epsilon^{a*}(p)$ depending on whether they are incoming
 373 or outgoing.
- 374 2. For each vertex or propagator in the Feynman diagram insert the corresponding
 375 mathematical expression (see tab. (2.1)). The order of the Lorentz indices must
 376 be the same as that found by tracing the fermion lines in the diagram backwards,
- 377 3. A factor of -1 must be included for each anti-fermion line flowing from the initial
 378 state to the final state,
- 379 4. A factor of -1 must be included for each fermion, anti-fermion or ghost loop in
 380 the diagram
- 381 5. An integration over any unconstrained momenta in the diagram must be included
 382 with measure:

$$\int \frac{d^4k}{(2\pi)^4}, \quad (2.18)$$

383 where k is the momenta in question and the integral is understood to run over
 384 all four momentum components from zero up to infinity,

- 385 6. A diagram dependent symmetry factor must be included,
- 386 7. Lastly, for an unpolarised calculation we must sum over initial spin and colour
 387 and average over all possible final spins and colours.

388 The $u(p)$ and $v(p)$ are Dirac spinors which solve the free Dirac eq. for a plane-wave:

$$(i\gamma^\mu - m)u(p) = 0 \quad (i\gamma^\mu + m)v(p) = 0. \quad (2.19)$$

389 The result of following these Feynman rules is what we refer to as the matrix element,
 390 \mathcal{M} . We will now detail how we go from the matrix element of some scattering process
 391 to a useful physical observable: the *partonic cross-section*, $\hat{\sigma}$. The matrix element
 392 is related to the fully-differential cross-section by ‘Fermi’s golden rule’ which, for a
 393 scattering process $p_a + p_b \rightarrow p_1 + \dots + p_m$ is given by

$$d\hat{\sigma} = \frac{|\mathcal{M}(p_a + p_b \rightarrow p_1^{(f)}, \dots, p_m^{(f)})|^2}{F} \times (2\pi)^4 \delta^{(4)}(p_a + p_b - p_1 - \dots - p_m) \times \frac{d^3 \vec{p}_1}{2E_1(2\pi)^3} \cdots \frac{d^3 \vec{p}_m}{2E_m(2\pi)^3}, \quad (2.20)$$

392 where $F = 4\sqrt{(p_a p_b)^2 - m_a^2 m_b^2}$ is the flux of the incoming particles and the delta
393 function acts to enforce momentum conservation for the process.

394 We now have a procedure for going from a scattering process we wish to calculate to
395 the differential cross-section for that process.

396 2.3 Divergences and Regularisation

397 In the preceding section we saw that any unconstrained momenta in a Feynman diagram
398 must be integrated over to account for all possible ways the momenta in the process
399 may flow. We refer to these contributions as loop-level or higher-order corrections.
400 When calculating these corrections we encounter divergences of various kinds which
401 can be divided up into three classes based on how they arise.

402 2.3.1 Ultraviolet divergences

403 Ultraviolet divergences (UV) occur when all the components of a loop momenta grow
404 large, $k^\alpha \rightarrow \infty$, such that k^2 becomes the dominant term in propagator. Since these
405 extremely high momentum modes corresponding to physics at very short distance scales
406 we choose to interpret these divergences as an indication that our theory is only an
407 effective theory and we shouldn't attempt to apply it to all scales. We can quickly spot
408 diagrams with these pathologies with a naive power counting argument. For example
409 given a diagram which results in a term such as the following:

$$\int \frac{d^4 k}{k^2(k^2 - m^2)}, \quad (2.21)$$

410 where m is some finite mass. In the UV region where $k \rightarrow \infty$ this is asymptotically
411 equal to:

$$\sim \int \frac{d^4k}{k^4}, \quad (2.22)$$

⁴¹² which is clearly logarithmically divergent.

⁴¹³ 2.3.2 Infrared and collinear divergences

⁴¹⁴ Infrared and collinear divergences (IRC) occur in theories with massless gauge bosons,
⁴¹⁵ such as QED and QCD, since a particle may emit any number of arbitrarily such
⁴¹⁶ bosons with infinitesimal energy and we would never be able to detect their emission.
⁴¹⁷ In contrast to the UV divergences the IR becomes important in the region of phase
⁴¹⁸ space where $k^2 \rightarrow 0$. A similar power counting analysis to that above can be applied
⁴¹⁹ here. For example if we consider the one-loop correction to the vertex diagram in
⁴²⁰ massless phi-cubed from section (2.2) we would find an integral of the form [64]:

$$I = \int \frac{d^4k}{(2\pi)^4} \frac{1}{k^2(p_1 - k)^2(p_2 + k)^2}, \quad (2.23)$$

⁴²¹ where k is the loop momentum, $q = p_1 + p_2$ is the incoming momentum and p_i the
⁴²² outgoing momenta. Expanding each momentum into light-cone coordinates with p_1 in
⁴²³ the plus-direction, p_2 in the minus-direction:

$$p_1 \sim (p_1^+, 0, \vec{0}) \quad p_2 \sim (0, p_2^-, \vec{0}). \quad (2.24)$$

⁴²⁴ Then take the Eikonal approximation then we have:

$$I = \int \frac{dk^+ k^- k_T^2}{(2\pi)^4} \frac{1}{(2k^+ k^- - k_T^2)(-2p_1^+ k^-)(2p_2^- k^+)}, \quad (2.25)$$

$$= \frac{1}{2q^2} \int \frac{dk^+ k^- k_T^2}{(2\pi)^4} \frac{1}{(2k^+ k^- - k_T^2)(-k^-)(k^+)}, \quad (2.26)$$

⁴²⁵ where $q^2 = 2p_1 \cdot p_2$ since p_i are massless. Here we can further subdivide the divergences
⁴²⁶ contained here into a ‘soft’ sector and a collinear one.

⁴²⁷ Considering first the soft regime if we let all the components of our integration variable,
⁴²⁸ k_μ become small at the same rate, that is, $k^\mu \sim \lambda \sqrt{q^2}$ where $\lambda \rightarrow 0$ then after a change
⁴²⁹ of variables equation (2.26) becomes:

$$I \sim \int \frac{d^4\lambda}{\lambda^4}, \quad (2.27)$$

430 which diverges logarithmically for small lambda. The collinear sector follows similarly,
431 if we now look at the following scaling:

$$k^\pm \sim \sqrt{q^2} \quad k^\mp \sim \lambda^2 \sqrt{q^2} \quad k_T^2 \sim \lambda \sqrt{q^2}. \quad (2.28)$$

432 I.e. as we decrease λ we make k_μ increasingly collinear to either p_1 or p_2 . Using this
433 scaling exactly reproduces eq. (2.27) and therefore is also divergent.

434 2.3.3 Regularising divergences

435 If we are to extract any useful information from diagrams contributing above leading-
436 order we must find ways to control these these divergences. These methods are
437 called ‘regularisation schemes’. The general plan with all regularisation schemes is to
438 introduce a new parameter to the calculation which is used to get a handle on exactly
439 how the integral diverges. Once we have performed the integration we take the limiting
440 case where the effect of the regulator vanishes and we will see that the divergence now
441 presents itself as some singular function of the regulator when $\Lambda^2 \rightarrow \infty$. There are many
442 ways to regularise divergences each with their own advantages and disadvantages. Here
443 we briefly describe three common approaches.

444 Given that the integrands seen so far only diverge in certain regions (very large or
445 very small momenta) perhaps the most obvious thing to do is to manually introduced
446 alter the limits of our integration. This is the momentum cut-off scheme. we simply
447 replace the upper (lower) bound with some finite large (small) value, Λ^2 . This will
448 regulate any UV (soft) divergences and allow us to complete the calculation provided
449 there are no collinear singularities which this approach cannot hope to regulate. While
450 this method has the advantage of being very conceptually simple it also has the serious
451 disadvantages of breaking translational and gauge invariance. Worse still is that simply
452 limiting the integration to avoid the extremities has not effect on the collinear sector.

453 An alternative which *does* keep both gauge and translational invariance is the Pauli-
454 Villars regularisation scheme [59]. In this picture we replace the introduce and extra
455 field (or many extra fields [40]) which has the opposite spin-statistics and therefore has
456 the effect of suppressing the very high mass region in the integrand as follows

$$\int \frac{d^4k}{(2\pi)^4} \frac{1}{p^2 - m^2} \rightarrow \int \frac{d^4k}{(2\pi)^4} \left(\frac{1}{p^2 - m^2} - \frac{1}{p^2 - M^2} \right), \quad (2.29)$$

457 where M is the mass of the Pauli-Villars field with $m \ll M$. However, once again this
458 does not treat any problems in the IRC sectors.

459 Lastly we have dimensional regularisation. Here we analytically continue the number
460 of dimensions in our integral away from $d = 4$. We still want to be able to return to
461 our physical four dimensional theory and so we choose

$$d = 4 - 2\epsilon \quad (2.30)$$

462 where ϵ is the regulator by which we control the divergence. Clearly then the limit $\epsilon \rightarrow 0$
463 would recover our original theory. It is worth noting that there are many conventions
464 for defining epsilons but up to signs and factors of 2 they are equivalent. Dimensional
465 regularisation treats both the UV and the IRC divergences and translational and gauge
466 invariance are preserved. The disadvantage is that this modification changes the Dirac
467 algebra relations which typically makes computing the integrals more involved.

468 2.4 Renormalising the QCD Lagrangian

- 469 • Is this section really necessary? We don't actually use counter-terms/dressed
470 vertices anywhere etc.
- 471 • Could be combined with the following section as 'Renormalisation and the QCD
472 Beta function'?

473 2.5 The QCD Beta function

474 QCD has two striking features which are not apparent from the Lagrangian derived
475 above. The first is asymptotic freedom. This is the fact that at *high* energies the QCD
476 coupling strength becomes increasingly weak and it is this which allows us to perform
477 a perturbative expansion of physical observables such as cross-sections. The second
478 feature is confinement. Confinement is the reason we do not observe bare quarks and
479 gluons in nature, instead we only see bound states of these fundamental QCD partons.
480 This is because at very *low* energies the coupling strength becomes increasingly strong.

481 It turns out that when renormalise QCD to remove the ultraviolet singularities we
482 introduce a scale dependence in the coupling strength:

$$\alpha_s = \alpha_s(\mu_r). \quad (2.31)$$

483 This scale, μ_r , is the renormalisation scale discussed in section (2.4). It can be
484 interpreted as a measure of our ignorance of the true high-scale theory which governs
485 nature, that is to say, we believe QCD is the right theory *only up to* some scale μ_r .
486 The evolution of α_s with μ_r is given by the renormalisation group equation:

$$\mu_r^2 \frac{\partial \alpha_s}{\partial \mu_r^2} = \beta(\alpha_s(\mu_r^2)), \quad (2.32)$$

487 where the $\beta(\alpha_s)$ is the beta function. It can be expanded perturbatively as a series in
488 α_s as follows:

$$\beta(\alpha_s) = -\beta_0 \alpha_s (1 + \beta_1 \alpha_s + \beta_2 \alpha_s^2 + \dots), \quad (2.33)$$

489 where the perturbative coefficients, β_i , can be calculated using the methods of section
490 (2.2). For example the leading order contribution, β_0 , is given by:

$$\beta_0 = 11 - \frac{2n_f}{3}. \quad (2.34)$$

491 If we truncate eq. (2.33) at leading-order in α_s then we can solve eq. (2.32) and we see
492 that the coupling, $\alpha_s(\mu_r)$, ‘runs’ with the following form:

$$\alpha_s(Q^2) = \frac{\alpha_s(\mu_r^2)}{1 + \alpha(\mu_r^2) \frac{\beta_0}{4\pi} \ln \frac{Q^2}{\mu_r^2}}. \quad (2.35)$$

493 It is clear from this (since in the standard model we have $n_f \leq 6$ and therefore $\beta_0 > 0$)²
494 that as Q^2 tends to zero the coupling strength becomes very large and at high values for
495 Q^2 we see that $\alpha_s(Q^2) \rightarrow 0$. This later limit is exactly the asymptotic freedom property
496 of QCD and it holds even when we include the higher order terms we neglected in the
497 leading-order approximation used to arrive at eq. (2.35) [20]. It is an essential result

²The number of fermions we consider depends on the energy scale we are at. Clearly we must be at an energy larger than the mass of any given quark for it to be produced. This was experimentally observed in the famous R -ratio where the ratio of the $e^+e^- \rightarrow$ hadrons cross-section to the $e^+e^- \rightarrow \mu^+\mu^-$ cross-section was investigated

in that it allows us to perform perturbative expansions of observables and without this none of the following work would be possible. The evolution of the strong coupling with Q^2 is shown in fig. (2.1), it shows several extracted values of α_s based on six various types of experiment. For example, the hadronic collider predictions include studies of the ratio of the 3-jet inclusive cross-section to the 2-jet inclusive cross-section as a means of finding the strong coupling [31].

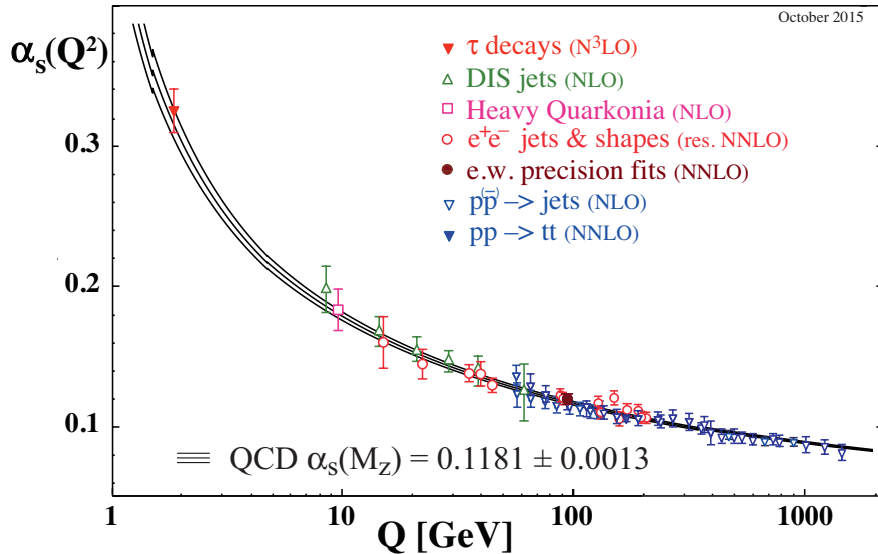


Figure 2.1: The evolution of α_s over several orders of magnitude in the scale of the process Q^2 . The data points fitted are of varying degrees of formal accuracy ranging from next-to-leading order in α_s (NLO) to next-to-next-to-next-to-leading order in α_s (N³LO). Fig. from [20].

2.6 QCD Factorisation at Hadronic Colliders

So far we have only talked about the very general idea of two particles interacting and scattering off one another into some final state which we are interested in. This is too simple a picture when we are considering hadronic colliders such as the Large Hadron Collider (proton-proton), the Tevatron (proton-antiproton), HERA (proton-lepton) and, potentially, a Future Circular Collider (FCC) with a hadronic initial state. At experiments we collide QCD bound states with one another but in practise when calculating cross-sections we perform a sum over the possible combinations of initial states we may encounter in the two incoming hadrons. In order to do this we must have a good understanding of the dynamics of the partons inside the onrushing hadrons; this understanding is encoded in the Parton Distribution Functions (PDFs). A PDF,

515 $f_{i/H}(x, Q^2)$ is a function which tells us how likely we are to find a parton of type i
516 carrying a fraction x of the total hadrons momentum in a hadron, of type H , during a
517 collision occurring at an energy scale Q . Because the PDFs contain non-perturbative
518 information we cannot compute their properties in the same way as we calculate cross-
519 sections, instead they are determined by fitting to data from a range of experiments
520 (such as those mentioned above). Once we have the PDFs we can compute the physical
521 hadronic cross-sections, σ , by convoluting two of them (one for each hadron) with the
522 partonic cross-section for the scattering of partons of type i and j , $\hat{\sigma}_{ij}$, discussed in
523 section (2.2) and summing over the possible initial partons as follows:

$$\sigma(Q^2) = \sum_{f_a, f_b} \int_0^1 dx_a dx_b f_{a/H_a}(x_a, Q^2) f_{b/H_b}(x_b, Q^2) \hat{\sigma}_{ij}(\alpha_s(\mu_r), \mu_r^2, \mu_f^2). \quad (2.36)$$

524 Eq. (2.36) can be intuitively understood as a separation of scales; the long distance
525 physics of the PDFs is manifestly distinct from the short distance hard scatter contained
526 in the partonic cross-section. The scale at which we separate the long and short range
527 physics is called the *factorisation scale*, μ_f . As with the renormalisation scale it is
528 not *a priori* clear what is the correct factorisation scale and results of perturbative
529 calculations are often quoted with a ‘scale uncertainty’ band.

530 2.7 From Partons to Jets

531 As alluded to in section (2.5) the computations of scattering amplitudes can only take us
532 so far when comparing simulations to experiments. In particular, the final state quarks
533 and gluons in our perturbative picture of QCD differ from the confined hadrons observed
534 at hadronic colliders: It is well known that final state QCD partons fragment and emit
535 showers of additional radiation before finally they becomes colourless bound states in
536 a process known as ‘hadronisation’. This process is not perturbatively well-understood
537 since it occurs at scale, often called Λ_{QCD} , at which QCD becomes non-perturbative, *i.e.*
538 the coupling constant of the theory has become too large for us to legitimately truncate
539 a perturbative expansion. There are models for both the ‘parton shower’ behaviour of
540 the energetic final state partons, such as **Pythia** [63], **Herwig** [33] and **Sherpa** [46] as
541 well as models for the hadronisation such as the ‘Lund string model’ [17] implemented
542 in various physics software packages but most relevantly (for the remainder of this
543 thesis) - in the **Ariadne** code.

544 All high energy collider experiments see a great deal of QCD radiation in the final
545 state. This radiation, produced through the mechanisms outlined above, appears in

546 columnated structures called ‘jets’ and so it is at the jet level that we may compare our
 547 simulated results to actual measurements. The question of how we best map from the
 548 parton level to the jet level is not a trivial one: A single high-energy (or ‘hard’) parton
 549 may split and form two final state jets but equally two low energy (or ‘soft’) partons
 550 may combine into a single jet.

551 There are several approaches to this problem include the **SISCone** algorithm [61] and
 552 Pythia’s own implementation **CellJet** [62]. However the most commonly user family
 553 of jet reconstruction algorithm are known as the ‘sequential recombination algorithms’.
 554 This group of approaches include the Cambridge-Aachen, k_T and anti- k_T algorithms.
 555 The general algorithm, as given in [24], is:

- 556 1. Given a list of final state partons calculate some generalised distance, d_{ij} , between
 557 all possible combinations of jets i and j as well as d_{iB} where B is the beam-line,
- 558 2. We identify the smallest value of these. If, say d_{ab} is the smallest, we combine
 559 partons a and b . If however d_{aB} is the smallest then we call a a jet and remove
 560 it from the list of partons,
- 561 3. We then recompute all the generalised distances and repeat steps 1 and 2 until
 562 no further partons remain,

563 where the generalised distances are defined as

$$d_{ij} = \min(k_{Ti}^{2p}, k_{Tj}^{2p}) \frac{\Delta R^2}{R^2}, \quad (2.37)$$

$$d_{iB} = k_{Ti}^{2p},$$

564 where k_{Ti} is the transverse momentum of the i^{th} parton, R is a free parameter in
 565 the clustering which relates to the size of the jets and ΔR^2 is the distance in the
 566 detector metric between the two partons given $\Delta R^2 = \Delta\phi^2 + \Delta y^2$ where $\Delta\phi$ and Δy
 567 are the angular distance (about the beam line) between the partons and the rapidity
 568 gap between the partons respectively. The parameter is p and it is this which specifies
 569 precisely which clustering algorithm we are using; $p = 0$ reduces to the Cambridge-
 570 Aachen scheme while $p = \pm 1$ give the k_T and anti- k_T respectively. The question of
 571 which to use is outlined in detail in [24] but we give a brief summary here.

572 The choice of jet algorithm boils down to handful of key properties the algorithm much
 573 exhibit. Given a set of hard QCD final states we require that the result of the clustering
 574 algorithm, i.e. the jets and jet shapes, are not unduly sensitive to additional soft and
 575 collinear radiation. This is intuitively clear since, for example, a final state with a

576 single high energy quark with momentum, k_{Ti} , may radiate infinitely a multitude of
577 infinitely soft gluons, k_{Ts_i} , which may (or may not) be collinear to the original parton
578 - but since $k_{Ts_i} \ll k_{Ti}$ the result must be a single jet, j_{Ti} , which has $j_{Ti} \sim k_{Ti}$.
579 Any algorithm which satisfies this is said to be infra-red and collinear (IRC) safe. We
580 also want an algorithm which is insensitive to the hadronisation model used, or any
581 possible extra multiple-parton or experimental pile-up emissions since these things are,
582 at present, poorly understood. It is also worth mentioning that since jet clustering
583 algorithms are used in experimental triggers to quickly catagorise events they should
584 be as computational cheap as possible.
585 Although the Cambridge-Aachen algorithm has advantages in some experimental
586 searches such as studies where the substructure of jets is of particular interest [7,22], the
587 most widely used sequential recombination algorithm is the anti- k_t algorithm ($p = -1$)
588 and so all of the work which follows and all of the experimental comparisons made will
589 use this as the method for mapping simulated parton level results to a more useful set
590 of jet level results. The jet size parameter R varies between experiments but is typically
591 either 0.4 for ATLAS analyses or 0.5 for CMS analyses.

592 2.8 Perturbative QCD and Resummation

593 In section 2.2 we saw that we could separate out the QCD Lagrangian into free and
594 interacting components and that vacuum expectations of time ordered fields could
595 be found by taking functional derivatives of the free partition function (eq. (2.16)).
596 Since terms which give rise to interactions in the Lagrangian come with a factor of
597 the coupling strength, g , Taylor expanding the exponential in eq. (2.16) will yield an
598 infinite series of terms and, in principle, in order to compute any physical observable we
599 must calculate we must evaluate all of these. Of course in practise this is not possible.
600 We must choose a subset of terms from this infinite array which we reason will give the
601 *best possible approximation to the full series*.

602 2.8.1 Fixed-order Perturbation

603 The fixed-order perturbative operates on the assumption that since, as we saw in section
604 2.5, the coupling strength α_s , and hence also the coupling constant, g , in the expansion,
605 becomes small at large energy scales we may truncate the series at some power of g .
606 For example given a cross-section of a scattering, $X \rightarrow Y$, we wish to calculate the
607 fixed order picture of the expansion would be:

$$\sigma_{X \rightarrow Y} = \sum_{i=1}^N \alpha_s^i(Q^2) \mathcal{C}_{X \rightarrow Y}^{(i)} \quad (2.38)$$

608 where $\mathcal{C}_{X \rightarrow Y}^{(i)}$ are the coefficient terms which encode the kinematics of the diagrams
 609 contributing at each ‘order’ in the series. Since we expect that the more terms we
 610 can calculate the better our truncated series will approximate the full result we should
 611 choose N as large as possible though in principle it is determined by the complexity and
 612 the computational cost of the relevant calculation of the coefficient functions. Recent
 613 progress has allowed the automation of next-to-leading order QCD calculations ($N = 2$)
 614 in packages such in **MadGraph** (v5) [13], **BlackHat** [21], **MC@NLO** [38] and **Powheg** [37]. In
 615 general it is not known how to compute multi-loop (i.e. $N \geq 3$) calculations and while
 616 process specific calculations have been completed [23, 41, 43], it is still very much a hot
 617 topic in theoretical physics.

618 It is important to note the limitations of this fixed-order scheme. For example if we
 619 were to consider NLO corrections to dijet production we would only be able to produce
 620 final states with two or three jets (since we can only have one extra real emission).
 621 Clearly this is a limitation since the external fermion lines can radiate arbitrarily many
 622 extra gluons. It is precisely this phenomenon which is shown in fig. 2.2, the NLO
 623 calculations (shown in green and black) are limited to $\langle \text{jets} \rangle \leq 3$ which the predictions
 624 from **POWHEJ+PYTHIA** and **HEJ** which include higher-order corrections and predict a
 625 higher average number of jets. Note that the higher-order corrections here are *not*
 626 the same in the case of **POWHEJ+PYTHIA** and **HEJ**. Also note that although the scale
 627 uncertainty band of the NLO calculation *does* exceed $\langle \text{jets} \rangle = 3$ this is not a result
 628 of the formalism but instead comes about as the result of an attempt to quantify the
 629 residual dependence of the calculation on the factorisation and renormalisation scales.
 630 This scale dependence of observables will be discussed in more detail in chapter 4.
 631 There are frameworks to allow the ‘merging’ of NLO calculations of different multiplicity
 632 but the details of these are beyond the scope of this thesis. A comprehensive review of
 633 such methods may be found in [11].

634 We now present an instructive fixed-order calculation of the next-to-leading corrections
 635 to quark-antiquark pair production via an off-shell photon [35].

636 2.8.2 An Example Fixed-Order Calculation

637 The Feynman diagrams which need to be included for the and $\mathcal{O}(1)$ and $\mathcal{O}(\alpha_s)$
 638 corrections to the $\gamma^* \rightarrow q\bar{q}$ process are shown in fig. (2.3). We refer to fig. (2.3a)

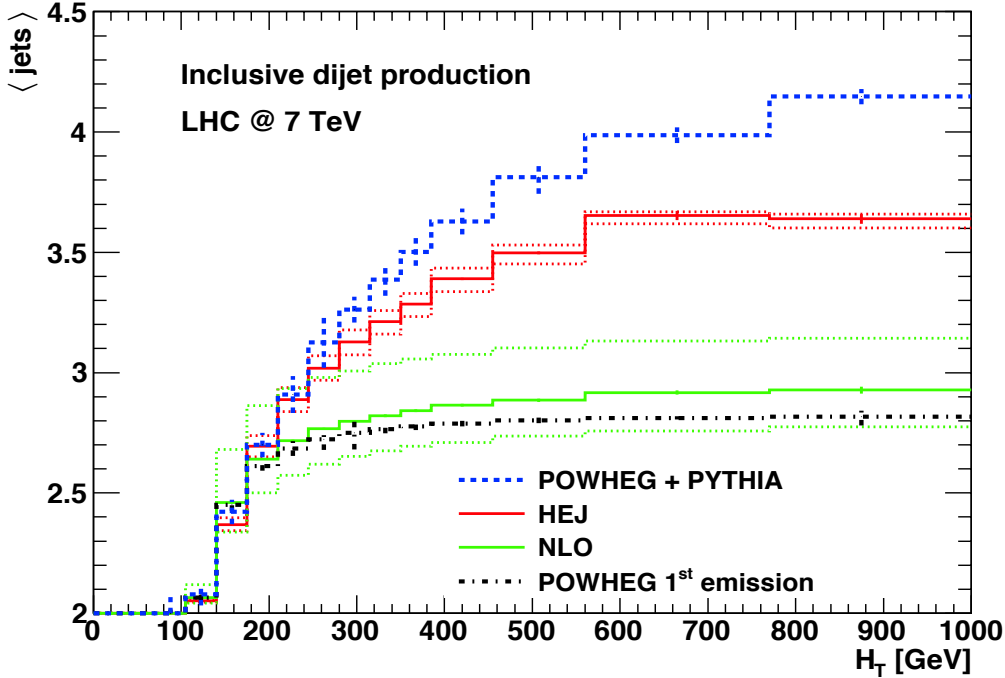


Figure 2.2: Simulations of the average number of jets as a function of the sum of the transverse momenta in the event, H_T , for inclusive dijets at a 7TeV LHC.

as the tree level diagram, fig. (2.3b) as the vertex correction and figs. (2.3c) and (2.3d) as the self-energy corrections. Figs. (2.3e) and (2.3f) are the ‘real correction’. Since the virtual corrections all have the same final state they must be summed and squared together. To make the order of each term in the perturbative expansion clear we extract the α_s factors from the \mathcal{A}_i here. Therefore:

$$\begin{aligned} |\mathcal{M}|^2 &= |\mathcal{A}_0 + \alpha_s \mathcal{A}_v + \alpha_s \mathcal{A}_{se1} + \alpha_s \mathcal{A}_{se2}|^2 + \mathcal{O}(\alpha_s^2) \\ &= |\mathcal{A}_0|^2 + 2\alpha_s \Re\{\mathcal{A}_0^* \mathcal{A}_v\} + 2\alpha_s \Re\{\mathcal{A}_0^* \mathcal{A}_{se1}\} \\ &\quad + 2\alpha_s \Re\{\mathcal{A}_0^* \mathcal{A}_{se2}\} + \mathcal{O}(\alpha_s^2), \end{aligned} \quad (2.39)$$

where the bar on the LHS means there is an implicit sum over spins and polarisations on the RHS. We can see then that to $\mathcal{O}(\alpha_s)$ we have four contributions to consider, but the two self-energy contributions will have the same functional form so it would seem that in practice we only need to perform three calculations - it turns out this is not the case; we will find that the divergence associated with exchanging a soft gluon

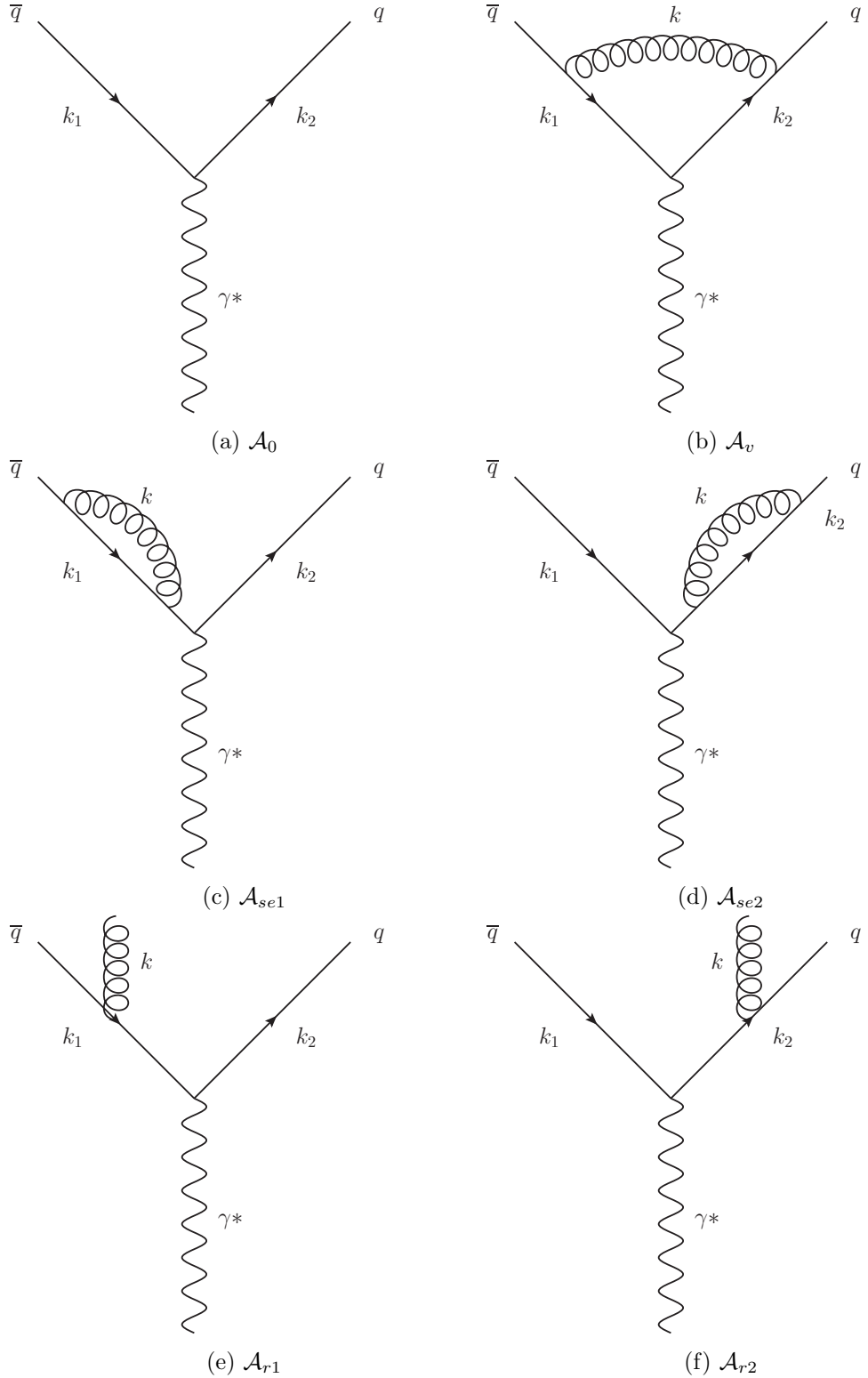


Figure 2.3: Feynman diagrams for calculating the $O(\alpha_s)$ correction to $\gamma^* \rightarrow q\bar{q}$. Fig. (2.3a) is the leading order contribution. Figs. (2.3b - 2.3d) are the virtual corrections and lastly figs. (2.3e - 2.3f) are the real emission contributions.

in fig. (2.3b) can only be cancelled if we also include the soft divergences that arise from figs. (2.3e) to (2.3f). At first glance this seems very peculiar since these diagrams have different final states and therefore should have no business contributing to this calculation. However, since the gluon can be emitted with vanishingly small momentum it would be experimentally impossible to detect and therefore the final states would look the same to an imperfect observer.

It is the cancellation of these divergences that will be shown in detail in the next two sections. Figs. (2.3a), (2.3b) and (2.3e) will be calculated in detail while the result for the self energy expressions will only be omitted since it can be cancelled by choosing the work in the Landau gauge [35]. Since we expect both UV and IR divergences we choose to work in the dimensional regularisation scheme.

660 The Leading Order Process

If we let the pair-produced quarks have charge $\pm Qe$ then the Feynman rules outlined in section 2.2 give:

$$\mathcal{A}_0 = -ieQ\bar{u}^{\lambda_2}(k_2)\gamma^\mu v^{\lambda_1}(k_1)\epsilon_\mu^r(p), \quad (2.40)$$

where we have used the QED Feynman rule for a quark-antiquark-photon vertex: $iQe\gamma^\mu$, the λ_i 's are the spins of the quarks, r is the polarisation of the incoming photon and $p = k_1 + k_2$ is the momentum carried by the incoming photon. To calculate we can square and since we are typically interested in unpolarised calculations we perform a sum over all polarisations and spins (we also choose this point to include the sum over the possible colour states of the outgoing quarks):

$$|\overline{\mathcal{A}_0}|^2 = 3 \sum_{\forall \lambda, r} e^2 Q^2 [\bar{u}^{\lambda_2}(k_2)\gamma^\mu v^{\lambda_1}(k_1)][\bar{v}^{\lambda_1}(k_1)\gamma^\nu v^{\lambda_2}(k_1)]\epsilon_\mu^r(p)\epsilon_{*\mu}^r(p). \quad (2.41)$$

We can now use Casimir's trick [44] to convert this spinor string into a trace, using the replacements $\sum_r \epsilon_\mu^r \epsilon_{*\nu}^r = -g_{\mu\nu}$ and the completeness conditions for spinors:

$$|\overline{\mathcal{A}_0}|^2 = -e^2 Q^2 \text{Tr}[\not{k}_2 \gamma^\mu \not{k}_1 \gamma_\mu], \quad (2.42)$$

where we have used the high energy limit to discard the quark mass terms. This trace can be evaluated in arbitrary dimensions to give, in the high energy limit:

$$|\overline{\mathcal{A}_0}|^2 = 6e_d^2 Q^2 s(d-2), \quad (2.43)$$

673 where we have defined the usual Mandelstam variable $s = (k_1 + k_2)^2 = 2k_1 \cdot k_2$ and define
 674 $e_d^2 = e^2 \mu^{4-d}$ where μ has units of mass in order to make the coupling e dimensionless.
 675 To find the leading order cross-section we divide by the particle flux and multiply by
 676 the two particle phase space which is given by:

$$\int d^{2d-2} R_2 = 2^{1-d} \pi^{\frac{d}{2}-1} \frac{\Gamma(\frac{d}{2}-1)}{\Gamma(d-2)} s^{\frac{d-4}{2}}, \quad (2.44)$$

677 where R_2 is the two particle phase space in d dimensions. Combining these factors and
 678 defining $\alpha_e = \frac{e^2}{4\pi}$:

$$\begin{aligned} \sigma_0 &= 3 \cdot 2^{2-d} \pi^{1-\frac{d}{2}} \frac{\Gamma(\frac{d}{2}-1)}{\Gamma(d-2)} s^{\frac{d-4}{2}} 4\pi \alpha \mu^{d-4} Q^2 s(d-2) \frac{1}{2s} \\ &= 3\alpha Q^2 \left(\frac{s}{4\pi\mu^2} \right)^{\frac{d}{2}-2} \left(\frac{d}{2}-1 \right) \frac{\Gamma(\frac{d}{2}-1)}{\Gamma(d-2)}. \end{aligned} \quad (2.45)$$

679 and finally using $x\Gamma(x) = \Gamma(x+1)$ we get:

$$\sigma_0 = 3\alpha Q^2 \frac{\Gamma(\frac{d}{2})}{\Gamma(d-2)} \left(\frac{s}{4\pi\mu^2} \right)^{\frac{d}{2}-2}. \quad (2.46)$$

680 It is important to note that in the limit $\epsilon \rightarrow 0$ the Born cross-section remains finite.

681 The Virtual $\mathcal{O}(\alpha_s)$ Corrections

682 The virtual correction graphs are shown in figs. (2.3b), (2.3c) and (2.3d). We will begin
 683 by calculating the second term in eq. (2.39). Using the Feynman rules we have:

$$\begin{aligned} \mathcal{A}_v &= \int \frac{d^d k}{(2\pi)^d} \bar{u}^{\lambda_2}(k_2) (-ig_s \mu^\epsilon \gamma^\alpha T_{ij}^a) \frac{i(\not{k}_1 + \not{k})}{(k_1 + k)^2} (-ieQ \gamma^\mu) \frac{i(\not{k}_2 - \not{k})}{(k_2 - k)^2} \\ &\quad (-g_s \mu^\epsilon \gamma^\beta T_{ij}^a) \epsilon_\mu^r(p) \frac{-i}{k^2} \left(g_{\alpha\beta} + (1-\xi) \frac{k^\alpha k^\beta}{k^2} \right) v^{\lambda_1}(k_1). \end{aligned}$$

$$\mathcal{A}_v = -ig_s^2 e Q \mu^{2\epsilon} \text{Tr}(T^a T^a) \bar{u}^{\lambda_2}(k_2) \int \frac{d^d k}{(2\pi)^d} \frac{\mathcal{N}_1(k_1, k_2, k)}{k^2(k_1 + k)^2(k_2 - k)^2} v^{\lambda_2}(k_2),$$

684 where the numerator of the fraction is given by:

$$\mathcal{N}_1(k_1, k_2, k) = \gamma^\alpha(\not{k}_1 + \not{k}) \gamma^\mu(\not{k}_2 - \not{k}) \gamma_\beta \left(g^{\alpha\beta} + (1 - \xi) \frac{k^\alpha k^\beta}{k^2} \right). \quad (2.48)$$

685 From eq. (2.39) we see we need $\mathcal{A}_0^* \mathcal{A}_v$:

$$\mathcal{A}_0^* \mathcal{A}_v = g_s^2 e^2 Q^2 \text{Tr}(T^a T^a) [\bar{v}^{\lambda_1}(k_1) \gamma^\nu u(k_2)] \quad (2.49)$$

$$[\bar{u}^{\lambda_2}(k_2) \int \frac{d^d k}{(2\pi)^d} \frac{\mathcal{N}_1(k_1, k_2, k)}{k^2(k_1 + k)^2(k_2 - k)^2} v^{\lambda_1}(k_1)] \epsilon_\mu^r(p) \epsilon_{*\nu}^r(p). \quad (2.50)$$

686 Now performing the spin/polarisation/colour sum and average gives:

$$\overline{\mathcal{A}_0^* \mathcal{A}_v} = -\frac{g_s^2 e^2 Q^2}{2} \int \frac{d^d k}{(2\pi)^d} \frac{\mathcal{N}_2(k_1, k_2, k)}{k^2(k_1 + k)^2(k_2 - k)^2}, \quad (2.51)$$

687 where:

$$\mathcal{N}_2(k_1, k_2, k) = \text{Tr}[\not{k}_1 \gamma_\alpha(\not{k}_1 + \not{k}) \gamma_\mu(\not{k}_2 - \not{k}) \gamma_\beta \not{k}_2 \gamma^\mu] \left(g^{\alpha\beta} + (1 - \xi) \frac{k^\alpha k^\beta}{k^2} \right). \quad (2.52)$$

688 Before we can proceed any further we must evaluate the trace term in the integral.
689 As mentioned briefly in section 2.3.3 this is not as easy as it seems because, although
690 the Dirac matrices still satisfy the Clifford algebra, the various identities for their
691 contractions and traces change when we are in d dimensions. Two useful examples are
692 shown below:

$$g_{\mu\nu} g^{\mu\nu} = d \quad (2.53a)$$

$$\gamma^\mu \gamma_\nu \gamma_\mu = (d - 2) \gamma_n u \quad (2.53b)$$

693 Using the FORM package [52] to perform the two trace terms present gives:

$$\begin{aligned} \text{Tr}[\not{k}_1 \gamma_\alpha (\not{k}_1 + \not{k}) \gamma_\mu (\not{k}_2 - \not{k}) \gamma^\alpha \not{k}_2 \gamma^\mu] &= s[s(8 - 4d) + \frac{(k_1 \cdot k)(k_2 \cdot k)}{s}(32 - 16d) \\ &\quad - (16 - 8d)(k_1 \cdot k - k_2 \cdot k) + k^2(16 - 12d + 2d^2)], \end{aligned} \quad (2.54)$$

⁶⁹⁴ and,

$$\begin{aligned} \text{Tr}[\not{k}_1 \gamma_\alpha (\not{k}_1 + \not{k}) \gamma_\mu (\not{k}_2 - \not{k}) \gamma_\beta \not{k}_2 \gamma^\mu] k^\alpha k^\beta &= s[(k_1 \cdot k)(k_2 \cdot k)(16 - 8d) \\ &\quad + k^2(8 - 4d)(k_2 \cdot k - k_1 \cdot k) - k^4(4 - 2d)], \end{aligned} \quad (2.55)$$

⁶⁹⁵ where $s = 2k_1 \cdot k_2$ and we have used the on-shell relations. After factorising the terms
⁶⁹⁶ quadratic in d and combining the two trace terms we arrive at:

$$\overline{\mathcal{A}_0^* \mathcal{A}_v} = -4s \left(\frac{d}{2} - 1 \right) \frac{g_s^2 e^2 Q^2}{2} \int \frac{d^d k}{(2\pi)^d} \frac{\mathcal{N}_3(k_1, k_2, k)}{k^2(k_1 + k)^2(k_2 - k)^2}, \quad (2.56)$$

⁶⁹⁷ where:

$$\mathcal{N}_3(k_1, k_2, k) = -2s + \frac{8k \cdot k_1 k \cdot k_2}{s} + (6 + 2\xi)(k \cdot k_1 - k \cdot k_2) + k^2(d - 4) \quad (2.57)$$

$$-4(1 - \xi) \frac{k \cdot k_1 k \cdot k_2}{k^2} - (1 - \xi)k^2. \quad (2.58)$$

⁶⁹⁸ Combining this with the particle flux and the two particle phase space we can write
⁶⁹⁹ an expression for the vertex corrected cross-section. Once again we scale the couplings
⁷⁰⁰ such that they remain dimensionless by defining $g_d^2 = g_s^2 \mu^{2-\frac{d}{2}}$:

$$\begin{aligned} \sigma_v &= -4s \left(\frac{d}{2} - 1 \right) \frac{g_d^2 \mu^{2-\frac{d}{2}} e^2 Q^2}{4s} 2^{1-d} \pi^{\frac{d}{2}-1} \frac{\Gamma(\frac{d}{2}-1)}{\Gamma(d-2)} s^{\frac{d-4}{2}} \int \frac{d^d k}{(2\pi)^d} \frac{\mathcal{N}_3(k_1, k_2, k)}{k^2(k_1 + k)^2(k_2 - k)^2}, \\ \Rightarrow \sigma_v &= -g_d^2 \mu^{2-\frac{d}{2}} Q^2 4\pi \alpha \mu^{4-d} 2^{1-d} \pi^{\frac{d}{2}-1} \frac{\Gamma(\frac{d}{2})}{\Gamma(d-2)} s^{\frac{d-4}{2}} \int \frac{d^d k}{(2\pi)^d} \frac{\mathcal{N}_3(k_1, k_2, k)}{k^2(k_1 + k)^2(k_2 - k)^2}, \\ \Rightarrow \sigma_v &= -\frac{4\sigma_0}{3} g_d^2 \mu^{2-\frac{d}{2}} \int \frac{d^d k}{(2\pi)^d} \frac{\mathcal{N}_3(k_1, k_2, k)}{k^2(k_1 + k)^2(k_2 - k)^2}, \end{aligned}$$

⁷⁰¹ where we have expressed the virtual rate as a multiplicative correction to the Born

702 level rate by comparing directly with eq. (35). We must now use the Feynman
 703 parametrisation to re-express the product of propagators as a sum by introducing new
 704 integration variables. Using:

$$\frac{1}{ab} = \int_0^1 dy \frac{1}{(ay + b(1-y))^2}, \quad (2.60)$$

705 we have:

$$\sigma_v = -\frac{4\sigma_0}{3} g_d^2 \mu^{2-\frac{d}{2}} \int \frac{d^d k}{(2\pi)^d} \int_0^1 dy \frac{\mathcal{N}_3(k_1, k_2, k)}{(k^2 - 2k \cdot k_y)^2 k^2}, \quad (2.61)$$

706 where $k_y = yk_1 - (1-y)k_2$. Examining now the integrand we see there are two different
 707 k dependences and so we partition the terms as follows:

$$\sigma_v = -\frac{4\sigma_0}{3} g_d^2 \mu^{2-\frac{d}{2}} \int \frac{d^d k}{(2\pi)^d} \int_0^1 dy \left(\frac{\mathcal{N}'_3(k_1, k_2, k)}{(k^2 - 2k \cdot k_y)^2 k^2} + \frac{\mathcal{N}''_3(k_1, k_2, k)}{(k^2 - 2k \cdot k_y)^2 k^4} \right), \quad (2.62)$$

708 where,

$$\mathcal{N}'_3(k_1, k_2, k) = -2s + \frac{8k \cdot k_1 k \cdot k_2}{s} + (6+2\xi)(k \cdot k_1 - k \cdot k_2) + k^2(d-4) - (1-\xi)k^2. \quad (2.63a)$$

$$\mathcal{N}''_3(k_1, k_2, k) = -4(1-\xi)k \cdot k_1 k \cdot k_2. \quad (2.63b)$$

709 Differentiating eq. (2.60) with respect to a and b we get the following useful
 710 parametrisations:

$$\frac{1}{a^2 b} = \int_0^1 dx \frac{2x}{(ax + b(1-x))^3}, \quad (2.64a)$$

$$\frac{1}{a^2 b^2} = \int_0^1 dx \frac{6x(1-x)}{(ax + b(1-x))^4}. \quad (2.64b)$$

711 and taking $a = k^2 - 2k \cdot k_y$ and $b = k^2$, simplifying the denominators and performing
 712 a change of variables $K = k - xp_y$ yields:

$$\sigma_v = -\frac{4\sigma_0}{3} g_d^2 \mu^{2-\frac{d}{2}} \int \frac{d^d K}{(2\pi)^d} \int_0^1 dy \int_0^1 dx \left(\frac{2x\mathcal{N}'_3(k_1, k_2, K + xk_y)}{(K^2 - C)^3} + \right. \quad (2.65)$$

$$\left. \frac{6x(1-x)\mathcal{N}''_3(k_1, k_2, K + xk_y)}{(K^2 - C)^4} \right), \quad (2.66)$$

⁷¹³ where $C = x^2 p_y^2$. The change of variables modifies the numerator terms to:

$$\begin{aligned} \mathcal{N}'_3(k_1, k_2, K + xk_y) &= -2s + K^2 \left(\frac{4}{d} + d - 5 + \xi \right) \\ &\quad - (3 + \xi)xs + x^2ys(1 - y)(3 - d - \xi), \end{aligned} \quad (2.67a)$$

$$\mathcal{N}''_3(k_1, k_2, K + xk_y) = (1 - \xi) \left(x^2ys^2(1 - y) - \frac{2s}{d}K^2 \right). \quad (2.67b)$$

⁷¹⁴

⁷¹⁵ We can now perform the integrations over K with the aid of the following result:

$$\int \frac{d^d K}{(2\pi)^d} \frac{(K^2)^m}{(K^2 - C)^n} = \frac{i(-1)^{m-n}}{(4\pi)^{\frac{d}{2}}} C^{m-n+\frac{d}{2}} \frac{\Gamma(m + \frac{d}{2})\Gamma(n - m - \frac{d}{2})}{\Gamma(\frac{d}{2})\Gamma(n)}. \quad (2.68)$$

⁷¹⁶ Looking at the K structure of eqs. (2.67) we can see that there are going to be 4
⁷¹⁷ forms of eq. (2.68) needed in this calculation. I will not show the calculation for every
⁷¹⁸ integral but will show one as an example of how the calculations can proceed. Consider
⁷¹⁹ the contribution of the first term of eq. (2.67a):

$$I = -4s \int_0^1 dy \int_0^1 dx \int \frac{d^d K}{(2\pi)^d} \frac{1}{(K^2 - C)^3} = 4si \int_0^1 dy \int_0^1 dx (4\pi)^{-\frac{d}{2}} C^{-3+\frac{d}{2}} \frac{\Gamma(\frac{d}{2})\Gamma(3 - \frac{d}{2})}{\Gamma(\frac{d}{2})\Gamma(3)}.$$

⁷²⁰ From above we see that $C = x^2 k_y = -x^2 y(1 - y)s$ and so:

$$I = 4si(4\pi)^{-\frac{d}{2}} \Gamma(3 - \frac{d}{2})(-s)^{-3+\frac{d}{2}} \int_0^1 dy \int_0^1 dx x^{-5+d} y^{(-2+\frac{d}{2})-1} (1 - y)^{(-2+\frac{d}{2})-1}, \quad (2.69)$$

⁷²¹ Therefore:

$$I = 4s i(4\pi)^{-\frac{d}{2}} \Gamma\left(3 - \frac{d}{2}\right) (-s)^{-3+\frac{d}{2}} \frac{1}{d-4} \frac{\Gamma^2(\frac{d}{2}-2)}{\Gamma(d-4)}. \quad (2.70)$$

722 Choosing $d = 4 + \epsilon$ (with the intention of taking the limit $\epsilon \rightarrow 0$ once it is safe to do
723 so), and manipulating the gamma functions to expose the pole structure gives:

$$-4 \int_0^1 dy \int_0^1 dxx \int \frac{d^d K}{(2\pi)^d} \frac{1}{(K^2 - C)^3} = 4(-s)^{\frac{\epsilon}{2}} i(4\pi)^{-2-\frac{\epsilon}{2}} \frac{4}{\epsilon^2} \frac{\Gamma\left(1 - \frac{\epsilon}{2}\right) \Gamma^2\left(1 + \frac{\epsilon}{2}\right)}{\Gamma(1+\epsilon)}, \quad (2.71)$$

724 which is clearly divergent in the limit $d \rightarrow 4$. The other integrals follow similarly and
725 the combined result can be expressed as:

$$\sigma_v = \frac{2\alpha_s}{3\pi} \sigma_0 \left(\frac{s}{4\pi\mu^2} \right)^{\frac{\epsilon}{2}} \frac{\Gamma\left(1 - \frac{\epsilon}{2}\right) \Gamma^2\left(1 + \frac{\epsilon}{2}\right)}{\Gamma(1+\epsilon)} \left(-\frac{8}{\epsilon^2} + \frac{6}{\epsilon} - \frac{8+4\epsilon}{1+\epsilon} \right), \quad (2.72)$$

726 where we have defined $\alpha_s = \frac{g_d^2}{4\pi}$. Expanding the product of gamma matrices for $\epsilon \rightarrow 0$
727 gives:

$$\frac{\Gamma\left(1 - \frac{\epsilon}{2}\right) \Gamma^2\left(1 + \frac{\epsilon}{2}\right)}{\Gamma(1+\epsilon)} = \frac{\gamma_E}{2} \epsilon + \left(\frac{\gamma_E^2}{8} - \frac{\pi^2}{48} \right) \epsilon^2 + \mathcal{O}(\epsilon^3), \quad (2.73a)$$

$$\left(\frac{s}{4\pi\mu^2} \right)^{\frac{\epsilon}{2}} = e^{\ln\left(\frac{s}{4\pi\mu^2}\right)^{\frac{\epsilon}{2}}} = e^{\frac{\epsilon}{2} \ln\left(\frac{s}{4\pi\mu^2}\right)} = 1 + \frac{\epsilon}{2} \ln\left(\frac{s}{4\pi\mu^2}\right) + \mathcal{O}(\epsilon^2), \quad (2.73b)$$

728 where γ_E is Euler's constant. Finally then we have:

$$\sigma_v = \frac{2\alpha_s}{3\pi} \sigma_0 \left[-\frac{8}{\epsilon^2} + \frac{1}{\epsilon} (6 - 4\gamma_E - 4L) + \gamma_E (3 - \gamma_E) \right] \quad (2.74)$$

$$- 8 + \frac{\pi^2}{6} + \pi^2 - L^2 - (2\gamma_E - 3)L \Big], \quad (2.75)$$

729 where $L = \ln\left(\frac{s}{4\pi\mu^2}\right)$. We can now see that regardless of our choice of gauge parameter,
730 ξ , the result for the vertex correction is gauge independent. We also see that the
731 parameter introduced to fix the coupling to be dimensionless appears in the final result;
732 this is often the case when using dimensional regularisation and the modified minimal
733 subtraction renormalisation scheme.

⁷³⁴ **The Real $\mathcal{O}(\alpha_s)$ Corrections**

⁷³⁵ The real gluon emission diagrams which contribute to the $\mathcal{O}(\alpha_s)$ corrections are figs.
⁷³⁶ (2.3e) and (2.3f). These diagrams have an indistinguishable final state and so the real
⁷³⁷ contribution will be of the form:

$$|\mathcal{A}_r|^2 = |\mathcal{A}_{left} + \mathcal{A}_{right}|^2 = |\mathcal{A}_{left}|^2 + |\mathcal{A}_{right}|^2 + 2\mathcal{A}_{left}\mathcal{A}_{right}^*, \quad (2.76)$$

⁷³⁸ where \mathcal{A}_{left} and \mathcal{A}_{right} refer to figs. (2.3e) and (2.3f) respectively and are given by:

$$\mathcal{A}_{left} = -Q e g_s T_{ij}^a \bar{u}(k_2) \gamma^\mu \frac{\not{k}_1 + \not{k}}{(k_1 + k)^2} \gamma^\nu v(k_1) \epsilon_\nu \eta_\mu, \quad (2.77a)$$

$$\mathcal{A}_{right} = -Q e g_s T_{ij}^a \bar{u}(k_2) \gamma^\nu \frac{\not{k}_2 + \not{k}}{(k_2 + k)^2} \gamma^\mu v(k_1) \epsilon_\nu \eta_\mu. \quad (2.77b)$$

⁷³⁹ In the calculation of the terms of eq. (64) it will be useful to write the energy fractions
⁷⁴⁰ for each particle as $x_i = \frac{2E_i}{\sqrt{s}}$ (where $i = 1$ is the external antiquark, $i = 2$ is the
⁷⁴¹ antiquark and $i = 3$ is the external gluon). In terms of these invariants the contraction
⁷⁴² of any two external particles simplifies to $p_i \cdot p_j = \frac{1}{2}s(1 - x_k)$ which (since we are still
⁷⁴³ assuming our quarks can be taken to be massless) gives a simple expression for the
⁷⁴⁴ Mandelstam variables. Evaluating the $|...|^2$ terms gives:

$$|\mathcal{A}_{left}|^2 = \frac{Q^2 e^2 g_s^2}{(k_1 + k)^4} \text{Tr}(T^a T^a) \text{Tr}(\not{k}_2 \gamma^\mu (\not{k}_1 + \not{k}) \gamma^\nu \not{k}_1 \gamma_\nu (\not{k}_1 + \not{k}) \gamma_\mu), \quad (2.78a)$$

$$|\mathcal{A}_{right}|^2 = \frac{Q^2 e^2 g_s^2}{(k_2 + k)^4} \text{Tr}(T^a T^a) \text{Tr}(\not{k}_2 \gamma^\nu (\not{k}_2 + \not{k}) \gamma^\mu \not{k}_2 \gamma_\mu (\not{k}_2 + \not{k}) \gamma_\nu), \quad (2.78b)$$

$$\mathcal{A}_{left} \mathcal{A}_{right}^* = \frac{Q^2 e^2 g_s^2}{(k_2 + k)^2 (k_1 + k)^2} \text{Tr}(T^a T^a) \text{Tr}(\not{k}_2 \gamma^\mu (\not{k}_1 + \not{k}) \gamma^\nu \not{k}_1 \gamma_\mu (\not{k}_2 + \not{k}) \gamma_\nu). \quad (2.78c)$$

⁷⁴⁵ Evaluating the trace terms in d -dimensions and rearranging in terms of the energy
⁷⁴⁶ fractions gives:

$$|\mathcal{A}_{left}|^2 = 32Q^2 e^2 g_s^2 \left(1 + \frac{\epsilon}{2}\right)^2 \frac{1 - x_1}{1 - x_2}, \quad (2.79a)$$

$$|\mathcal{A}_{right}|^2 = 32Q^2 e^2 g_s^2 \left(1 + \frac{\epsilon}{2}\right)^2 \frac{1 - x_2}{1 - x_1}, \quad (2.79b)$$

$$2\mathcal{A}_{left} \mathcal{A}_{right}^* = 64Q^2 e^2 g_s^2 \left(1 + \frac{\epsilon}{2}\right) \left(-\frac{\epsilon}{2} - 2 \frac{1 - x_3}{(1 - x_1)(1 - x_2)}\right). \quad (2.79c)$$

⁷⁴⁷ Summing these expressions gives:

$$|\mathcal{A}_r|^2 = 32Q^2e^2g_s^2 \left[\left(1 + \frac{\epsilon}{2}\right)^2 \frac{x_1^2 + x_2^2}{(1-x_2)(1-x_1)} + \epsilon \left(1 + \frac{\epsilon}{2}\right) \frac{2 - 2x_1 - 2x_2 + x_1x_2}{(1-x_2)(1-x_1)} \right]. \quad (2.80)$$

⁷⁴⁸ As with the virtual contributions we are interested in the observable cross-section and
⁷⁴⁹ so we must include the phase space factor for a three particle final state. Unlike the
⁷⁵⁰ two particle phase space calculation here $\int d^{3d-3}R_3$ cannot be integrated completely
⁷⁵¹ and we are left with a differential in terms of the energy fractions defined above:

$$\frac{d^2R_3}{dx_1dx_2} = \frac{s}{16(2\pi)^3} \left(\frac{s}{4\pi}\right)^\epsilon \frac{1}{\Gamma(2+\epsilon)} \left(\frac{1-z^2}{4}\right)^{\frac{\epsilon}{2}} x_1^\epsilon x_2^\epsilon, \quad (2.81)$$

⁷⁵² where $z = 1 - 2\frac{1-x_1-x_2}{x_1x_2}$. Combining eqs. (2.80) and (2.81) with a flux factor gives:

$$\frac{d^2\sigma_r}{dx_1dx_2} = \frac{2Q^2e^2g_s^2F(x_1, x_2; \epsilon)}{\pi} \left(\frac{s}{4\pi}\right)^\epsilon \frac{1}{\Gamma(2+\epsilon)} \left(\frac{1-z^2}{4}\right)^{\frac{\epsilon}{2}} x_1^\epsilon x_2^\epsilon, \quad (2.82)$$

⁷⁵³ where we define $F(x_1, x_2; \epsilon)$ as the algebraic factor in square brackets from eq. (2.80).
⁷⁵⁴ Switching to a dimensionless coupling and introducing α_s as above:

$$\frac{d^2\sigma_r}{dx_1dx_2} = \frac{2Q^2e^2\alpha_s}{\pi} F(x_1, x_2; \epsilon) \left(\frac{s}{4\pi\mu^2}\right)^\epsilon \frac{1}{\Gamma(2+\epsilon)} \left(\frac{1-z^2}{4}\right)^{\frac{\epsilon}{2}} x_1^\epsilon x_2^\epsilon. \quad (2.83)$$

⁷⁵⁵ Comparing with the Born cross-section in eq. (2.46) this can be written as:

$$\frac{d^2\sigma_r}{dx_1dx_2} = \frac{2\alpha_s\sigma_0}{3\pi} F(x_1, x_2; \epsilon) \left(\frac{s}{4\pi\mu^2}\right)^{\frac{\epsilon}{2}} \frac{1}{\Gamma(2+\frac{\epsilon}{2})} \left(\frac{1-z^2}{4}\right)^{\frac{\epsilon}{2}} x_1^\epsilon x_2^\epsilon. \quad (2.84)$$

⁷⁵⁶ Integrating over the allowed region of x_1 and x_2 :

$$\sigma_r = \frac{2\alpha_s\sigma_0}{3\pi} \left(\frac{s}{4\pi\mu^2}\right)^{\frac{\epsilon}{2}} \frac{1}{\Gamma(2+\frac{\epsilon}{2})} \int_0^1 dx_1 x_1^\epsilon \int_{1-x_1}^1 x_2^\epsilon \left(\frac{1-z^2}{4}\right)^{\frac{\epsilon}{2}} F(x_1, x_2; \epsilon). \quad (2.85)$$

⁷⁵⁷ We can define a change of variables $x_2 = 1 - vx_1$ to decouple these integrals since:

$$\left(\frac{1-z^2}{4}\right)^{\frac{\epsilon}{2}} = \frac{x_1^2(1+v^2) - 2vx_1 + 1}{(1-x_1)x_1v} + \epsilon \frac{x_1^2(1-v+v^2-x_1+1)}{(1-x_1)x_1v} \quad (2.86)$$

$$+ \frac{\epsilon^2}{4} \frac{x_1^2(v^2-2v+1) + 4(v-1)+1}{(1-x_1)xv}. \quad (2.87)$$

⁷⁵⁸ Substituting this into eq. (2.85) and performing the x_1 and v integrations gives:

$$\sigma_r = \frac{2\alpha_s\sigma_0}{3\pi} \left(\frac{s}{4\pi\mu^2} \right)^{\frac{\epsilon}{2}} \frac{\Gamma^2(1+\frac{\epsilon}{2})}{\Gamma(1+\frac{3\epsilon}{2})} \left[\frac{8}{\epsilon^2} - \frac{6}{\epsilon} + \frac{19}{2} \right]. \quad (2.88)$$

⁷⁵⁹ Further expanding the Gamma functions gives:

$$\sigma_r = \frac{2\alpha_s}{3\pi} \sigma_0 \left[\frac{8}{\epsilon^2} + \frac{1}{\epsilon} (-6 + 4\gamma_E + 4L) - \gamma_E(3 - \gamma_E) - \frac{57}{6} + \frac{7\pi^2}{6} + L^2 + (2\gamma_E - 3)L \right].$$

⁷⁶⁰ As in the case of the virtual corrections this is divergent in the limit $\epsilon \rightarrow 0$ and exhibits
⁷⁶¹ a residual dependence on μ .

⁷⁶² Cancellation of divergences

⁷⁶³ Having now found the vertex corrections and the real corrections up to $\mathcal{O}(\epsilon^2)$ we can
⁷⁶⁴ write the next-to-leading order cross-section by simply summing the two:

$$\sigma_{NLO} = \sigma_r + \sigma_v = \frac{\alpha_s}{\pi} \sigma_0. \quad (2.89)$$

⁷⁶⁵ So the total cross-section to next-to-leading order accuracy is:

$$\sigma = \sigma_0 \left(1 + \frac{\alpha_s}{\pi} \right) + \mathcal{O}(\alpha_s^2). \quad (2.90)$$

⁷⁶⁶ The fact that the infra-red divergences in both the real and virtual emission NLO
⁷⁶⁷ diagrams cancel is an example of the KLN theorem which states that the Standard
⁷⁶⁸ Model is completely free of infra-red divergences on the whole and holds true at all
⁷⁶⁹ orders.

⁷⁷⁰ **2.8.3 Resumming Higher-Order Corrections**

⁷⁷¹ So as we have seen we can evaluate the truncated perturbative series and, provided we
⁷⁷² remember to include higher multiplicity diagrams which contribute in the soft limit,
⁷⁷³ we will be left with a finite result which is invariant under gauge transformations.

⁷⁷⁴ It would seem then that this is the best way to proceed: we calculate as many corrections
⁷⁷⁵ as we can and reason that all of the higher-order terms we have neglected are suppressed
⁷⁷⁶ by powers of a small expansion parameter - the strong coupling, α_s . If this is indeed
⁷⁷⁷ the case we should see that each time we go to a higher-order in perturbation theory
⁷⁷⁸ our series begins to converge. E.g. the effect of the NNLO terms should be small
⁷⁷⁹ with respect to the NLO terms etc. It turns out that this true for all observables. To
⁷⁸⁰ motivate this we can give a schematic expansion of some variable we wish to calculate,
⁷⁸¹ \mathcal{O} :

$$\mathcal{O} = \dots \quad (2.91)$$

⁷⁸² **2.9 Parton showers for Monte-Carlo generators**

⁷⁸³ **2.10 Spinor-Helicity Notation**

⁷⁸⁴ It is convenient to work in Helicity-Spinor notation to evaluate Feynman diagrams in
⁷⁸⁵ the MRK limit [?]. As usual we have:

$$| p\pm \rangle = \psi_{\pm}(p) \quad \overline{\psi_{\pm}(p)} = \langle p\pm | . \quad (2.92)$$

⁷⁸⁶ Often the helicity information will be suppressed, and we define the following shorthand:

$$\langle pk \rangle = \langle p- | k+ \rangle \quad [pk] = \langle p+ | k- \rangle. \quad (2.93)$$

⁷⁸⁷ In this scheme we have the following identities:

$$\langle ij \rangle [ij] = s_{ij} \quad \langle i\pm | \gamma^\mu | i\pm \rangle = 2k_i^\mu \quad (2.94)$$

$$\langle ij \rangle = -\langle ji \rangle \quad [ij] = -[ji] \quad (2.95)$$

$$\langle ii \rangle = 0 \quad [ii] = 0 \quad (2.96)$$

$$\langle i\pm | \gamma^\mu | j\pm \rangle \langle k\pm | \gamma_\mu | l\pm \rangle = 2[ik]\langle lj \rangle \quad \langle k\pm | \gamma^\mu | l\pm \rangle = \langle l\mp | \gamma^\mu | k\mp \rangle \quad (2.97)$$

$$\langle ij \rangle \langle kl \rangle = \langle ik \rangle \langle lj \rangle + \langle il \rangle \langle kj \rangle \quad [ij][kl] = [ik][jl] + [il][kj] \quad (2.98)$$

$$\langle i+ | \not{k} | j+ \rangle = [ik]\langle kj \rangle \quad \langle i- | \not{k} | j- \rangle = \langle ik \rangle [kj] \quad (2.99)$$

788 Using the momentum for the partons outlined above and the on-shell condition for the
789 external partons, $|p_i^\perp| = p_i^+ p_i^-$, we have the following:

$$\langle ij \rangle = p_i^\perp \sqrt{\frac{p_j^+}{p_i^+} - p_j^\perp} \sqrt{\frac{p_i^+}{p_j^+}}, \quad \langle ai \rangle = -i \sqrt{-\frac{p_a^+}{p_i^+} p_i^\perp}, \quad \langle ib \rangle = i \sqrt{-p_b^- p_i^+}, \quad \langle ab \rangle = -\sqrt{\hat{s}}, \quad (2.100)$$

790 where \hat{s} is the partonic centre of mass energy. In the MRK limit eq. 19 simplifies to:

$$\langle ij \rangle \approx -p_j^\perp \sqrt{\frac{p_i^+}{p_j^+}}, \quad \langle ai \rangle \approx -i \sqrt{\frac{p_a^+}{p_i^+} p_i^\perp}, \quad \langle ib \rangle \approx i \sqrt{p_i^+ p_n^-}, \quad \langle ab \rangle \approx -\sqrt{p_1^+ p_n^-}. \quad (2.101)$$

791 2.10.1 Spinor-Helicity Calculations with Massive Partons

792 To do calculations with massive partons using the spinor-helicity formalism we must be
793 very careful since all of our favourite identities and tricks rely on the spinor brackets,
794 $|i\rangle$, representing massless partons with $p_i^2 = 0$. We begin by defining ‘fundamental
795 spinors’ [?] which we can use to build more general spinors and go from there. For
796 some k_0, k_1 satisfying $k_0^2 = 0, k_1^2 = -1$ and $k_0 \cdot k_1 = 0$ we can define positive and
797 negative helicity spinors as follows:

$$u_-(k_0)\bar{u}_-(k_0) \equiv \omega_- \not{k}_0 \quad (2.102a)$$

$$u_+(k_0) \equiv \not{k}_1 u_-(k_0), \quad (2.102b)$$

where $\omega_\lambda = \frac{1}{2}(1 + \lambda\gamma^5)$ is the helicity projection operator. In order for these to be valid spinors they must satisfy the following completeness relations:

$$\sum_{\lambda} u_{\lambda}(p)\bar{u}_{\lambda}(p) = \not{p} + m \quad (2.103a)$$

$$u_{\lambda}(p)\bar{u}_{\lambda}(p) = \omega_{\lambda}\not{p} \quad (2.103b)$$

The spinors in eq. can easily be shown to satisfy these as follows:

$$\begin{aligned} u_-(k_0)\bar{u}_-(k_0) + u_+(k_0)\bar{u}_+(k_0) &= \omega_- \not{k}_0 + \not{k}_1 u_-(k_0)\bar{u}_-(k_0) \not{k}_1, \\ &= \omega_- \not{k}_0 + \not{k}_1 \omega_- \not{k}_0 \not{k}_1, \\ &= \omega_- \not{k}_0 + \frac{1}{2}\gamma^{\mu}k_{1\mu}(1 - \gamma^5)\gamma^{\nu}k_{0\nu}\gamma^{\sigma}k_{1\sigma}, \\ &= \omega_- \not{k}_0 + \frac{1}{2}k_{1\mu}k_{0\nu}k_{1\sigma}(\gamma^{\mu}\gamma^{\nu}\gamma^{\sigma} - \gamma^{\mu}\gamma^5\gamma^{\nu}\gamma^{\sigma}), \\ &= \omega_- \not{k}_0 + \frac{1}{2}k_{1\mu}k_{0\nu}k_{1\sigma}(2\gamma^{\mu}g^{\nu\sigma} - \gamma^{\mu}\gamma^{\sigma}\gamma^{\nu} + 2\gamma^5\gamma^{\mu}g^{\nu\sigma} - \gamma^5\gamma^{\mu}\gamma^{\sigma}\gamma^{\nu}), \\ &= \omega_- \not{k}_0 + k_{1\mu}k_{0\nu}k_{1\sigma}\omega_+\gamma^{\mu}(2g^{\nu\sigma} - \gamma^{\sigma}\gamma^{\nu}), \\ &= \omega_- \not{k}_0 + 2\not{k}_1 k_0 \cdot k_1 - \omega_+ \not{k}_1 \not{k}_1 \not{k}_0, \\ &= \omega_- \not{k}_0 + \omega_+ \not{k}_0, \end{aligned}$$

where we have used $\gamma^{\mu}\gamma^{\mu} = 2g^{\mu\nu}$, $\gamma^{\mu}\gamma^5 = 0$ and $\not{k}_1 \not{k}_1 = k_1^2 = 0$. This proves the property of eq. 2.103b and inserting the definition of ω_{λ} gives:

$$\begin{aligned} u_-(k_0)\bar{u}_-(k_0) + u_+(k_0)\bar{u}_+(k_0) &= \frac{1}{2}(1 - \gamma^5)\not{k}_0 + (1 + \gamma^5)\not{k}_0, \\ &= \not{k}_0, \end{aligned}$$

Which is eq. 2.103a for a massless particle.

We can use these fundamental spinors to form spinors for any given momenta, p (which

805 has $p^2 = 0$), as follows:

$$u_\lambda(p) = \not{p} u_{-\lambda}(k_0) \frac{1}{\sqrt{2p \cdot k_0}}, \quad (2.106)$$

806 provided we don't have $p \cdot k_0 = 0$. Once again it is easy to show that this spinor satisfies
 807 the necessary conditions, for example:

$$\begin{aligned} u_\lambda(p) \bar{u}_\lambda(p) &= \frac{1}{2p \cdot k_0} \not{p} u_{-\lambda}(k_0) \bar{u}_{-\lambda}(p) \not{p}, \\ &= \frac{1}{2p \cdot k_0} \not{p} \omega_{-\lambda} \not{k}_0 \not{p}, \\ &= \frac{1}{4p \cdot k_0} \not{p} (1 - \lambda \gamma^5) \not{k}_0 \not{p}, \\ &= \frac{1}{2p \cdot k_0} p_\mu k_{0\nu} p_\sigma \omega_\lambda \gamma^\mu (2g^{\nu\sigma} - \gamma^\sigma \gamma^\nu), \\ &= \frac{1}{2p \cdot k_0} \omega_\lambda (2\not{p} p \cdot k_0 - \not{p} \not{p} \not{k}), \\ &= \omega_\lambda \not{p}. \end{aligned}$$

808 So far so good. This can also be generalised so that we can build massive spinors from
 809 our fundamental ones. We can use

$$u(q, s) = \frac{1}{\sqrt{2q \cdot k}} (\not{q} + m) u_-(k) \quad (2.108)$$

810 to describe a quark with spin 4-vector s , mass m and momentum q . To confirm this
 811 we go through the same procedure as above:

$$\begin{aligned}
 u_\lambda(p, s) \bar{u}_\lambda(p, s) &= \frac{1}{2q \cdot k_0} (\not{q} + m) u_-(k_0) \bar{u}_-(q) (\not{q} + m), \\
 &= \frac{1}{2q \cdot k_0} (\not{q} + m) \omega_- \not{k}_0 (\not{q} + m), \\
 &= \frac{1}{4q \cdot k_0} (\not{q} + m) (1 - \gamma^5) \not{k}_0 (\not{q} + m), \\
 &= \frac{1}{4q \cdot k_0} [(\not{q} \not{k}_0 \not{q} + m \not{k} \not{q} + m \not{q} \not{k}_0 + m^2 \not{k}) - \gamma^5 (\not{q} \not{k} \not{q} - m \not{k} \not{q} + m \not{q} \not{k}_0 - m^2 \not{k})], \\
 &= \frac{1}{2} \left(\not{q} + m - \gamma^5 \not{q} - m \gamma^5 + \frac{m \gamma^5 \not{k} \not{q}}{k \cdot q} + \frac{\gamma^5 m^2 \not{k}}{k \cdot q} \right), \\
 &= \frac{1}{2} \left(1 + \left(\frac{1}{m} \not{q} - \frac{m}{q \cdot k} \not{k} \right) \gamma^5 \right) (\not{q} + m), \\
 &= \frac{1}{2} (1 + \not{s} \gamma^5) (\not{q} + m),
 \end{aligned}$$

⁸¹² where the last line defines the spin vector $s = \frac{1}{m}q - \frac{m}{q \cdot k}k$. Conjecturing a similar form
⁸¹³ for an antiquark spinor with spin 4-vector s , mass m and momentum q :

$$v(q, s) = \frac{1}{\sqrt{2q \cdot k}} (\not{q} - m) u_-(k), \quad (2.110)$$

⁸¹⁴ which leads to:

$$\begin{aligned}
 v_\lambda(p, s) \bar{v}_\lambda(p, s) &= \frac{1}{2q \cdot k_0} (\not{q} - m) u_-(k_0) \bar{u}_-(q) (\not{q} - m), \\
 &= \frac{1}{2} \left((\not{q} - m) + \left(-\not{q} + m + \frac{m^2}{q \cdot k_0} \not{k}_0 - \frac{m}{q \cdot k_0} \not{q} \not{k}_0 \right) \gamma^5 \right), \\
 &= \frac{1}{2} (1 + \not{s} \gamma^5) (\not{q} - m).
 \end{aligned}$$

⁸¹⁵ One last check that is worth performing is that these spinors actually satisfy the Dirac
⁸¹⁶ eq. for both the quark and antiquark case. For the quark:

$$\not{q}u(q, s) = \frac{1}{2q \cdot k_0} \not{q}(\not{q} + m)u_-(k_0), \\ = \frac{1}{2q \cdot k_0} (m^2 + m\not{q})u_-(k_0),$$

817 we now define some momentum \tilde{q} by the relation $q = \tilde{q} + k_0$ such that $\tilde{q}^2 = 0$ and
818 $q \cdot k = \tilde{q} \cdot k$. Since $q^2 = 2\tilde{q} \cdot k = m^2$ we may write

$$\not{q}u(q, s) = \frac{1}{m} (m^2 + m\not{q})u_-(k_0), \\ = (m + \not{q})u_-(k_0),$$

819 we can now back substitute from the definition of $u(q, s)$ in eq. 2.108 to get:

$$\not{q}u(q, s) = \sqrt{2q \cdot k}u(q, s), \\ = mu(q, s),$$

820 which is the Dirac eq. for a quark. The result for antiquarks follows similarly. Now we
821 have forms for massive quarks and antiquarks in terms of massless spinors we can use
822 all of the spinor-helicity machinery to make our computations more efficient. Slightly
823 more useful forms of equations 2.108 and 2.110 can be found by decomposing q into
824 massless components once again: $q = \tilde{q} + k$ (once again this acts as a definition for \tilde{q}).
825 Then from eq. 2.108:

$$u(q, s) = \frac{1}{m} (\not{\tilde{q}} + \not{k} + m)u_-(k), \\ = \frac{1}{m} (|\tilde{q}^+\rangle\langle\tilde{q}^+|k^-\rangle + |\tilde{q}^-\rangle\langle\tilde{q}^-|k^-\rangle + |k^-\rangle\langle k^-|k^-\rangle + |k^-\rangle\langle k^-|k^-\rangle + m|k^-\rangle), \\ = \frac{[\tilde{q}k]}{m} |\tilde{q}^+\rangle + |k^-\rangle,$$

826 and similarly for the other helicities and the antiquarks:

$$u(q, -s) = \frac{\langle \tilde{q}k \rangle}{m} |\tilde{q}^- \rangle + |k^+ \rangle, \quad (2.116a)$$

$$v(q, s) = \frac{[\tilde{q}k]}{m} |\tilde{q}^+ \rangle - |k^- \rangle, \quad (2.116b)$$

$$v(q, -s) = \frac{\langle \tilde{q}k \rangle}{m} |\tilde{q}^- \rangle - |k^+ \rangle \quad (2.116c)$$

827 2.11 Monte Carlo Techniques

828 2.11.1 One Dimensional Integration

829 Integrals are ubiquitous in every field of physics and particle physics is no different.
830 We have already seen many examples where meaningful physical results can only be
831 obtained after computing an integral two good examples of this are the convolution of
832 the parton distribution functions with the partonic cross-section seen in section ?? and
833 the more complex multi-dimensional integrals seen in section ?? the calculation of the
834 one-loop correction to quark-antiquark production.

835 For some of the integrals derived here it is not always feasible (and sometimes not even
836 possible) to calculate them analytically. In these situations we must use a numerical
837 approach to approximate the full result. Such approaches generally fall into one of
838 two categories; quadrature or Monte-Carlo random sampling approaches. The most
839 appropriate solution depends the integrand itself (and in particular our prior knowledge
840 of the integrand) and the number of dimensions we are integrating over.

841 Here we briefly consider the one-dimensional case. Given an integral:

$$I = \int_a^b f(x) dx, \quad (2.117)$$

842 we can use well known results such as the Compound Simpson's Rule to approximate
843 the integral by

$$I \approx \frac{h}{3} \sum_{i=0}^{N/2} (f(x_{2i-2}) + 4f(x_{2i-1}) + f(x_{2i})) + \mathcal{O}(N^{-4}), \quad (2.118)$$

844 where N is the number of times we have subdivided the integral range (a, b) and

845 $x_i = a + \frac{i(b-a)}{N}$ are the points at which we sample the integrand. The error quoted
 846 on eq. 2.118 only shows the dependence on the sampling rate and it should be noted
 847 that there are other factors arising from the size of the domain of integration and on
 848 derivatives of the integrand, $f(x)$. The N^{-4} scaling of the error in this method makes
 849 it a good choice for numerics in one-dimension.

850 The Monte-Carlo approach to approximating eq. (2.117) would be to (pseudo-
 851)randomly select a series of N points, x_i , from within the domain of integration and
 852 then compute the integral as follows:

$$I \approx I_{MC} = \frac{b-a}{N} \sum_{i=0}^N f(x_i) + \mathcal{O}(N^{-\frac{1}{2}}). \quad (2.119)$$

853 Convergence of this result is assured by the weak law of large numbers (also known
 854 as Bernoulli's Theorem) which states that for a series of independent and identically
 855 distributed random variables, X_1, \dots, X_N , each with $\mathbb{E}(X_i) = \mu$ the sample mean
 856 approaches the population mean as $N \rightarrow \infty$. That is,

$$\lim_{N \rightarrow \infty} \frac{X_1 + \dots + X_N}{N} = \mu. \quad (2.120)$$

857 We can see this explicitly since the expectation of I_{MC} under the continuous probability
 858 density function p is:

$$\begin{aligned} \mathbb{E}_p[I_{MC}] &= \mathbb{E}_p \left[\frac{b-a}{N} \sum_{i=0}^N f(x_i) \right] \\ &= \frac{b-a}{N} \sum_{i=0}^N \mathbb{E}_p [f(x_i)] \\ &= \frac{b-a}{N} \sum_{i=0}^N \int_{-\infty}^{+\infty} f(x)p(x)dx \end{aligned}$$

where $p(x) = \frac{1}{b-a}$ is the uniform probability distribution for $x \in (a, b)$. Hence,

$$\begin{aligned} \mathbb{E}_p[I_{MC}] &= \frac{b-a}{N} \frac{1}{b-a} \sum_{i=0}^N \int_a^b f(x)dx \\ &= \int_a^b f(x)dx = I. \end{aligned}$$

859 Since the convergence of the Monte-Carlo approximation clearly scales significantly
 860 worse than the case for quadrature it would seem that it is not worth considering and,
 861 indeed, for a single dimension it is not. However, the picture changes when we consider
 862 integrals in dimension $d \geq 2$.

863 **2.11.2 Higher Dimensional Integration**

864 In the case of higher dimensional integrals e.g.

$$I = \int_{[a,b]} f(\vec{x}) d\vec{x} = \int_{x_1=a_1}^{x_1=b_1} \cdots \int_{x_n=a_n}^{x_n=b_n} f(x_1, \dots, x_n) dx_1 \dots dx_n, \quad (2.121)$$

865 we can still look to generalisations of the quadrature methods touched on in section
 866 2.11.1 however the convergence of these methods is less favourable. Quadrature
 867 methods have errors which scale with the number of dimensions we are integrating
 868 over, e.g. $\mathcal{O}(N^{-\frac{4}{d}})$ for the compound Simpson's rule. We can argue this intuitively
 869 since if we have N points in one dimension to get an error which scales as $\mathcal{O}(N^{-4})$ then
 870 in two dimensions we would require N^2 to achieve the same density of samplings and
 871 hence $N^2 \sim \mathcal{O}(N^{-4}) \implies N^2 \sim \mathcal{O}(N^{-\frac{4}{2}})$ and more generally $\mathcal{O}(N^{-\frac{4}{d}})$.

872 By comparison the error of a Monte Carlo approximation stays fixed at $\mathcal{O}(N^{-\frac{1}{2}})$
 873 regardless of the number of dimensions in the integrals. We are spared from this so-
 874 called ‘curse of dimensionality’ by the Central Limit Theorem which states that for a
 875 sequence of independent and identically distributed random variables X_1, \dots, X_N each
 876 with variance σ^2 we have:

$$\frac{X_1 + \dots + X_N - N\mathbb{E}(X_1)}{\sqrt{N}\sigma} \xrightarrow{\lim N \rightarrow \infty} \mathcal{N}(0, 1), \quad (2.122)$$

877 where $\mathcal{N}(0, 1)$ is the normal distribution with mean zero and variance 1. Then using
 878 the additive and multiplicative scaling of the normal distribution we see that:

$$\sum_{i=1}^N X_i \xrightarrow{\lim N \rightarrow \infty} \mathcal{N}\left(\mu, \frac{\sigma^2}{N}\right), \quad (2.123)$$

879 where μ is the mean of the variables X_i . The variance of a normal distribution is well
 880 known and we can use this to see that for a d -dimensional integral we can approximate
 881 our uncertainty as:

$$\int_{[a,b]} f(\vec{x}) d\vec{x} = V \langle f \rangle \pm V \sqrt{\frac{\langle f^2 \rangle - \langle f \rangle^2}{N}} \quad (2.124)$$

$$\equiv V \langle f \rangle \pm V \frac{\sigma_{MC}}{\sqrt{N}}, \quad (2.125)$$

where V is the volume of the domain of integration, $\langle f \rangle = \sum_i f(x_i)$ and $\langle f^2 \rangle = \sum_i f(x_i)^2$.

2.11.3 Variation Reduction Techniques

In equation 2.125 we saw that the error estimate of a Monte Carlo approximation depends not only on the number of points sampled, N , but also on σ_{MC} . We can try to reduce σ_{MC} by reducing how ‘variable’ the integrand is over the domain of integration, for instance in the extreme example where our integrand is $f(x) = f_0$, a constant, it is clear that one Monte Carlo sample is sufficient to compute the integral exactly. Previously when computing $\mathbb{E}_p[I_{MC}]$ we used a uniform probability density function but we are free to use any distribution we like to perform the integration. This can be seen since:

$$\begin{aligned} \mathbb{E}_p[I_{MC}] &= \int f(x)p(x)dx, \\ &= \int \frac{f(x)p(x)q(x)}{q(x)}, \\ &= \mathbb{E}_q \left[\frac{I_{MC}p(x)}{q(x)} \right], \end{aligned}$$

where $q(x)$ is our ‘importance sampling’ distribution. For example let us consider the integral

$$I = 150 \int_0^{\frac{1}{2}} x^2 \arcsin x^2 dx. \quad (2.126)$$

The integrand of eq. 2.126 is shown in fig. 2.4 along with two potential choices of density functions. The uniform distribution (shown in red) will sample the integrand equally across the domain however it is clear from looking at the functional form of

eq. 2.126 that that isn't the most efficient approach since it is strongly peaked towards the right hand side of the domain. Hence that is where the largest contribution to the Monte Carlo sum will come from. However if we sample the modified integrand using pseudo-random numbers generated from a distribution proportional to x^4 (shown in green in fig. 2.4) we can reduce the variance of our approximation significantly. Tab. 2.2 shows how the approximation improves as we vary the number of samples, N , for the two cases of $q \sim \mathcal{U}(0, 0.5)$ and $q \sim x^4$.

N	$q \sim \mathcal{U}(0.0, 0.5)$		$q \sim x^4$	
	Approximation	Error	Approximation	Error
10^1	0.5111428 ± 1.5932607	0.4318912	0.9424279 ± 1.6817093	0.0006061
10^2	0.9098668 ± 2.0212007	0.0331672	0.9429298 ± 2.6653523	0.0001042
10^3	0.9456974 ± 2.0415918	0.0026633	0.9431454 ± 0.8430513	8.936×10^{-5}
10^4	0.9438040 ± 2.0222993	0.0007699	0.9430386 ± 0.2665659	4.504×10^{-6}
10^5	0.9337252 ± 2.0040391	0.0093088	0.9430241 ± 0.0842942	2.848×10^{-6}

Table 2.2: The Monte-Carlo approximation to equation 2.126 as we vary the number of sampled points, N , shown in the naive sampling case and in the importance sampled case.

Tab. 2.2 clearly shows the value of an importance sampling approach convergences to the correct result much faster than when we sample uniformly. Of course this tactic relies on us having some prior knowledge of the behaviour of our integrand in order to select the correct probability density function to use which, in more complicated examples is not always possible³. A more realistic, and relevant, example of importance sampling comes from the cross-section for the production of a Z^0 boson in association with dijets. The matrix element squared for such a process will have following form upon factoring out the Z^0 propagator squared:

$$|\mathcal{M}_{Z^0+jj}|^2 \sim \left| \frac{1}{p_Z^2 - M_Z^2 + i\Gamma_Z M_Z} \right|^2 \times f(\text{QCD, EW}) \times g(\text{Kinematic}), \quad (2.127)$$

where p_Z is the momentum carried by the Z^0 boson, M_Z is its mass, Γ_Z is its width and $f(\text{QCD, EW})$ will contain all of the coupling information and $g(\text{Kinematic})$ encodes the remainder of the matrix element. When using a Monte-Carlo approach to generate events of this kind we can use the schematic of 2.127 to *a priori* select an appropriate probability density function to sample from. Fig. 2.5 shows the squared Z^0 propagator. Obvious comparisons with fig. 2.4 can be drawn in the sense that were we to generate

³More novel approaches whereby the sampling distribution is modified to improve convergence as the Monte-Carlo iterations are calculated, such as the VEGAS algorithm, exist but they will not be discussed here.

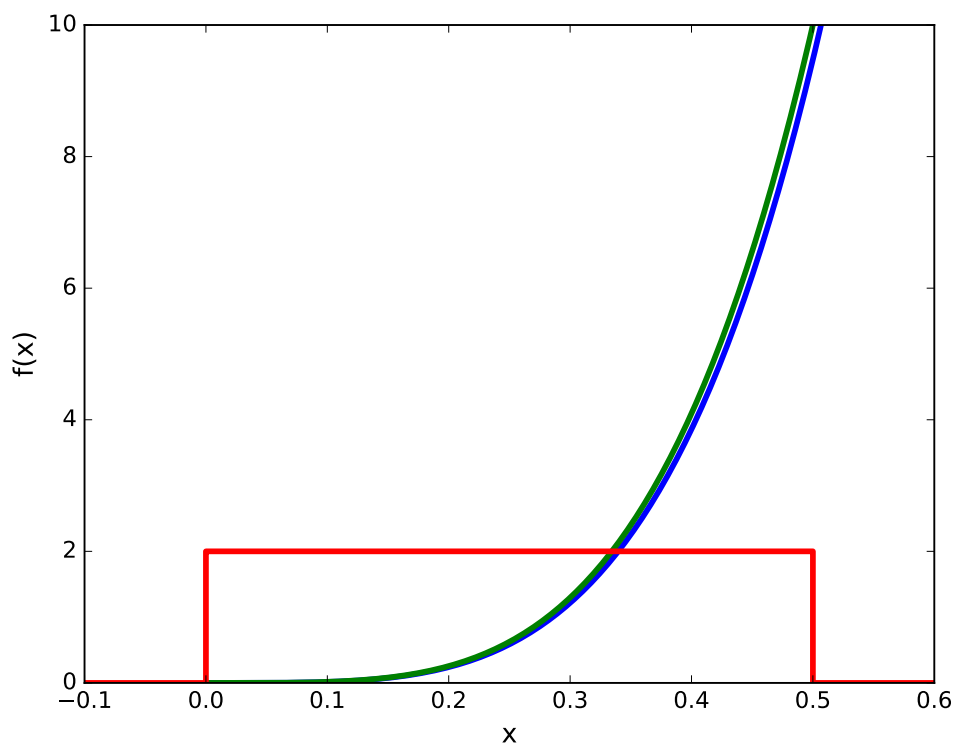


Figure 2.4: A simple importance sampling example (see equation 2.126). The integrand, $f(x)$, is shown in blue, the importance sampling distribution is shown in green and, for comparison, the uniform probability density function used in the naive case of no importance sampling is also shown (in red).

919 events with a uniform spread of values for p_Z^2 we would end with a very slow rate
 920 of convergence by oversampling areas where the integrand is very small and slowly
 921 varying.

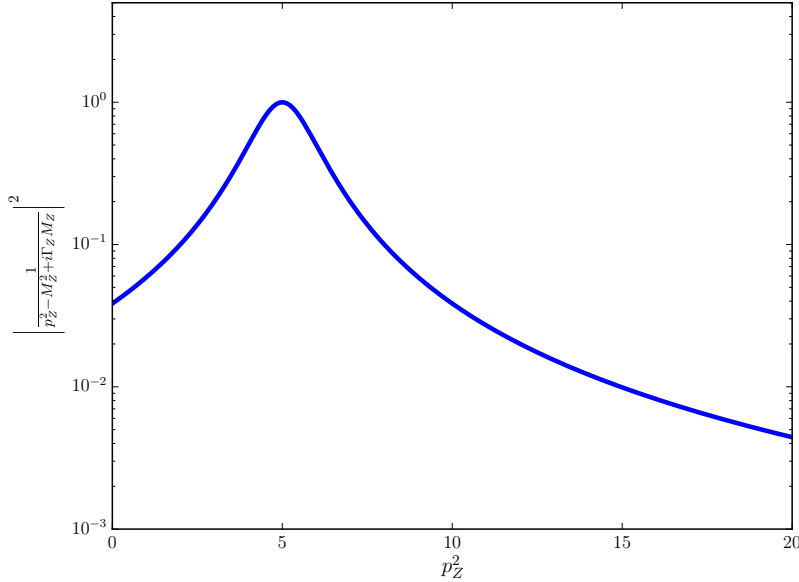


Figure 2.5: The absolute value squared of the Z^0 propagator for a range of values of the invariant mass squared of the Z^0 , p_Z^2 . We can see it is strongly peaked at the Z^0 mass and, as such, is an ideal candidate for using importance sampling.

922 Another good example of importance sampling is found in how we sample the incoming
 923 partons in our simulations. Simple momentum conservation considerations lead us to
 924 values for the Bjorken scaling variables of our incoming partons, x_a and x_b , and we can
 925 use these to intelligently sample the available partons. The naive way to perform the
 926 sum over all possible incoming states would be to uniformly choose a random number
 927 corresponding to one of the light quarks, one the light anti-quarks or to a gluon⁴. We
 928 can, however, do better than this by using what we know about how the parton density
 929 functions vary with $x_{a/b}$ - fig. ?? shows this behaviour as measured by the HERA
 930 experiment. By choosing to randomly sample then incoming parton types according
 931 to the relative values for the parton density functions we can, once again, reduce the
 932 variance of our numerical integrations as much as possible.

⁴By ‘light (anti-)quarks’ we mean all except the top and anti-top. The parton density functions for these are not available and, even if they were, they would be small enough that we could safely ignore their contribution to cross-sections.

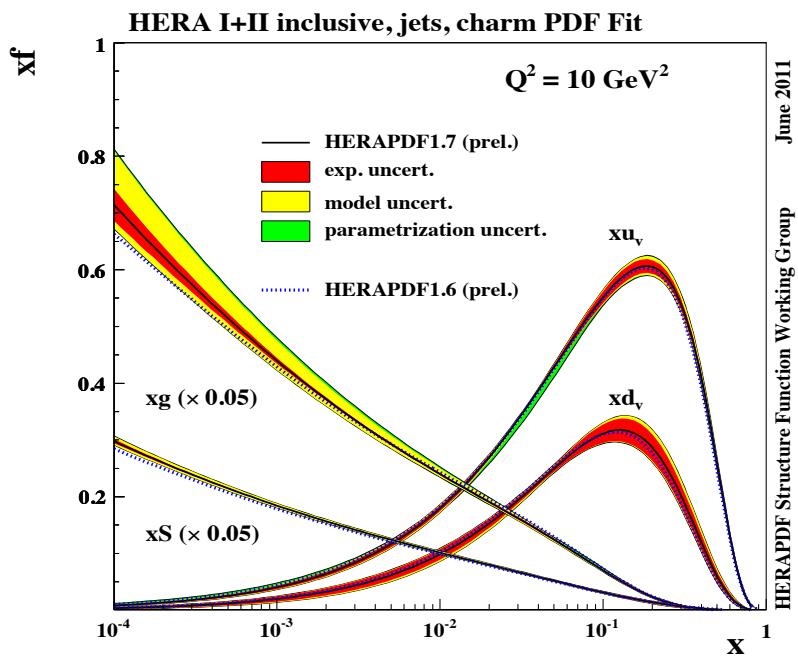


Figure 2.6: Recent parton distribution function fits from the HERA experiment. The observed variation in $f(x_{a/b}, Q^2)$, especially at high $x_{a/b}$, can be exploited when computing the equation ?? by using an importance sampling approach

933 **Chapter 3**

934 **High Energy QCD**

935 **3.1 The High Energy Limit of $2 \rightarrow 2$ QCD scattering**

936 **3.1.1 Mandelstam Variables in the High Energy Limit**

937 The $2 \rightarrow 2$ QCD scattering amplitudes can be expressed in terms of the well-known
938 Mandelstam variables s, t and u . Which, in terms of the momenta in the process, are
939 given by:

$$s = (p_1 + p_2)^2 \quad (3.1a)$$

$$t = (p_1 - p_2)^2 \quad (3.1b)$$

$$u = (p_2 - p_3)^2 \quad (3.1c)$$

940 When working in the high energy limit it is convenient to re-express these in terms of
941 the perpendicular momentum of the outgoing partons, p_\perp , and the difference in rapidity
942 between the two final state partons, Δy :

$$s = 4p_\perp^2 \cosh^2 \frac{\Delta y}{2} \quad (3.2a)$$

$$t = -2p_\perp^2 \cosh \frac{\Delta y}{2} e^{-\frac{\Delta y}{2}} \quad (3.2b)$$

$$u = -2p_\perp^2 \cosh \frac{\Delta y}{2} e^{\frac{\Delta y}{2}} \quad (3.2c)$$

943 In the limit of hard jets well separated in rapidity these can be approximated to give

$$s \approx p_{\perp}^2 e^{\Delta y} \quad (3.3a)$$

$$t \approx -p_{\perp}^2 \quad (3.3b)$$

$$u \approx -p_{\perp}^2 e^{\Delta y} \quad (3.3c)$$

⁹⁴⁴ From eq. (above) it is clear that the ‘hard, wide-angle jet’ limit is equivalent to the
⁹⁴⁵ High Energy limit since:

$$\Delta y \approx \ln \left(\frac{s}{-t} \right) \quad (3.4)$$

⁹⁴⁶ 3.1.2 HE limit of the three-gluon vertex

⁹⁴⁷ The three gluon vertex shown in fig. (X) has the following Feynman rule:

$$g_s f^{abc} ((p_1 + p_3)^{\nu} g^{\mu_1 \mu_3} + (q - p_3)^{\mu_1} g^{\mu_3 \nu} - (q + p_1)^{\mu_3} g^{\mu_1 \nu}) \quad (3.5)$$

⁹⁴⁸ In the high energy limit the emitted gluon with momenta q is much softer than the
⁹⁴⁹ emitting gluon with momenta p_1 i.e. $p_1^{\mu} \gg q^{\mu} \forall \mu$ and therefore $p_1 \sim p_3$ - using this we
⁹⁵⁰ can approximate the vertex by

$$\approx g_s f^{abc} (2p_1^{\nu} g^{\mu_1 \mu_3} + p_3^{\mu_1} g^{\mu_3 \nu} - p_3^{\mu_3} g^{\mu_1 \nu}) \quad (3.6)$$

⁹⁵¹ Furthermore, since the hard gluons in a high energy process are external they must
⁹⁵² satisfy the Ward identities; $\epsilon_1 \cdot p_1 = \epsilon_3 \cdot p_3 = 0$. Hence, the vertex can be expressed
⁹⁵³ simply as:

$$\approx 2g_s f^{abc} p_1^{\nu} g^{\mu_1 \mu_3} \quad (3.7)$$

⁹⁵⁴ 3.1.3 At Leading Order in α_s

⁹⁵⁵ Talk through the limit of $2 \rightarrow 2$ scattering of gluons. Introduce mandelstam variables,
⁹⁵⁶ show the equivalence of large delta y and large s.

⁹⁵⁷ **3.1.4 At Next-to-Leading Order in α_s**

⁹⁵⁸ Calculate the NLO calculations to the 2j ME and show that there explicitly is a delta
⁹⁵⁹ y (large log) enhancement.

⁹⁶⁰ **3.1.5 High Energy Jets ‘Currents’**

⁹⁶¹ **3.1.6 Effective Vertices For Real Emissions**

⁹⁶² **3.2 High Energy Jets**

⁹⁶³ **3.2.1 The Multi-Regge Kinematic limit of QCD amplitudes**

⁹⁶⁴ **3.2.2 Logarithms in HEJ observables**

⁹⁶⁵ Here you should take a $2 \rightarrow n$ ME, apply the HE limit to it, do a PS integration and
⁹⁶⁶ show the logs you get. Need the HE limit of PS integral from JA thesis and/or from
⁹⁶⁷ VDD talk

⁹⁶⁸ **3.2.3 HEJ currents**

⁹⁶⁹ **3.2.4 High Energy Phase-space Integration**

970 **Chapter 4**

971 **$Z/\gamma^* + \text{Jets}$ at the LHC**

972 • Rewrite the bits Jenni/Jeppe wrote.

973 The Large Hadron Collider (LHC) sheds ever more light on Standard Model processes
974 at higher energies as it continues into Run II. One “standard candle” process for the
975 validation of the Standard Model description in this new energy regime is the production
976 of a dilepton pair through an intermediate Z boson or photon, in association with (at
977 least) two jets [2–4, 27, 30, 50, 51]. This final state can be entirely reconstructed from
978 visible particles (in contrast to $pp \rightarrow \text{dijets} + (W \rightarrow e\nu)$) making it a particularly
979 clean channel for studying QCD radiation in the presence of a boson. Experimentally
980 this process is indistinguishable from the production of a virtual photon which has
981 decayed into the same products and we will consider both throughout.

982 W and Z/γ^* -production are excellent benchmark processes for investigating QCD
983 corrections, since the mass of the boson provides a perturbative scale, while the event
984 rates allow for jet selection criteria similar to those applied in Higgs boson studies.
985 $W, Z/\gamma^*$ -production in association with dijets is of particular interest, since in many
986 respects it behaves like a dijet production emitting a weak boson (i.e. electroweak
987 corrections to a QCD process rather than QCD corrections to a weak process). This
988 observation means that a study of $W, Z/\gamma^*$ -production in association with dijets is
989 relevant for understanding Higgs-boson production in association with dijets (which in
990 the gluon-fusion channel can be viewed as a Higgs-boson correction to dijet production).
991 This process is interesting (e.g. for CP -studies) in the region of phase space with
992 large dijet invariant mass, where the coefficients in the perturbative series have
993 logarithmically large contributions to all orders. As an example of the increasing
994 importance of the higher orders, it is noted that the experimental measurement of
995 the $N + 1/N$ -jet rate in $Z/\gamma^* + \text{jets}$ increases from 0.2 to 0.3 after application of very

996 modest VBF-style selection cuts even at 7 TeV [2, 3, 27].

997 The current state-of-the-art for fixed-order calculations for this process is the next-to-
 998 leading order calculation of Z/γ^* plus 4 jets by the BlackHat collaboration [47]. While
 999 it has become standard to merge next-to-leading order QCD calculations with parton
 1000 showers [9, 12, 37–39, 58], results for jet production in association with vector bosons
 1001 have so far only appeared with up to two jets [25, 60]. Indeed, $W/Z + 0-, 1-$ and
 1002 2-jet NLO samples have been merged with higher-order tree-level matrix elements
 1003 and parton shower formulations [36, 45]. However, a parton shower cannot be expected
 1004 to accurately provide a description of multiple hard jets from its resummation of the
 1005 (soft and collinear) logarithms which are enhanced in the region of small invariant
 1006 mass. An alternative method to describe the higher-order corrections is instead to sum
 1007 the logarithmic corrections which are enhanced at large invariant mass between the
 1008 particles. This is the approach pioneered by the High Energy Jets (HEJ) framework [15,
 1009 16]. Here, the hard-scattering matrix elements for a given process are supplemented
 1010 with the leading-logarithmic corrections (in s/t) at all orders in α_s . This approach
 1011 has been seen to give a good description of dijet and W plus dijet data at both the
 1012 TeVatron [8] and the LHC [1, 5, 6, 28, 29]. In particular, these logarithmic corrections
 1013 ensure a good description of W plus dijet-production in the region of large invariant
 1014 mass between the two leading jets [6]. It is not surprising that standard methods
 1015 struggle in the region of large invariant mass, since the perturbative coefficients receive
 1016 large logarithmic corrections to all orders, and perturbative stability is guaranteed only
 1017 once these are systematically summed.

1018 The purpose of this paper is to develop the treatment of such large QCD perturbative
 1019 corrections within High Energy Jets to include the process of Z/γ^* plus dijets. While
 1020 this process has many features in common with the W plus dijets process, one major
 1021 difference is the importance of interference terms, both between different diagrams
 1022 within the same subprocess (e.g. $qQ \rightarrow qQ(Z \rightarrow) e^+ e^-$ with emissions off either the
 1023 q or Q line) and between Z and γ^* processes of the same partonic configuration. For
 1024 processes with two quark lines, the possibility to emit the Z/γ^* from both of these leads
 1025 to profound differences to the formalism, since the t -channel momentum exchanged
 1026 between the two quark lines obviously differs whether the boson emission is off line q
 1027 or Q . Furthermore, the interference between the two resulting amplitudes necessitates
 1028 a treatment at the amplitude-level. High Energy Jets is formulated at the amplitude-
 1029 level, which, together with the matching to high-multiplicity matrix-elements, sets it
 1030 apart in the field of high energy logarithms [18, 26, 32, 34, 48, 49, 53–55]. The added
 1031 complication over earlier High Energy Jets-formalism (and indeed in any BFKL-related
 1032 study) by the interfering t -channels introduces a new structure of divergences in both

1033 real and virtual corrections, and therefore a new set of subtraction terms are needed,
1034 in order to organise the cancellation of these divergences. The matching to full high-
1035 multiplicity matrix elements puts the final result much closer to those of fixed order
1036 samples merged according to the shower formalism [25, 36, 45, 60] — although of course
1037 the logarithms systematically controlled with High Energy Jets are different to those
1038 controlled in the parton shower formalism. In particular, High Energy Jets remains a
1039 partonic generator, i.e. although it is an all-order calculation (like a parton shower), it
1040 is not interfaced to a hadronisation model. Initial steps in combining the formalism of
1041 High Energy Jets and that of a parton shower (and hadronisation) were performed in
1042 Ref. [14].

We begin the main body of this article by outlining the construction of a High Energy Jets amplitude and its implementation in a fully flexible parton level Monte Carlo in the next section. In section ?? we derive the new subtraction terms which allows us to fully account for interference between the amplitudes. The subtraction terms allow for the construction of the all-order contribution to the process as an explicit phase-space integral over any number of emissions. Specifically, the main result for the all-order summation is formulated in Eq. (??):

$$\sigma = \sum_{f_a, f_b} \sum_{n=2}^{\infty} \int \frac{d^3 p_a}{(2\pi)^3 2E_a} \int \frac{d^3 p_b}{(2\pi)^3 2E_b} \left(\prod_{i=2}^n \int_{p_{i\perp} > \lambda_{cut}} \frac{d^3 p_i}{(2\pi)^3 2E_i} \right) (2\pi)^4 \delta^{(4)} \left(p_a + p_b - \sum_i p_i \right) \\ \times | \mathcal{M}_{f_a f_b \rightarrow Z/\gamma^* f_a(n-2) g f_b}^{HEJ-reg}(p_a, p_b, \{p_i\}) |^2 \frac{x_a f_{fa}(x_a, Q_a) x_b f_{fb}(x_b, Q_b)}{\hat{s}^2} \Theta_{cut},$$

1043 where σ is the sough-after cross section, and the rest of the equation is discussed in
1044 the relevant section. Section ?? also discusses the necessary modifications in order
1045 to include fixed-order matching. In section ?? we show and discuss the comparisons
1046 between the new predictions obtained with High Energy Jets and LHC data. We
1047 conclude and present the outlook in section ??.

1048 4.1 $Z+jets$

1049 Similarly to the the case of W^\pm plus jets there are *four* possible emission sites for the
1050 boson; Two on the forward incoming quark, and two on the backward incoming quarks
1051 (see fig. 4.1).

1052 In the language of currents (see for *e.g.* [?]) we call the left hand side of fig. 4.1 j_μ^Z / γ^* :

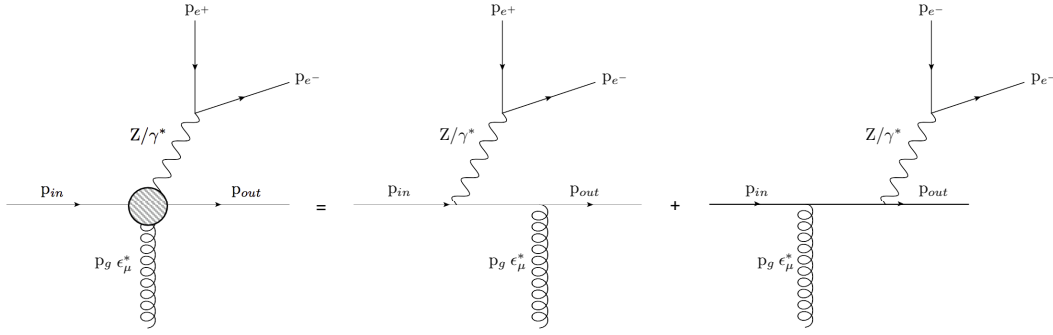


Figure 4.1: The possible emission sites for a neutral weak boson.

$$j_\mu^Z = \bar{u}^{h_{out}}(p_{out}) \left(\gamma^\sigma \frac{\not{p}_{out} + \not{p}_Z}{(p_{out} + p_Z)^2} \gamma_\mu + \gamma_\mu \frac{\not{p}_{in} - \not{p}_Z}{(p_{in} - p_Z)^2} \gamma_\sigma \right) u^{h_{in}}(p_{in}) \times \bar{u}^{h_{e^-}}(p_{e^-}) \gamma_\sigma u^{h_{e^+}}(p_{e^+}). \quad (4.1)$$

1053 We can then express amplitudes in terms of contractions of ‘emitting’ and ‘non-emitting’
 1054 currents.

1055 As the fig. above indicates, when emitting a Z boson there is also the possibility of
 1056 an off-shell photon being exchanged instead of a Z . Since the difference in these two
 1057 channels is indistinguishable in the final state we must treat the interference as the
 1058 amplitude level. For example, the amplitude for $2 \rightarrow 2$ scattering is:

$$\mathcal{A}_{Z/\gamma}^{2 \rightarrow 2} = \underbrace{\left(\frac{k_1}{p_{Z/\gamma}^2 - m_Z^2 + i\Gamma_Z m_Z} + \frac{Q_1 e}{p_{Z/\gamma}^2} \right)}_{\mathcal{K}_a} \frac{j_1^{Z/\gamma} \cdot j_2}{q_{t1}^2} + \underbrace{\left(\frac{k_2}{p_{Z/\gamma}^2 - m_Z^2 + i\Gamma_Z m_Z} + \frac{Q_2 e}{p_{Z/\gamma}^2} \right)}_{\mathcal{K}_b} \frac{j_1 \cdot j_2^{Z/\gamma}}{q_{b1}^2}, \quad (4.2)$$

1059 where k_i are the Z couplings to the quarks, Q_i are the the γ couplings to the quarks,
 1060 m_Z is the mass of the Z , Γ_Z is the width of the Z peak, q_{t1} is the momentum of
 1061 the t -channel gluon exchanged when Z emission occurs of the forward incoming quark
 1062 line and q_{b1} is the momentum of the exchanged gluon when Z emission occurs of the
 1063 backward incoming quark line.

1064 Eq. (4.2) is a good example of the advantages of using currents since the form of the
 1065 diagrams for either Z or γ can be expressed as only two contraction (with the distinct
 1066 propagators dealt with in the \mathcal{K}_i terms).

1067 Extra *real* gluon emissions from the t -channel gluon are then included using an effective
 1068 vertex of the form [?] [?]:

$$V^\rho(q_j, q_{j+1}) = -(q_j + q_{j+1})^\rho - 2 \left(\frac{s_{aj}}{s_{ab}} - \frac{q_{j+1}^2}{s_{bj}} \right) p_b^\rho + 2 \left(\frac{s_{bj}}{s_{ab}} + \frac{q_j^2}{s_{aj}} \right) p_a^\rho, \quad (4.3)$$

1069 where $s_{aj} = 2p_a \cdot p_j$ etc. The general $2 \rightarrow n$ amplitude therefore looks like:

$$\begin{aligned} \mathcal{A}_{Z/\gamma}^{2 \rightarrow n} = & \left(\mathcal{K}_a \frac{V^{\mu_1}(q_{t1}, q_{t2}) \cdots V^{\mu_{n-2}}(q_{t(n-1)}, q_{t(n-2)})}{q_{t1} \cdots q_{t(n-1)}} j_1^Z \cdot j_2 + \dots \right. \\ & \left. \mathcal{K}_b \frac{V^{\mu_1}(q_{b1}, q_{b2}) \cdots V^{\mu_{n-2}}(q_{b(n-1)}, q_{b(n-2)})}{q_{b1} \cdots q_{b(n-1)}} j_1 \cdot j_2^Z \right) \epsilon_{\mu_1}^* \cdots \epsilon_{\mu_{(n-2)}}^* \end{aligned} \quad (4.4)$$

1070 and after taking the modulus squared of this we have the following:

$$\begin{aligned} |\mathcal{A}_{Z/\gamma}^{2 \rightarrow n}|^2 = & \left| \mathcal{K}_a j_1^{Z/\gamma} \cdot j_2 \right|^2 \frac{V^2(q_{t1}, q_{t2}) V^2(q_{t2}, q_{t3}) \cdots V^2(q_{b(n-2)}, q_{b(n-1)})}{q_{t1}^2 \cdots q_{t(n-1)}^2} + \dots \\ & \left| \mathcal{K}_b j_2^{Z/\gamma} \cdot j_1 \right|^2 \frac{V^2(q_{b1}, q_{b2}) V^2(q_{b2}, q_{b3}) \cdots V^2(q_{b(n-2)}, q_{b(n-1)})}{q_{b1}^2 \cdots q_{b(n-1)}^2} + \dots \\ & 2\Re \{ \mathcal{K}_a \overline{\mathcal{K}_b} \times (j_1^{Z/\gamma} \cdot j_2) (\overline{j_2^{Z/\gamma} \cdot j_1}) \} \frac{V(q_{t1}, q_{t2}) \cdot V(q_{b1}, q_{b2}) \cdots V(q_{t(n-2)}, q_{t(n-1)}) \cdot V(q_{b(n-2)}, q_{b(n-1)})}{q_{t1} q_{b1} \cdots q_{t(n-1)} q_{b(n-1)}} \end{aligned} \quad (4.5)$$

1071 In previous work it was seen that the interference between forward quark- and backward
1072 weak boson emission (the third term in eq. (4.5)) was negligible [?]. This turns out
1073 not to be the case in Z plus jets - possibly due to the effects of photon interference.

1074 4.1.1 Formulation in terms of currents

1075 4.1.2 To High Multiplicity Final States

1076 4.1.3 Z^0 Emission Interference

1077 4.1.4 Photonic Interference

1078 4.1.5 The $2 \rightarrow n$ Matrix Element

1079 4.1.6 The Differential Z/γ Cross-Section

1080 4.2 Regularising the $Z/\gamma^* + \text{Jets}$ Matrix Element

1081 Explain that in the MRK limit the external legs can't (by definition) be soft, then look
1082 at the limit of one gluon going soft (basically an NLO correction to the ($n-1$) parton
1083 ME) in the effective vertex. Show that this leads to a divergence.

1084 Next talk about NLO virtual corrections to the ($n-1$)-parton ME. Show that in the HE
1085 limit, only two diagrams contribute (extra t - crosses and uncrossed - g exchange) show
1086 the log enhancement given. Give explicitly calculation showing divergences cancelling
1087 (as must happen by KLN theorem).

1088 4.2.1 Soft Emissions

1089 To calculate useful quantities such as cross sections *etc.* we must integrate equation (4.5)
1090 over all of phase space. However, problems arise when we attempt to integrate over
1091 the so called 'soft' (low energy) regions of phase space - things which should be finite
1092 diverge and need to be cancelled carefully. It is well understood that the divergences
1093 coming from soft *real* emissions cancel with those coming from soft *virtual* emissions
1094 and so we must explicitly show this cancellation and calculate the remaining finite
1095 contribution multiplying the ($n-1$)-final state parton matrix element.

1096 In the previous work on W^\pm emission the finite contribution was found to be [?][?]:

$$\frac{\alpha_s C_a \Delta_{j-1,j+1}}{\pi} \ln \frac{\lambda^2}{|\vec{q}_{j\perp}|^2}, \quad (4.6)$$

1097 where α_s is the strong coupling strength, C_a is a numerical factor, $\Delta_{i-1,i+1}$ is the
1098 rapidity span of the final state partons either side of our soft emission, λ is a factor

1099 chosen to define the soft region: $p^2 < \lambda^2$ and $|\vec{q}_{j\perp}|^2$ is the sum of squares of the
 1100 transverse components of the j^{th} t -channel gluon momenta.

1101 Here we investigate the cancellation of these divergences for Z emission and most
 1102 importantly whether the finite term is of the same form for the interference term which
 1103 was previously disregarded.

1104 We start by looking at a $2 \rightarrow n$ process and take the limit of one final state parton
 1105 momentum, p_i , becoming small. Because of the form of eq. (4.5) this amounts to
 1106 looking at the effect of soft-ness on eq. (4.3), we can immediately see that for p_i going
 1107 soft the gluon chain momenta coming into- and coming out of the j^{th} emission site will
 1108 coincide: $q_{j+1} \sim q_j$:

$$V^\rho(q_j, q_{j+1}) \rightarrow -2q_j^\rho - 2 \left(\frac{s_{aj}}{s_{ab}} - \frac{q_j^2}{s_{bj}} \right) p_b^\rho + 2 \left(\frac{s_{bj}}{s_{ab}} + \frac{q_j^2}{s_{aj}} \right) p_a^\rho \quad (4.7)$$

1109 In eq. (4.5) we have two types of terms involving the effective vertex; terms like
 1110 $V^2(q_{t/bj}, q_{t/b(j+1)})$ and terms like $V(q_{tj}, q_{t(j+1)}) \cdot V(q_{bj}, q_{b(j+1)})$. The procedure for the
 1111 V^2 terms doesn't change between top-line emission and bottom-line emission and
 1112 so only the calculation for top-line emission will be shown here.

1113 4.2.2 $V^2(q_{tj}, q_{t(j+1)})$ Terms

1114 Once we square eq. (4.7) and impose on-shell conditions to p_a and p_b we get:

$$V^2(q_{tj}, q_{tj}) = 4q_j^2 + 8q_j \cdot p_b \left(\frac{s_{aj}}{s_{ab}} - \frac{q_j^2}{s_{bj}} \right) - 8q_j \cdot p_a \left(\frac{s_{bj}}{s_{ab}} + \frac{q_j^2}{s_{aj}} \right) - 4s_{ab} \left(\frac{s_{aj}}{s_{ab}} - \frac{q_j^2}{s_{bj}} \right) \left(\frac{s_{bj}}{s_{ab}} + \frac{q_j^2}{s_{aj}} \right) \quad (4.8)$$

1115 Now since $p_j \rightarrow 0$ the terms s_{aj} and s_{bj} will also become vanishing:

$$V^2(q_{tj}, q_{tj}) = 4q_j^2 + 8q_j \cdot p_b \frac{q_j^2}{s_{bj}} - 8q_j \cdot p_a \frac{q_j^2}{s_{aj}} - 4s_{ab} \frac{q_j^4}{s_{bj}s_{aj}} \quad (4.9)$$

1116 Clearly the final term now dominates due to its $\sim \frac{1}{p_i^2}$ behaviour:

$$V^2(q_{ti}, q_{ti}) = -\frac{4s_{ab}}{s_{bi}s_{ai}} q_i^4 + \mathcal{O}\left(\frac{1}{|p_i|}\right) \quad (4.10)$$

1117 We must now explicitly calculate the invariant mass terms. Since we are in the high

1118 energy limit we may take $p_a \sim p_1 \sim p_+ = (\frac{1}{2}p_z, 0, 0, \frac{1}{2}p_z)$ and $p_b \sim p_n \sim p_- =$
1119 $(\frac{1}{2}p_z, 0, 0, -\frac{1}{2}p_z)$ and we describe our soft gluon by $p_i = (E, \vec{p})$. Therefore:

$$s_{ai} = 2p_a \cdot p_i \sim 2p_+ \cdot p_i = \frac{1}{2}p_z E - \frac{1}{2}p_z^2, \quad (4.11a)$$

$$s_{bi} = 2p_b \cdot p_i \sim 2p_- \cdot p_i = \frac{1}{2}p_z E + \frac{1}{2}p_z^2, \quad (4.11b)$$

1120 and $s_{ab} = \frac{1}{2}p_z^2$. Then eq. (4.10) reads:

$$V^2(q_{ti}, q_{ti}) = -\frac{4p_z^2}{(p_z E - p_z^2)(p_z E + p_z^2)} q_i^4 + \mathcal{O}\left(\frac{1}{|p_i|}\right), \quad (4.12a)$$

$$V^2(q_{ti}, q_{ti}) = -\frac{4p_z^2}{p_z^2(E^2 - p_z^2)} q_i^4 + \mathcal{O}\left(\frac{1}{|p_i|}\right), \quad (4.12b)$$

1121 but since $E^2 - p_1^2 = 0$:

$$V^2(q_{ti}, q_{ti}) = -\frac{4}{|\vec{p}_{1\perp}|^2} q_i^4 + \mathcal{O}\left(\frac{1}{|p_i|}\right), \quad (4.13)$$

1122 Now looking back to eq. (4.5) we see that each vertex is associated with factors of
1123 $(q_{ti}^{-2} q_{t(i+1)}^{-2})$ but once again since the emission is soft this becomes (q_{ti}^{-4}) . This factor
1124 conspires to cancel with that in eq. (4.13), moreover each vertex comes with a factor
1125 of $-C_A g_s^2$ (which are contained in the \mathcal{K}_i terms in eq. (4.5)). Including these and
1126 dropping subdominant terms the final factor is:

$$\frac{4C_A g_s^2}{|\vec{p}_{\perp}|^2} \quad (4.14)$$

1127 4.2.3 $V(q_{ti}, q_{t(i+1)}) \cdot V(q_{bi}, q_{b(i+1)})$ Terms

1128 The calculation of the interference term with a soft emission follows similarly to the
1129 above section. After taking $p_i \rightarrow 0$ and dotting the two vertex terms together we have:

$$\begin{aligned} V(q_{ti}, q_{ti}) \cdot V(q_{bi}, q_{bi}) &= 4q_i^t \cdot q_i^b - 4q_i^t \cdot p_a \left(\frac{s_{bi}}{s_{ab}} + \frac{t_i^b}{s_{ai}} \right) + 4q_i^t \cdot p_b \left(\frac{s_{ai}}{s_{ab}} + \frac{t_i^b}{s_{bi}} \right) \dots \\ &\quad - 4q_i^b \cdot p_a \left(\frac{s_{bi}}{s_{ab}} + \frac{t_i^t}{s_{ai}} \right) + 4q_i^b \cdot p_b \left(\frac{s_{ai}}{s_{ab}} + \frac{t_i^t}{s_{bi}} \right) \dots \end{aligned} \quad (4.15)$$

1130 having use $p_a^2 = 0$ and $p_b^2 = 0$ once again. We can drop all the terms with s_{ai} or s_{bi} in
 1131 the denominator and this time we are left with *two* dominant terms which combine to
 1132 give:

$$V(q_{ti}, q_{ti}) \cdot V(q_{bi}, q_{bi}) = -\frac{s_{ab}}{s_{ai}s_{bi}} t_i^t t_i^b + \mathcal{O}\left(\frac{1}{|p_i|}\right). \quad (4.16)$$

1133 The invariant mass terms here are identical to those we saw in the V^2 terms and the
 1134 products of $t_i^t t_i^b$ also appear in the denominator of the interference term in eq. (4.5).
 1135 After this cancelling we are left with exactly what we had before (see eq. (4.14)). Since
 1136 exactly the same factor comes from all three terms at the amplitude squared level we
 1137 may factor them out and express the amplitude squared for an n -parton final state with
 1138 one soft emission in terms of an $(n-1)$ -parton final state amplitude squared multiplied
 1139 by our factor:

$$\lim_{p_i \rightarrow 0} |\mathcal{A}_{Z/\gamma}^{2 \rightarrow n}|^2 = \left(\frac{4C_A g_s^2}{|\vec{p}_{i\perp}|^2} \right) |\mathcal{A}_{Z/\gamma}^{2 \rightarrow (n-1)}|^2 \quad (4.17)$$

1140 4.2.4 Integration of soft diverences

1141 As mentioned above the divergences only become apparent after we have attempted to
 1142 integrate over phase space. The Lorentz invariant phase space integral associated with
 1143 p_i is:

$$\int \frac{d^3 \vec{p}_i}{(2\pi)^3 2E_i} \frac{4C_A g_s^2}{|\vec{p}_{i\perp}|^2}. \quad (4.18)$$

1144 It is convenient to replace the integral over the z -component of momentum with one
 1145 over rapidity, y_2 . Rapidity and momentum are related through:

$$y = \frac{1}{2} \ln \left(\frac{E + p_z}{E - p_z} \right) \quad (4.19)$$

1146 The Jacobian of this transformation is:

$$\frac{dy}{dp_z} = \frac{1}{2(E+p_z)} \frac{\partial}{\partial p_z}(E+p_z) - \frac{1}{2(E-p_z)} \frac{\partial}{\partial p_z}(E-p_z), \quad (4.20)$$

$$= \frac{E}{E^2 - p_z^2} - \frac{p_z}{E^2 - p_z^2} \frac{\partial E}{\partial p_z}, \quad (4.21)$$

$$= \frac{E}{E^2 - p_z^2} - \frac{p_z}{E^2 - p_z^2} \frac{p_z}{E}, \quad (4.22)$$

$$= \frac{1}{E}. \quad (4.23)$$

1147 The phase space integral then reads:

$$\int \frac{d^{2+2\epsilon} \vec{p}_\perp}{(2\pi)^{2+2\epsilon}} \frac{dy}{4\pi} \frac{4C_A g_s^2}{|\vec{p}_\perp|^2} \mu^{-2\epsilon} = \frac{4C_A g_s^2 \mu^{-2\epsilon}}{(2\pi)^{2+2\epsilon} 4\pi} \Delta_{i-1,i+1} \int \frac{d^{2+2\epsilon} \vec{p}_\perp}{|\vec{p}_\perp|^2}, \quad (4.24)$$

1148 where we have analytically continued the integral to $2 + 2\epsilon$ dimensions to regulate the
1149 divergence and introduced the parameter μ to keep the coupling dimensionless in the
1150 process. Converting to polar coordinates and using the result for the volume of a unit
1151 hypersphere gives to integrated soft contribution:

$$\frac{4C_A g_s^2}{(2\pi)^{2+2\epsilon} 4\pi} \Delta_{i-1,i+1} \frac{1}{\epsilon} \frac{\pi^{1+\epsilon}}{\Gamma(\epsilon+1)} \left(\frac{\lambda^2}{\mu^2} \right)^\epsilon \quad (4.25)$$

1152 4.2.5 Virtual Emissions

1153 The virtual emission diagrams are included using the Lipatov ansatz for the gluon
1154 propagator:

$$\frac{1}{q_i^2} \longrightarrow \frac{1}{q_i^2} e^{\hat{\alpha}(q_i)(\Delta_{i,i-1})}, \quad (4.26)$$

1155 where:

$$\hat{\alpha}(q_i) = \alpha_s C_A q_i^2 \int \frac{d^{2+2\epsilon} k_\perp}{(2\pi)^{2+2\epsilon}} \frac{1}{k_\perp^2 (k_\perp - q_{i\perp})^2} \mu^{-2\epsilon}. \quad (4.27)$$

1156 Once again we choose to perform the integral using dimensional regularisation. Using
1157 the well known Feynman parameterisation formulae gives:

$$\hat{\alpha}(q_i) = \alpha_s C_A q_i^2 \int \frac{d^{2+2\epsilon} k_\perp}{(2\pi)^{2+2\epsilon}} \int_0^1 \frac{dx}{[x(k - q_i)_\perp^2 + (1-x)k_\perp^2]^2} \mu^{-2\epsilon}, \quad (4.28)$$

$$= \alpha_s C_A q_i^2 \int \frac{d^{2+2\epsilon} \hat{k}_\perp}{(2\pi)^{2+2\epsilon}} \int_0^1 \frac{dx}{[\hat{k}_\perp^2 + q_{i\perp}^2(1-x)]^2} \mu^{-2\epsilon}, \quad (4.29)$$

1158 where we have performed a change of variables to $\hat{k}_\perp = k_\perp - x q_{i\perp}$ with unit Jacobian.
 1159 Changing the order of integration we can perform the \hat{k}_\perp integral using the following
 1160 result:

$$\int \frac{d^d k}{(2\pi)^d} \frac{1}{(k^2 - C)^\alpha} = \frac{1}{(4\pi)^{\frac{d}{2}}} \frac{\Gamma(\alpha - \frac{d}{2})}{\Gamma(\alpha)} \frac{(-1)^\alpha}{C^{\alpha - \frac{d}{2}}}, \quad (4.30)$$

1161 to give:

$$\hat{\alpha}(q_i) = \alpha_s C_A q_i^2 \frac{\Gamma(1-\epsilon)}{(4\pi)^{1+\epsilon}} (-q_{i\perp}^2)^{\epsilon-1} \int_0^1 dx (1-x)^{\epsilon-1}, \quad (4.31)$$

$$= -\frac{2g_s^2 C_A}{(4\pi)^{2+\epsilon}} \frac{\Gamma(1-\epsilon)}{\epsilon} \left(\frac{q_{i\perp}^2}{\mu^2} \right)^\epsilon, \quad (4.32)$$

1162 having completed the x integral and used $\alpha_s = \frac{g_s^2}{4\pi}$.

1163 4.2.6 Cancellation of Infrared Contributions

1164 We now show how the infrared contributions from soft real emissions and virtual
 1165 emissions cancel leaving our integrated matrix element finite. The subtlety here is
 1166 that we must sum two diagrams with different final states to see the cancellation.
 1167 This is because they are experimentally indistinguishable; the $2 \rightarrow (n-1)$ virtual
 1168 diagram has $(n-1)$ resolvable partons in the final state (but is a higher order diagram
 1169 perturbatively speaking). Because one of the emission in the real $2 \rightarrow n$ diagram is
 1170 soft it is experimentally undetectable so we detect the same final state as the virtual
 1171 diagram. The matrix element squared for the real soft diagram will look like:

$$|\mathcal{A}_{Z/\gamma}^{2 \rightarrow n}|^2 = \left(\frac{4g_s^2 C_a}{|p_{i\perp}|^2} \right) \left[\left| \mathcal{K}_a j_1^{Z/\gamma} \cdot j_2 \right|^2 \frac{\prod_{i \neq j}^{n-2} V^2(q_{ti}, q_{t(i+1)})}{\prod_{i \neq j}^{n-1} q_{ti}^2} + \dots \right] \quad (4.33)$$

$$\left| \mathcal{K}_b j_2^{Z/\gamma} \cdot j_1 \right|^2 \frac{\prod_{i \neq j}^{n-2} V^2(q_{bi}, q_{b(i+1)})}{\prod_{i \neq j}^{n-1} q_{bi}^2} + \dots \quad (4.34)$$

$$2\Re\{\mathcal{K}_a \overline{\mathcal{K}_b} \times (j_1^{Z/\gamma} \cdot j_2)(\overline{j_2^{Z/\gamma} \cdot j_1})\} \frac{\prod_{i \neq j}^{n-2} V(q_{ti}, q_{t(i+1)}) \cdot V(q_{bi}, q_{b(i+1)}))}{\prod_{i \neq j}^{n-1} q_{ti} q_{bi}} \Big], \quad (4.35)$$

where we have taken the i^{th} gluon to be soft and the result of the Lorentz invariant phase space integration over the p_i momentum is shown in eq. (4.25).

After inserting the Lipatov ansatz into the $2 \rightarrow (n-1)$ matrix element squared we have:

$$|\mathcal{A}_{Z/\gamma}^{2 \rightarrow (n-1)}|^2 = \left| \mathcal{K}_a j_1^{Z/\gamma} \cdot j_2 \right|^2 \frac{\prod_i^{n-3} V^2(q_{ti}, q_{t(i+1)})}{\prod_i^{n-2} q_{ti}^2} e^{2\hat{\alpha}(q_{ti})\Delta_{i-1,i+1}} + \dots \quad (4.36)$$

$$\left| \mathcal{K}_b j_2^{Z/\gamma} \cdot j_1 \right|^2 \frac{\prod_i^{n-3} V^2(q_{bi}, q_{b(i+1)})}{\prod_i^{n-2} q_{bi}^2} e^{2\hat{\alpha}(q_{bi})\Delta_{i-1,i+1}} + \dots \quad (4.37)$$

$$2\Re\{\mathcal{K}_a \overline{\mathcal{K}_b} \times (j_1^{Z/\gamma} \cdot j_2)(\overline{j_2^{Z/\gamma} \cdot j_1})\} \frac{\prod_i^{n-3} V(q_{ti}, q_{t(i+1)}) \cdot V(q_{bi}, q_{b(i+1)}))}{\prod_i^{n-2} q_{ti} q_{bi}} e^{(\hat{\alpha}(q_{bi}) + \hat{\alpha}(q_{ti}))\Delta_{i-1,i+1}}, \quad (4.38)$$

We can now go through term-by-term to show the divergences cancel and find the finite contribution to the matrix element squared. Similarly to when we calculated the soft terms the pure top and bottom emissions follow identically so here we will only state the procedure for the top emission. The interference term is slightly different.

For the top line emission we have the following terms:

$$\frac{4C_A g_s^2}{(2\pi)^{2+2\epsilon} 4\pi} \Delta_{i-1,i+1} \frac{1}{\epsilon} \frac{\pi^{1+\epsilon}}{\Gamma(\epsilon+1)} \left(\frac{\lambda^2}{\mu^2} \right)^\epsilon + e^{2\hat{\alpha}_s(q_{ti})\Delta_{i-1,i+1}}. \quad (4.39)$$

We now extract the relevant term (in terms of the strong coupling order) from the exponential and substitute the expression for $\hat{\alpha}_s$:

$$= \frac{4C_A g_s^2}{(2\pi)^{2+2\epsilon} 4\pi} \Delta_{i-1,i+1} \frac{1}{\epsilon} \frac{\pi^{1+\epsilon}}{\Gamma(\epsilon+1)} \left(\frac{\lambda^2}{\mu^2} \right)^\epsilon - - \frac{2g_s^2 C_A}{(4\pi)^{2+\epsilon}} \frac{\Gamma(1-\epsilon)}{\epsilon} \left(\frac{q_{ti\perp}^2}{\mu^2} \right)^\epsilon, \quad (4.40)$$

$$= \frac{g_s^2 C_A}{4^{1+\epsilon} \pi^{2+\epsilon}} \Delta_{i-1,i+1} \left(\frac{1}{\epsilon \Gamma(1+\epsilon)} \left(\frac{\lambda^2}{\mu^2} \right)^\epsilon - \frac{\Gamma(1-\epsilon)}{\epsilon} \left(\frac{q_{ti\perp}^2}{\mu^2} \right)^\epsilon \right). \quad (4.41)$$

¹¹⁸³ Expanding the terms involving ϵ yeilds:

$$\frac{1}{\Gamma(1+\epsilon)} = 1 + \gamma_E \epsilon + \mathcal{O}(\epsilon^2), \quad (4.42a)$$

$$\Gamma(1-\epsilon) = 1 + \gamma_E \epsilon + \mathcal{O}(\epsilon^2), \quad (4.42b)$$

$$\left(\frac{x}{y} \right)^\epsilon = 1 + \epsilon \ln \left(\frac{x}{y} \right) + \mathcal{O}(\epsilon^2). \quad (4.42c)$$

¹¹⁸⁴ And so the finite terms are:

$$= \frac{g_s^2 C_A \Delta_{i-1,i+1}}{4^{1+\epsilon} \pi^{2+\epsilon}} \left((1 + \gamma_E \epsilon + \mathcal{O}(\epsilon^2)) \left(\frac{1}{\epsilon} + \ln \left(\frac{\lambda^2}{\mu^2} \right) + \mathcal{O}(\epsilon) \right) - (1 + \gamma_E \epsilon + \mathcal{O}(\epsilon^2)) \left(\frac{1}{\epsilon} + \ln \left(\frac{q_{ti\perp}^2}{\mu^2} \right) + \mathcal{O}(\epsilon) \right) \right) \quad (4.43a)$$

$$= \frac{g_s^2 C_A \Delta_{i-1,i+1}}{4\pi^2} \ln \left(\frac{\lambda^2}{q_{ti\perp}^2} \right) \quad (4.43b)$$

$$= \frac{\alpha_s C_A \Delta_{i-1,i+1}}{\pi} \ln \left(\frac{\lambda^2}{q_{ti\perp}^2} \right) \quad (4.43c)$$

¹¹⁸⁵ Likewise for the emission purely from the backward quark line we have:

$$= \frac{\alpha_s C_A \Delta_{i-1,i+1}}{\pi} \ln \left(\frac{\lambda^2}{q_{bi\perp}^2} \right) \quad (4.44)$$

¹¹⁸⁶ For the interference we expand the exponential with both forward emission q momenta

¹¹⁸⁷ and backward emission q momenta to get:

$$= \frac{g_s^2 C_A \Delta_{i-1,i+1}}{4^{1+\epsilon} \pi^{2+\epsilon}} \left(\left(\frac{1}{\epsilon} + \gamma_E + \ln \left(\frac{\lambda^2}{\mu^2} \right) + \mathcal{O}(\epsilon) \right) - \frac{1}{2} \left[\frac{2}{\epsilon} + 2\gamma_E + \ln \left(\frac{q_{ti\perp}^2}{\mu^2} \right) - \ln \left(\frac{q_{bi\perp}^2}{\mu^2} \right) + \mathcal{O}(\epsilon) \right] \right) \quad (4.45a)$$

$$= \frac{\alpha_s C_A \Delta_{i-1,i+1}}{\pi} \ln \left(\frac{\lambda^2}{\sqrt{q_{ti\perp}^2 q_{bi\perp}^2}} \right) \quad (4.45b)$$

¹¹⁸⁸ This is a very similar form to that found in [?] and [?].

¹¹⁸⁹ **4.2.7 Example: $2 \rightarrow 4$ Scattering**

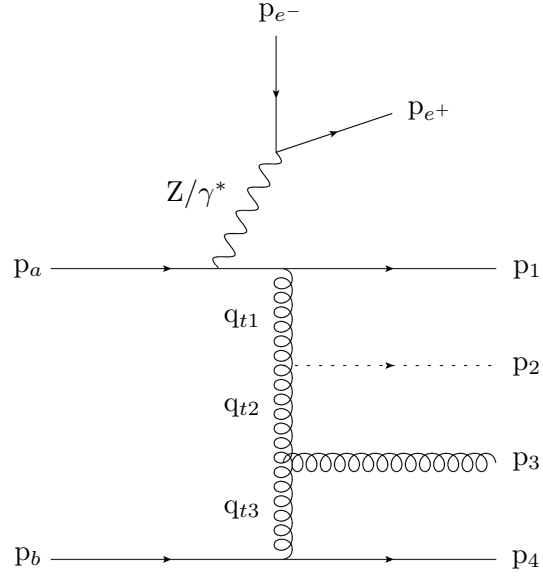
¹¹⁹⁰ As an example we show the cancellation explicitly for the case of $2 \rightarrow 4$ when the p_2
¹¹⁹¹ momentum has gone soft. A contributing soft diagram is shown in fig. 4.2a and one
¹¹⁹² example of a contributing virtual diagram of the same order is shown in fig. 4.2b. When
¹¹⁹³ p_2 goes soft we have the following form for the $2 \rightarrow 4$ integrated amplitude squared
¹¹⁹⁴ (N.B.: The integration is only schematic and doesn't represent the full Lorentz invariant
¹¹⁹⁵ phase space):

$$\int |\mathcal{A}_{soft}^{2 \rightarrow 4}|^2 = \frac{4C_A g_s^2 \Delta_{1,3}}{(2\pi)^{2+2\epsilon} 4\pi \epsilon \Gamma(\epsilon+1)} \left(\frac{\lambda^2}{\mu^2} \right)^\epsilon \left[|\mathcal{K}_a j_1^Z \cdot j_2|^2 \frac{V^2(q_{t1}, q_{t3})}{q_{t1}^2 q_{t3}^2} + |\mathcal{K}_b j_1 \cdot j_2^Z|^2 \frac{V^2(q_{b1}, q_{b3})}{q_{b1}^2 q_{b3}^2} + \dots \right. \\ \left. 2\Re \left\{ \mathcal{K}_a \overline{\mathcal{K}_b} (j_1^Z \cdot j_2) \overline{(j_1 \cdot j_2^Z)} \right\} \frac{V(q_{t1}, q_{t3}) \cdot V(q_{b1}, q_{b3})}{q_{t1} q_{t3} q_{b1} q_{b3}} \right], \quad (4.46)$$

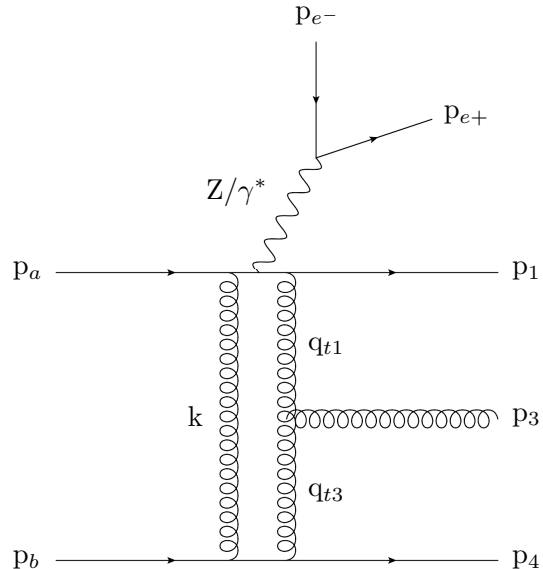
¹¹⁹⁶ and the virtual contributions for the $2 \rightarrow 3$ amplitude is:

$$\int |\mathcal{A}_{virtual}^{2 \rightarrow 3}|^2 = |\mathcal{K}_b j_1 \cdot j_2^Z|^2 \frac{V^2(q_{t1}, q_{t3})}{q_{t1}^2} e^{2\hat{\alpha}(q_{t1})\Delta_{1,3}} + |\mathcal{K}_t j_1^Z \cdot j_2|^2 \frac{V^2(q_{b1}, q_{b3})}{q_{b1}^2} e^{2\hat{\alpha}(q_{b1})\Delta_{1,3}} + \dots \\ 2\Re \left\{ \mathcal{K}_a \overline{\mathcal{K}_b} (j_1^Z \cdot j_2) \overline{(j_1 \cdot j_2^Z)} \right\} \frac{V(q_{t1}, q_{t3}) \cdot V(q_{b1}, q_{b3})}{q_{t1} q_{t3} q_{b1} q_{b3}} e^{(\hat{\alpha}(q_{t1}) + \hat{\alpha}(q_{b1}))\Delta_{1,3}}. \quad (4.47)$$

¹¹⁹⁷ Once we expand the exponential to the correct order in g_s^2 , the sum of these matrix
¹¹⁹⁸ elements squared over the region of phase space when p_2 is soft is:



(a) Soft Emission



(b) Virtual Emission

Figure 4.2: Examples of diagrams contributing to $2 \rightarrow 4$ scattering. In fig. 4.2a the p_2 has been drawn with a dashed line to denote it is not resolvable. In fig. 4.2b the final state momenta have been labelled in a seemingly strange way - this was done to make clear the cancellation when working through the algebra.

$$\begin{aligned}
 \int (|\mathcal{A}_{soft}^{2 \rightarrow 4}|^2 + |\mathcal{A}_{virtual}^{2 \rightarrow 3}|^2) = & |\mathcal{K}_a j_1^Z \cdot j_2|^2 \frac{V^2(q_{t1}, q_{t3})}{q_{t1}^2} \left(\frac{4C_A g_s^2 \Delta_{1,3}}{(2\pi)^{2+2\epsilon} 4\pi} \frac{\pi^{\epsilon+1}}{\epsilon \Gamma(\epsilon+1)} - 2\hat{\alpha}(q_{t1}) \Delta_{1,3} \right) + \dots \\
 & |\mathcal{K}_b j_1 \cdot j_2^Z|^2 \frac{V^2(q_{b1}, q_{b3})}{q_{b1}^2} \left(\frac{4C_A g_s^2 \Delta_{1,3}}{(2\pi)^{2+2\epsilon} 4\pi} \frac{\pi^{\epsilon+1}}{\epsilon \Gamma(\epsilon+1)} - 2\hat{\alpha}(q_{b1}) \Delta_{1,3} \right) + \dots \\
 & 2\Re \left\{ \mathcal{K}_a \overline{\mathcal{K}_b} (j_1^Z \cdot j_2) \overline{(j_1 \cdot j_2^Z)} \right\} \frac{V(q_{t1}, q_{t3}) \cdot V(q_{b1}, q_{b3})}{q_{t1} q_{t3} q_{b1} q_{b3}} \left(\frac{4C_A g_s^2 \Delta_{1,3}}{(2\pi)^{2+2\epsilon} 4\pi} \frac{\pi^{\epsilon+1}}{\epsilon \Gamma(\epsilon+1)} - (\hat{\alpha}(q_{t1}) + \hat{\alpha}(q_{b1})) \Delta_{1,3} \right) + \dots
 \end{aligned} \tag{4.48}$$

1199 These bracketed terms are exactly the cancellations calculated in section 4 above.
1200 Therefore:

$$\begin{aligned} \int (|\mathcal{A}_{\text{soft}}^{2 \rightarrow 4}|^2 + |\mathcal{A}_{\text{virtual}}^{2 \rightarrow 3}|^2) = & \frac{\alpha_s C_A \Delta_{1,3}}{\pi} \left(|\mathcal{K}_a j_1^Z \cdot j_2|^2 \frac{V^2(q_{t1}, q_{t3})}{q_{t1}^2} \ln \left(\frac{\lambda^2}{|q_{1t\perp}|^2} \right) + \dots \right. \\ & |\mathcal{K}_b j_1 \cdot j_2^Z|^2 \frac{V^2(q_{b1}, q_{b3})}{q_{b1}^2} \ln \left(\frac{\lambda^2}{|q_{1b\perp}|^2} \right) + \dots \\ & \left. 2 \Re \left\{ \mathcal{K}_a \overline{\mathcal{K}_b} (j_1^Z \cdot j_2) \overline{(j_1 \cdot j_2^Z)} \right\} \frac{V(q_{t1}, q_{t3}) \cdot V(q_{b1}, q_{b3})}{q_{t1} q_{t3} q_{b1} q_{b3}} \ln \left(\frac{\lambda^2}{\sqrt{|q_{1t\perp}|^2 |q_{1b\perp}|^2}} \right) \right) + \mathcal{O}(\alpha_s^2), \end{aligned} \quad (4.49)$$

1201 Which is manifestly finite.

1202 4.3 Subtractions and the λ_{cut} scale

1203 The table below shows the value of the total cross section for varying values of the
1204 parameter λ_{cut} defined in section ???. It is clear that the cross section does not display
1205 a large dependence on the value of λ_{cut} . Figure 4.3 shows the effect of the same variation
1206 in λ_{cut} on the differential distribution in the rapidity gap between the two leading jets
1207 in p_\perp . Our default chosen value is 0.2.

λ_{cut} (GeV)	$\sigma(2j)$ (pb)	$\sigma(3j)$ (pb)	$\sigma(4j)$ (pb)
0.2	5.16 ± 0.03	0.90 ± 0.02	0.20 ± 0.02
0.5	5.17 ± 0.02	0.92 ± 0.01	0.22 ± 0.03
1.0	5.20 ± 0.02	0.91 ± 0.02	0.20 ± 0.01
1.0	5.26 ± 0.02	0.91 ± 0.02	0.21 ± 0.02

Table 4.1: The total cross-sections for the 2, 3 and 4 jet exclusive rates with associated statistical errors shown for different values of the regularisation parameter λ_{cut} . The scale choice was the half the sum over all traverse scales in the event, $H_T/2$.

1208 4.4 $Z/\gamma^* + \text{Jets}$ at the ATLAS Experiment

1209 • Re-word descriptions of plots

1210 We now compare the results of the formalism described in the previous sections to data.
1211 We begin with a recent ATLAS analysis of Z -plus-jets events from 7 TeV collisions [3].

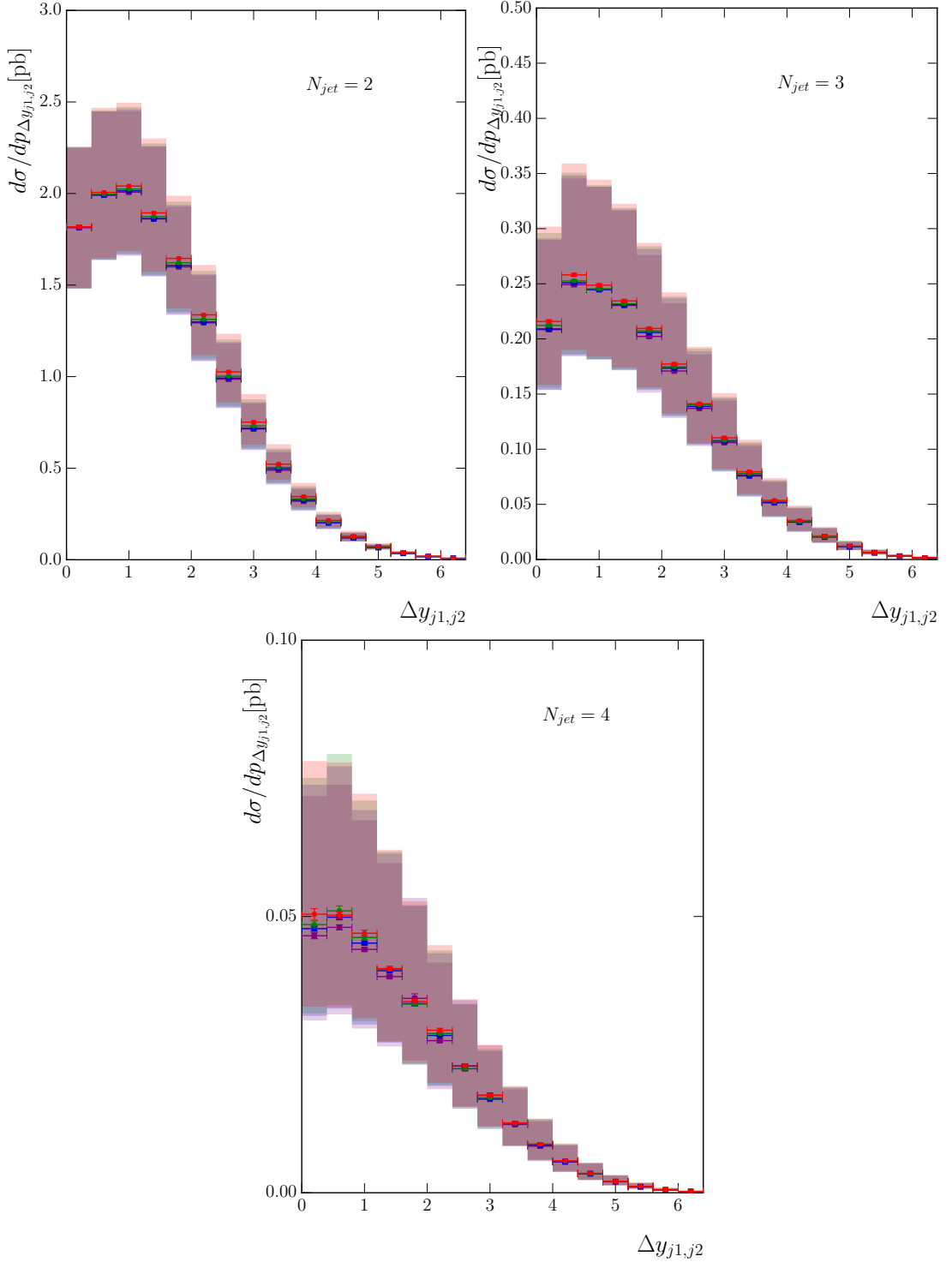


Figure 4.3: The effect of varying λ_{cut} on the differential distribution in the rapidity gap between the two leading jets in p_\perp with the $N_{jet} = 2, 3, 4$ exclusive selections shown from left to right. $\lambda_{cut} = 0.2$ (red), 0.5 (blue), 1.0 (green), 2.0 (purple).

1212 We summarise the cuts in the following table:

Lepton Cuts	$p_{T\ell} > 20 \text{ GeV}, \eta_\ell < 2.5$ $\Delta R^{\ell^+\ell^-} > 0.2, 66 \text{ GeV} \leq m^{\ell^+\ell^-} \leq 116 \text{ GeV}$
Jet Cuts ($\text{anti-}k_T, 0.4$)	$p_{Tj} > 30 \text{ GeV}, y_j < 4.4$ $\Delta R^{j\ell} > 0.5$

Table 4.2: Cuts applied to theory simulations in the ATLAS Z -plus-jets analysis results shown in Figs. 4.4–4.7.

1213 Any jet which failed the final isolation cut was removed from the event, but the event
 1214 itself is kept provided there are a sufficient number of other jets present. Throughout
 1215 the central value of the HEJ predictions has been calculated with factorisation and
 1216 renormalisation scales set to $\mu_F = \mu_R = H_T/2$, and the theoretical uncertainty band
 1217 has been determined by varying these independently by up to a factor of 2 in each
 1218 direction (removing the corners where the relative ratio is greater than two). Also
 1219 shown in the plots taken from the ATLAS paper are theory predictions from Alpgen [56],
 1220 Sherpa [42, 45], MC@NLO [39] and BlackHat+Sherpa [19, 47]. We will also comment
 1221 on the recent theory description of Ref. [36].

1222 In Fig. 4.4, we begin this set of comparisons with predictions and measurements of the
 1223 inclusive jet rates. HEJ and most of the other theory descriptions give a reasonable
 1224 description of these rates. The MC@NLO prediction drops below the data because
 1225 it only contains the hard-scattering matrix element for Z/γ^* production and relies
 1226 on a parton shower for additional emissions. The HEJ predictions have a larger
 1227 uncertainty band which largely arises from the use of leading-order results in the
 1228 matching procedures.

1229 The first differential distribution we consider here is the distribution of the invariant
 1230 mass between the two hardest jets, Fig. 4.5. The region of large invariant mass is
 1231 particularly important because this is a critical region for studies of vector boson fusion
 1232 (VBF) processes in Higgs-plus-dijets. Radiation patterns are largely universal between
 1233 these processes, so one can test the quality of theoretical descriptions in Z/γ^* -plus-
 1234 dijets and use these to inform the VBF analyses. It is also a distribution which will be
 1235 studied to try to detect subtle signs of new physics. In this study, HEJ and the other
 1236 theory descriptions all give a good description of this variable out to 1 TeV, with HEJ
 1237 being closest throughout the range. The merged sample of Ref. [36] (Fig. 9 in that
 1238 paper) combined with the Pythia8 parton shower performs reasonably well throughout
 1239 the range with a few deviations of more than 20%, while that combined with Herwig++
 1240 deviates badly. In a recent ATLAS analysis of W -plus-dijet events [6], the equivalent
 1241 distribution was extended out to 2 TeV and almost all of the theoretical predictions

1242 deviated significantly while the HEJ prediction remained flat. This is one region where
1243 the high-energy logarithms which are only included in HEJ are expected to become
1244 large.

1245 In Fig. 4.6, we show the comparison of various theoretical predictions to the distribution
1246 of the absolute rapidity difference between the two leading jets. It is clear in the left
1247 plot that HEJ gives an excellent description of this distribution. This is to some extent
1248 expected as high-energy logarithms are associated with rapidity separations. However,
1249 this variable is only the rapidity separation between the two hardest jets which is often
1250 not representative of the event as harder jets tend to be more central. Nonetheless, the
1251 HEJ description performs well in this restricted scenario. The next-to-leading order
1252 (NLO) calculation of Blackhat+Sherpa also describes the distribution quite well while
1253 the other merged, fixed-order samples deviate from the data at larger values. The
1254 merged samples of Ref. [36] (Fig. 8 in that paper) describe this distribution well for
1255 small values of this variable up to about 3 units when combined with Herwig++ and
1256 for most of the range when combined with the Pythia8 parton shower, only deviating
1257 above 5 units.

1258 The final distribution in this section is that of the ratio of the transverse momentum of
1259 the second hardest jet to the hardest jet. The perturbative description of HEJ does not
1260 contain any systematic evolution of transverse momentum and this can be seen where
1261 its prediction undershoots the data at low values of p_{T2}/p_{T1} . However, for values of
1262 $p_{T2} \gtrsim 0.5p_{T1}$, the ratio of the HEJ prediction to data is extremely close to 1. The
1263 fixed-order based predictions shown in Fig. 4.4 are all fairly flat above about 0.2, but
1264 the ratio of the data differs by about 10%.

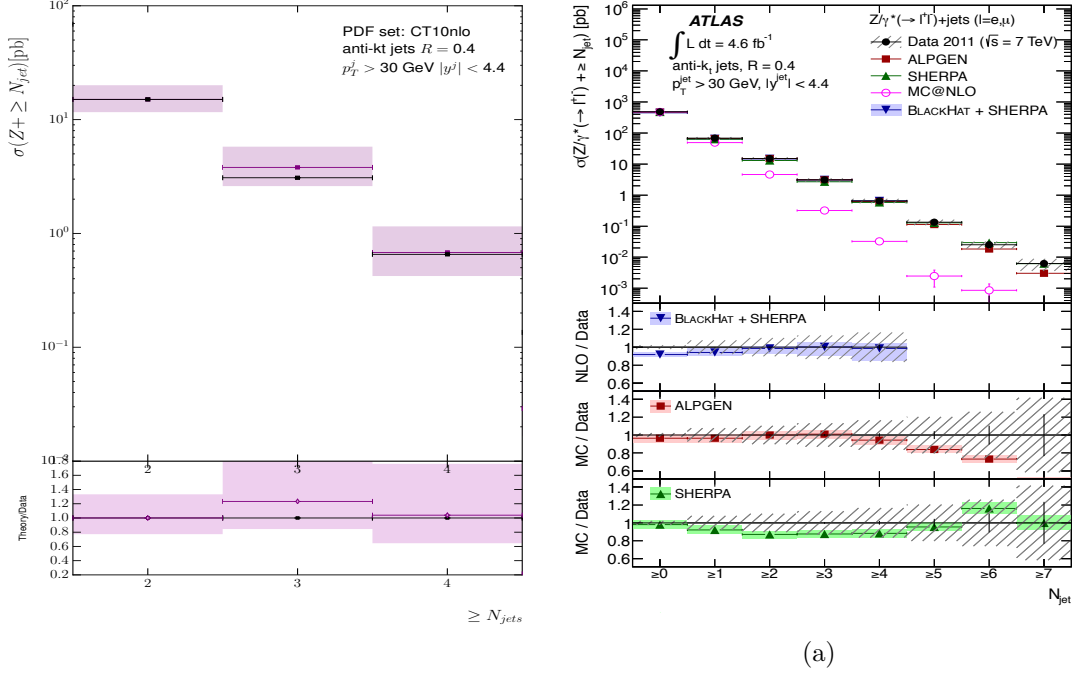


Figure 4.4: These plots show the inclusive jet rates from (a) HEJ and (b) other theory descriptions and data [3]. HEJ events all contain at least two jets and do not contain matching for 5 jets and above, so these bins are not shown.

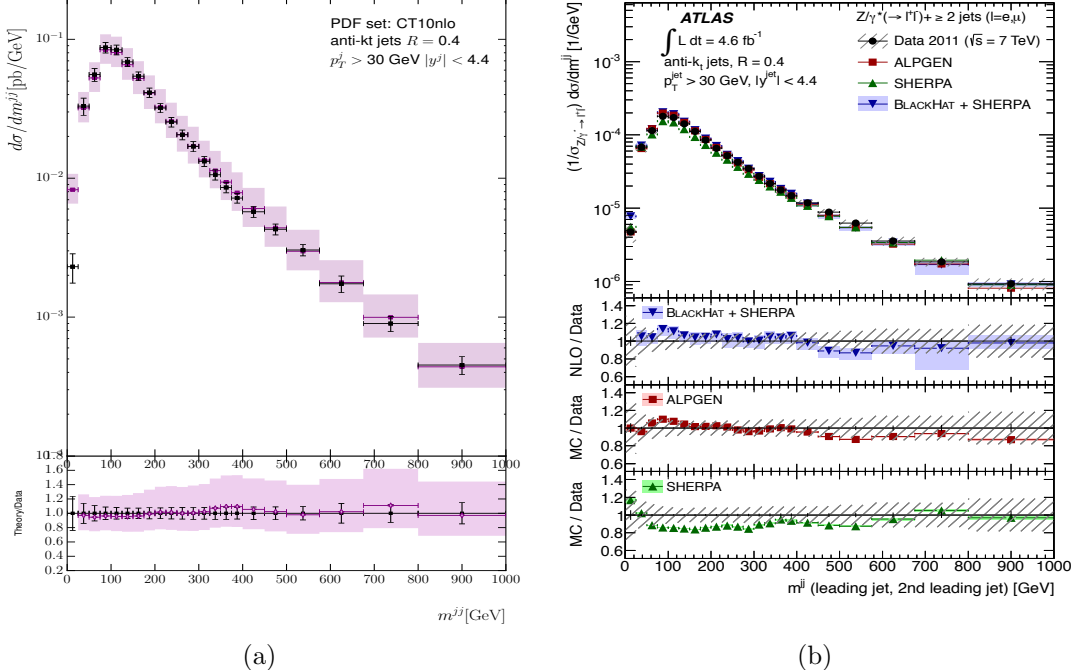


Figure 4.5: These plots show the invariant mass between the leading and second-leading jet in p_T . As in Fig. 4.4, predictions are shown from (a) HEJ and (b) other theory descriptions and data [3]. These studies will inform Higgs plus dijets analyses, where cuts are usually applied to select events with large m_{12} .

1265 **4.4.1 CMS - $Z + \text{Jets}$ Measurements**

1266 We now compare to data from a CMS analysis of events with a Z/γ^* boson
1267 produced in association with jets [51]. We show, for comparison, the plots from that
1268 analysis which contain theoretical predictions from Sherpa [42, 45], Powheg [10] and
1269 MadGraph [12]. The cuts used for this analysis are summarised in tab. 4.3.

Lepton Cuts	$p_{T\ell} > 20 \text{ GeV}, \eta_\ell < 2.4$ $71 \text{ GeV} \leq m^{\ell^+\ell^-} \leq 111 \text{ GeV}$
Jet Cuts (anti- k_T , 0.5)	$p_{Tj} > 30 \text{ GeV}, y_j < 2.4$ $\Delta R^{j\ell} > 0.5$

Table 4.3: Cuts applied to theory simulations in the CMS Z -plus-jets analysis results shown in Figs. 4.8–4.10

1270 As in the previous section, any jet which failed the final isolation cut was removed from
1271 the event, but the event itself is kept provided there are a sufficient number of other jets
1272 present. The main difference to these cuts and those of ATLAS in the previous section
1273 is that the jets are required to be more central; $|\eta| < 2.4$ as opposed to $|y| < 4.4$. This
1274 allows less room for evolution in rapidity; however, HEJ predictions are still relevant
1275 in this scenario. Once again, the central values are given by $\mu_F = \mu_R = H_T/2$ with
1276 theoretical uncertainty bands determined by varying these independently by factors of
1277 two around this value. HEJ events always contain a minimum of two jets and therefore
1278 here we only compare to the distributions for an event sample with at least two jets or
1279 above.

1280 We begin in Fig. 4.8 by showing the inclusive jet rates for these cuts. The HEJ
1281 predictions give a good description, especially for the 2- and 3-jet inclusive rates in this
1282 narrower phase space. The uncertainty bands are larger for HEJ than for the Sherpa
1283 and Powheg predictions due to our LO matching prescription (those for Madgraph are
1284 not shown).

1285 In Figs. 4.9–4.10, we show the transverse momentum distributions for the second
1286 and third jet respectively (the leading jet distribution was not given for inclusive dijet
1287 events). Beginning with the second jet in Fig. 4.9, we see that the HEJ predictions
1288 overshoot the data at large transverse momentum. In this region, the non-FKL matched
1289 components of the HEJ description become more important and these are not controlled
1290 by the high-energy resummation. The HEJ predictions are broadly similar to Powheg’s
1291 Z -plus-one-jet NLO calculation matched with the Pythia parton shower. In contrast,
1292 Sherpa’s prediction significantly undershoots the data at large transverse momentum.
1293 Here the Madgraph prediction gives the best description of the data.

Fig. 4.10 shows the transverse momentum distribution of the third jet in this data sample. Here, the ratio of the HEJ prediction to data shows a linear increase with transverse momentum (until the last bin where all the theory predictions show the same dip). Both the Sherpa and Powheg predictions show similar deviations for this variable while the Madgraph prediction again performs very well.

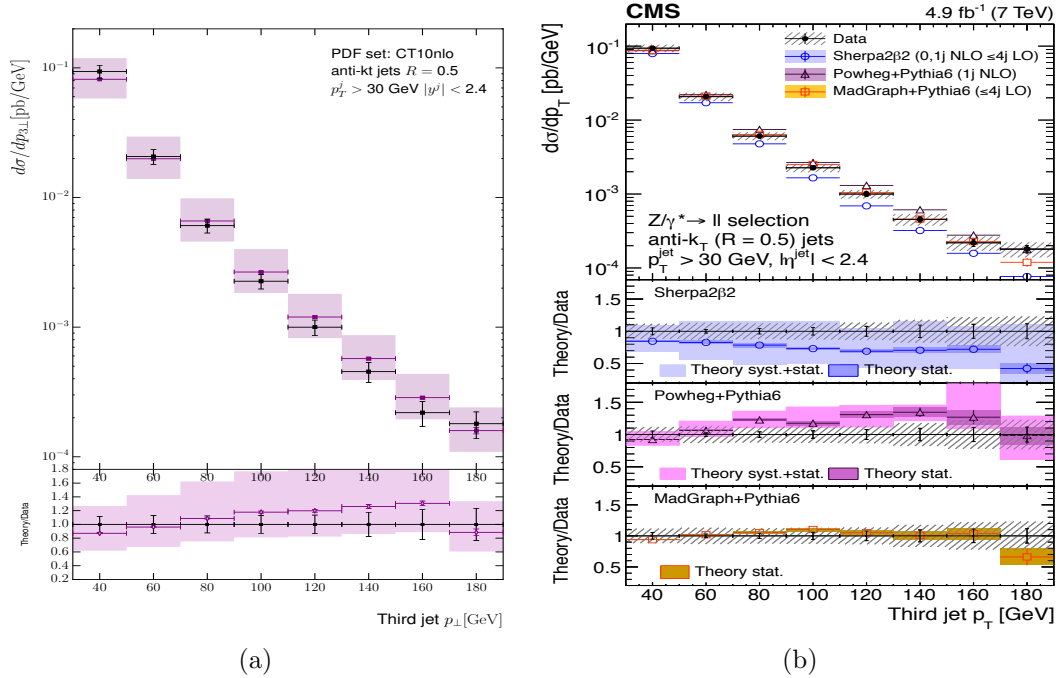


Figure 4.10: The transverse momentum distribution of the third hardest jet in inclusive dijet events in [51], compared to (a) the predictions from HEJ and (b) the predictions from other theory descriptions.

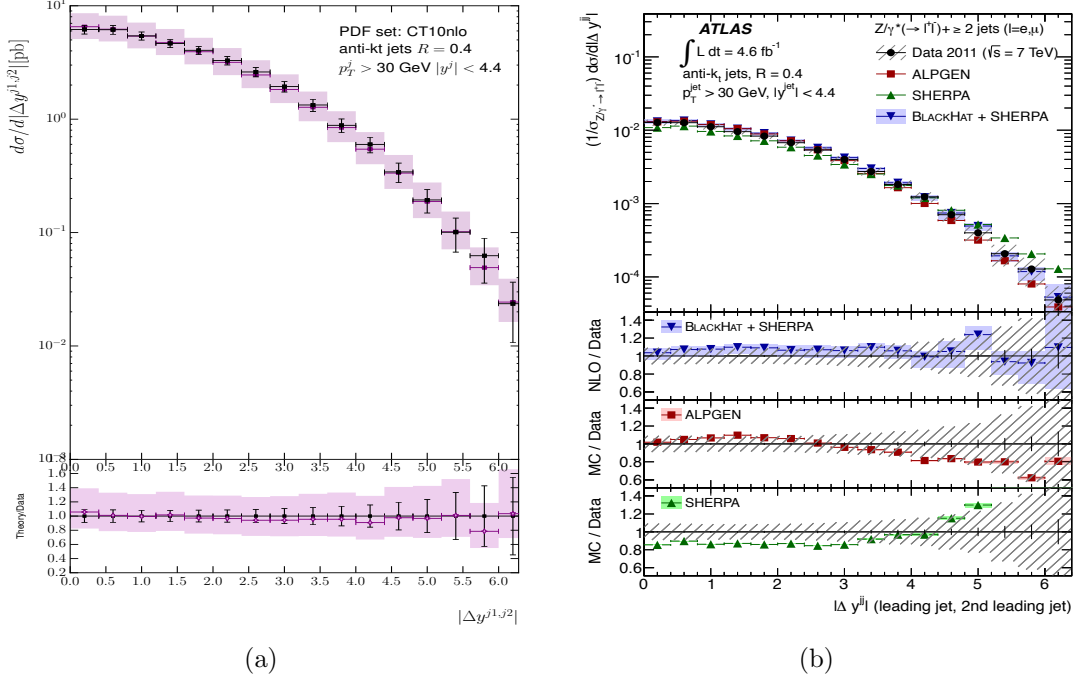


Figure 4.6: The comparison of (a) HEJ and (b) other theoretical descriptions and data [3] to the distribution of the absolute rapidity different between the two leading jets. HEJ and Blackhat+Sherpa give the best description.

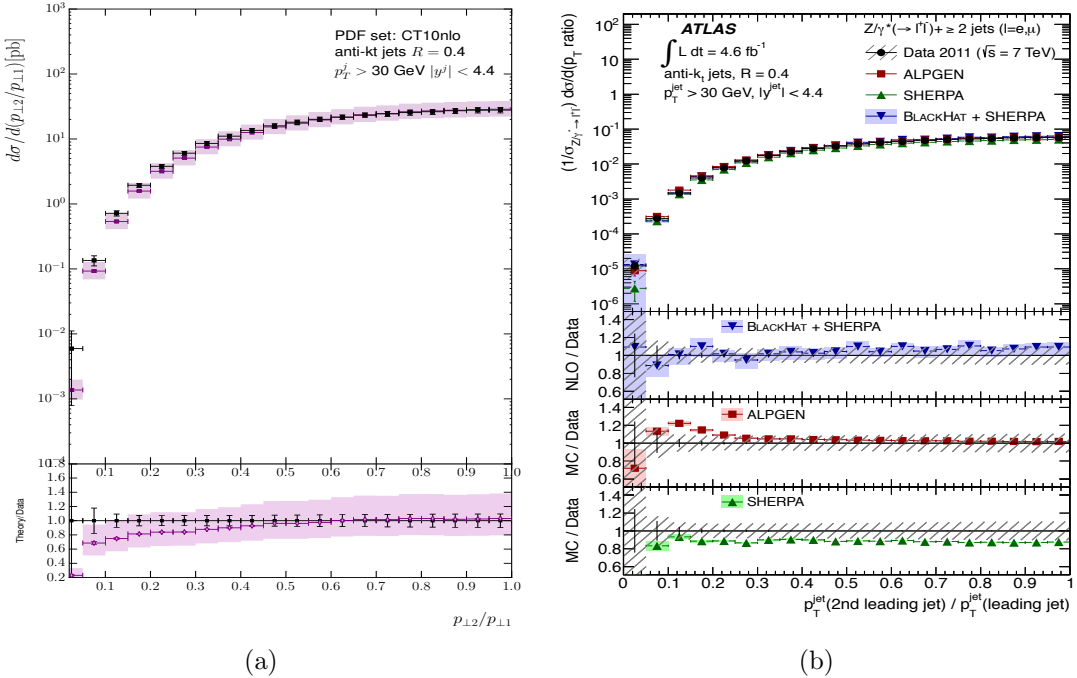


Figure 4.7: These plots show the differential cross section in the ratio of the leading and second leading jet in p_T from (a) HEJ and (b) other theory descriptions and data [3].

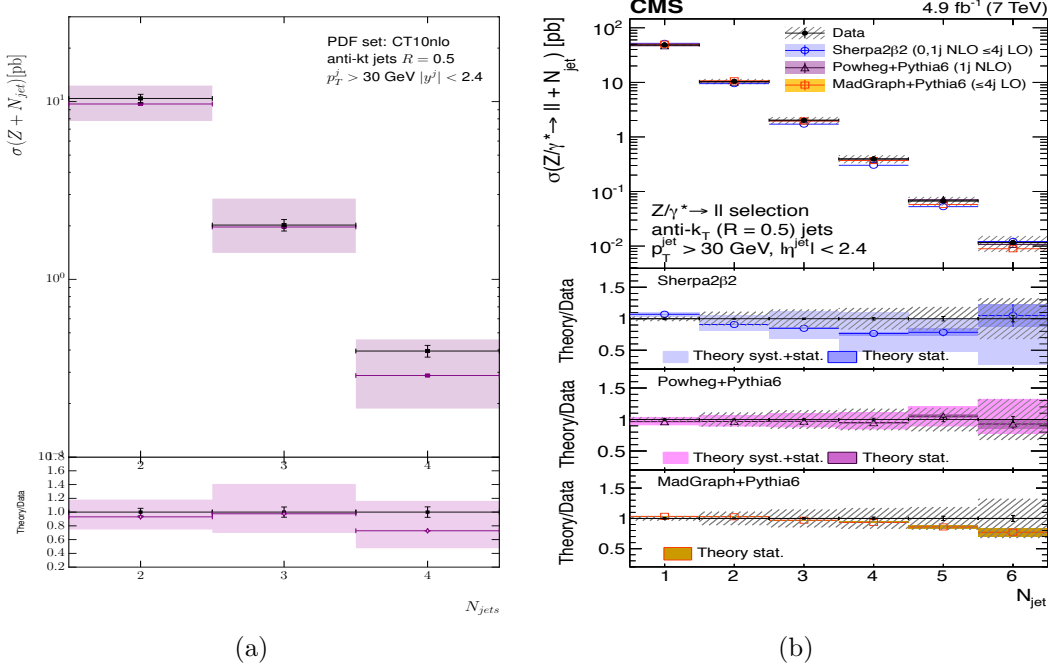


Figure 4.8: The inclusive jet rates as given by (a) the HEJ description and (b) by other theoretical descriptions, both plots compared to the CMS data in [51].

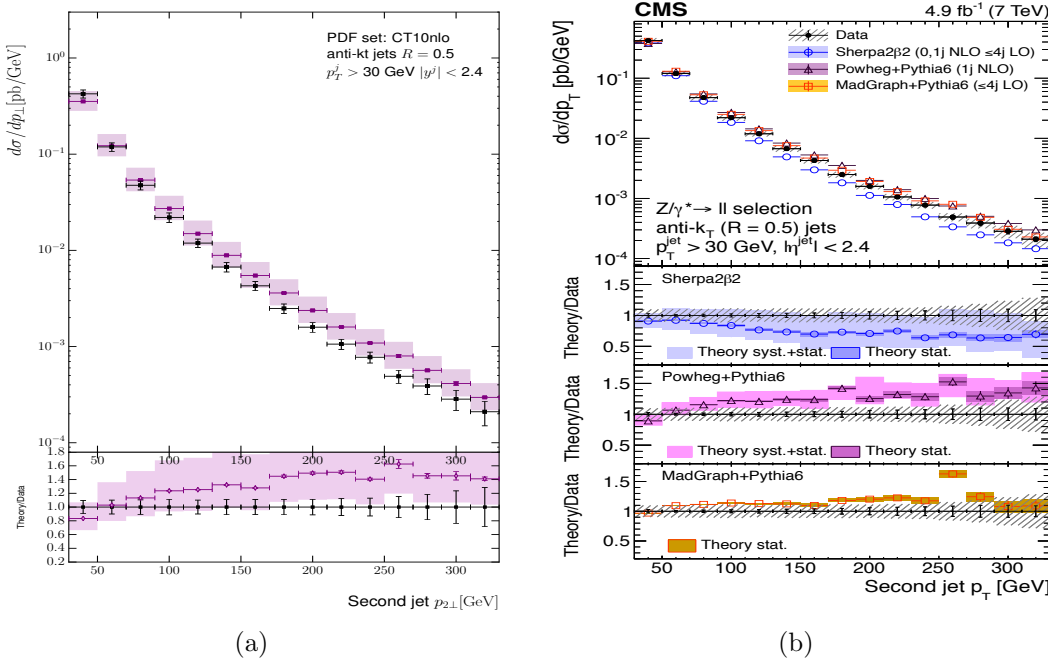


Figure 4.9: The transverse momentum distribution of the second hardest jet in inclusive dijet events in [51], compared to (a) the predictions from HEJ and (b) the predictions from other theory descriptions.

¹²⁹⁹ **Chapter 5**

¹³⁰⁰ **High Multiplicity Jets at ATLAS**

¹³⁰¹ Show the ATLAS pure jets analysis and talk a bit about the issues with running the
¹³⁰² damn thing. Talk about the conclusions about BFKL-like dynamics

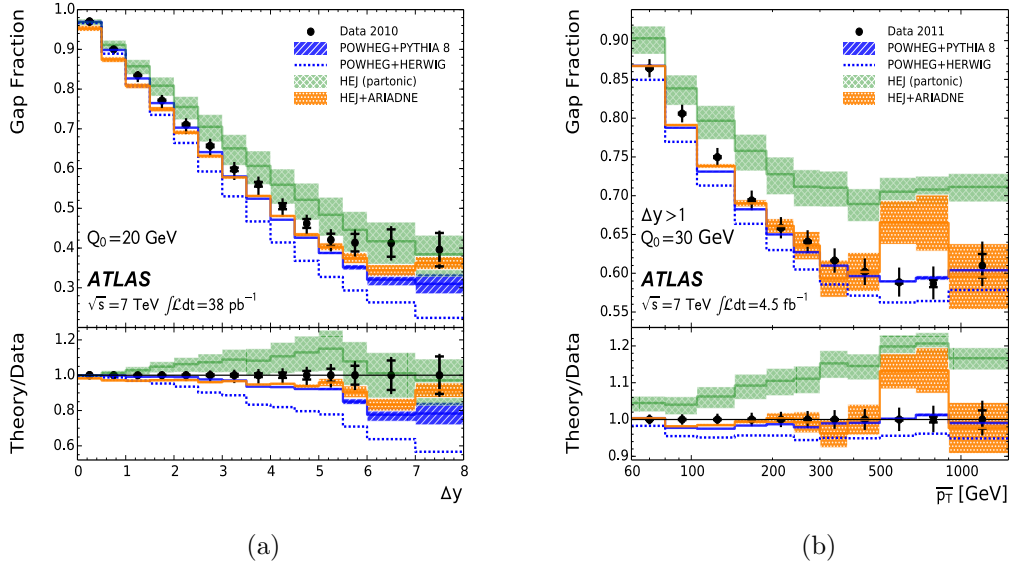


Figure 5.1

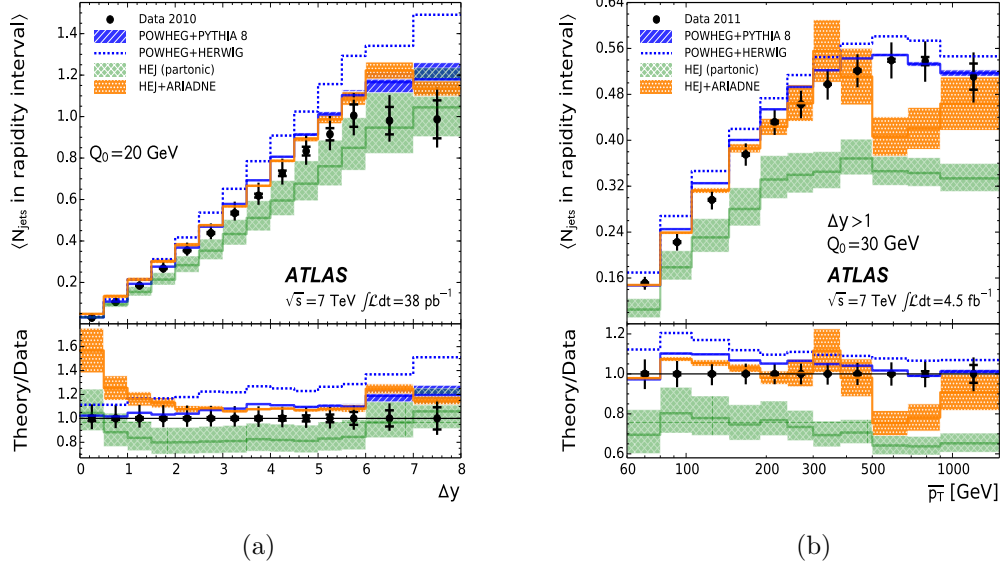


Figure 5.2

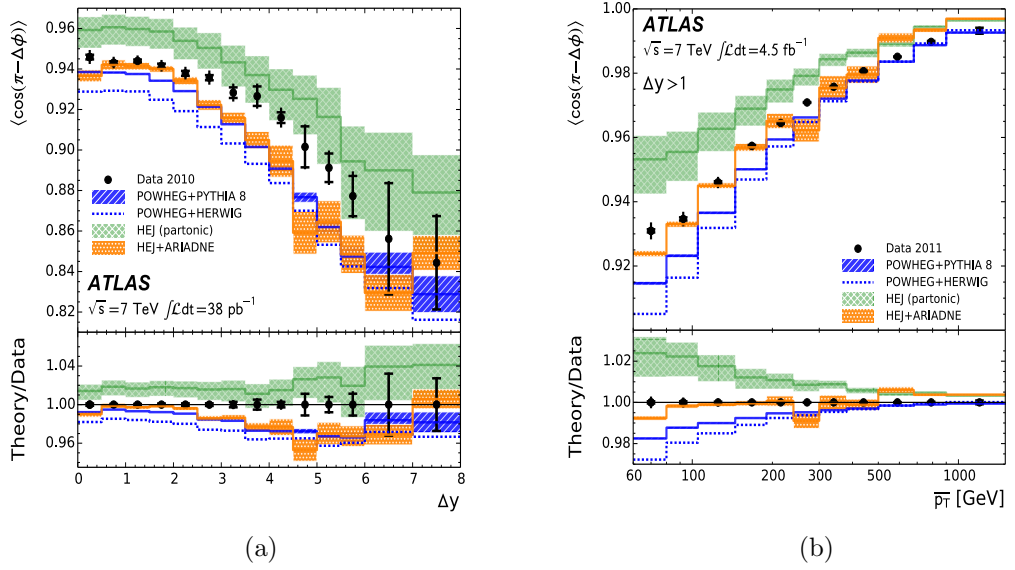


Figure 5.3

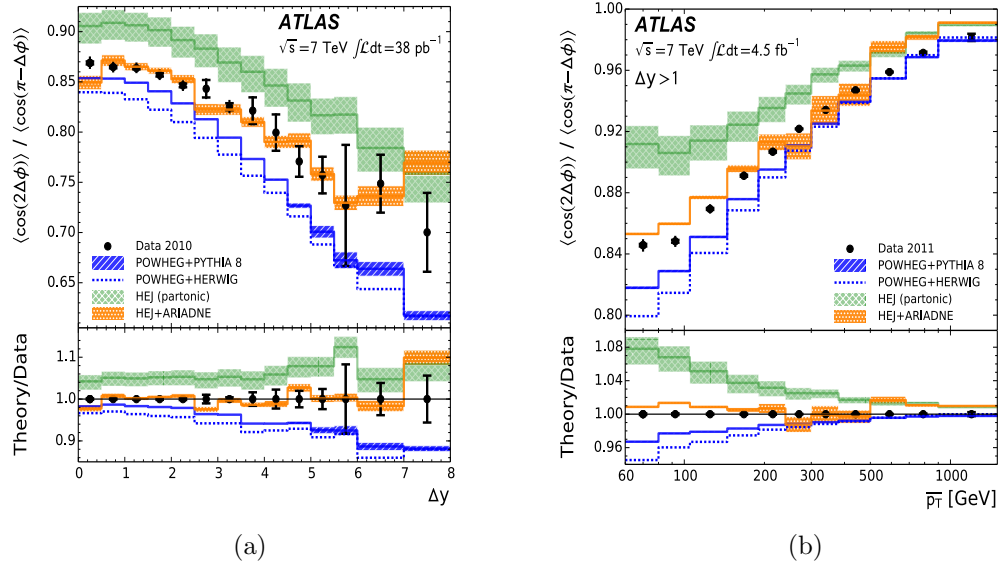


Figure 5.4

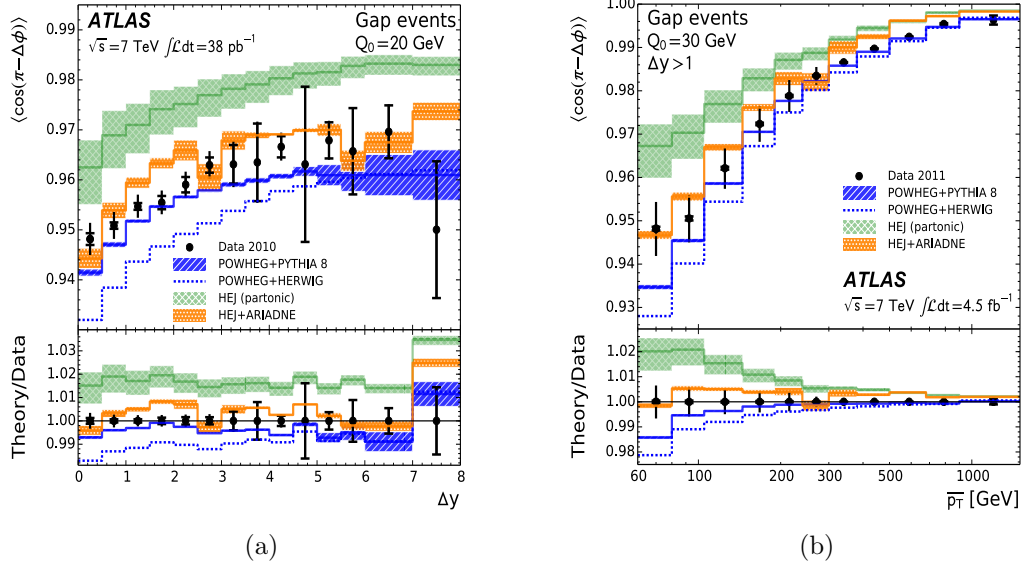


Figure 5.5

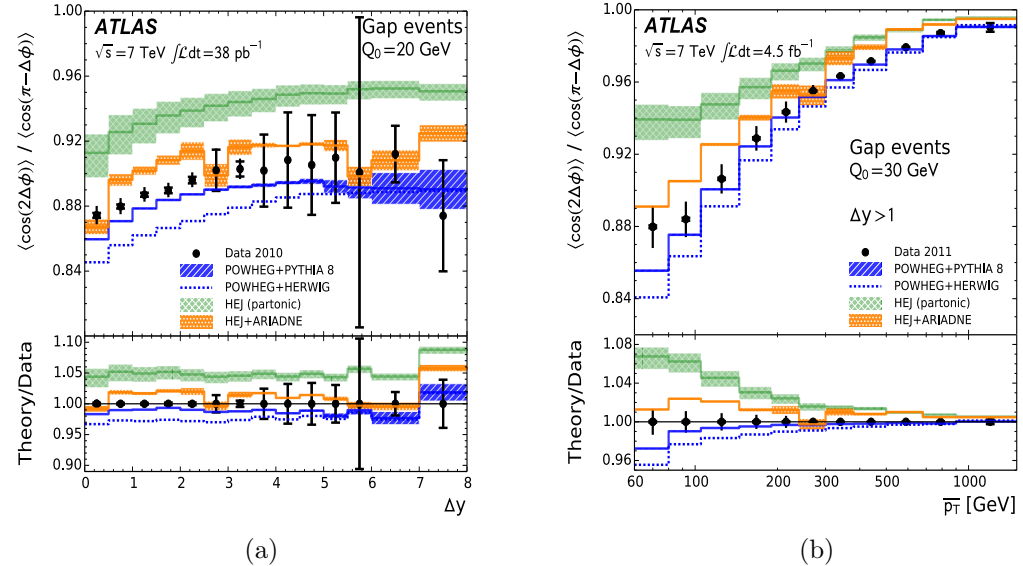


Figure 5.6

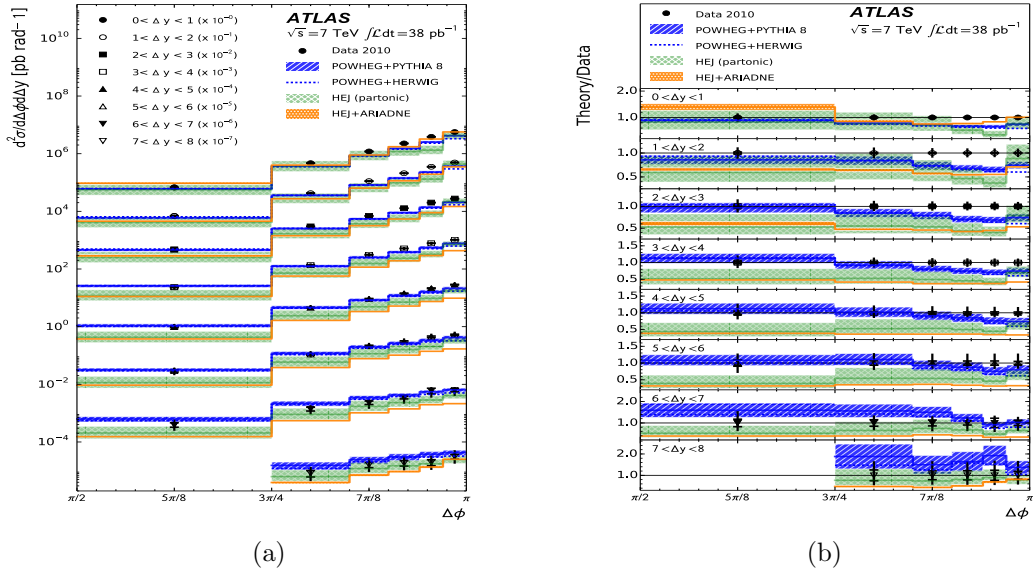


Figure 5.7

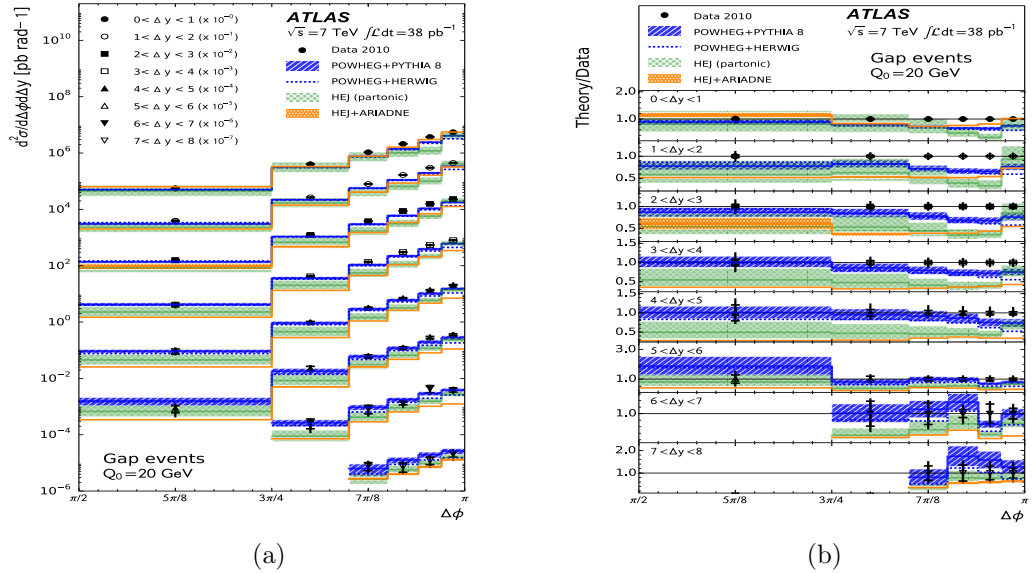


Figure 5.8

₁₃₀₃ **Chapter 6**

₁₃₀₄ **The W^\pm to Z/γ^* Ratio at ATLAS**

₁₃₀₅ Compare HEJ Z+Jets to NJet (NLO predictions) and MadGraph (LO predictions).

₁₃₀₆ ***Is this still worth it? Data/HEJ/MG all very unstable...***

¹³⁰⁷ Chapter 7

¹³⁰⁸ $Z/\gamma^* + \text{Jets}$ at 100TeV

- ¹³⁰⁹ • Talk about the FCC movement and the effect we expect the resummation will have at these energies.
- ¹³¹⁰ • Put all three lines (30GeV, 60GeV, 100GeV) on the same plots in this section?
- ¹³¹¹ • Pros: Can see that we can put more stringent cuts while maintaining x-section.
- ¹³¹² • Also makes the point that we can cut out all the NP physics we cant model.
- ¹³¹³ • Cons: Plots will be very busy.

¹³¹⁴ Figure (7.1) notes:

- ¹³¹⁵ • dphi plot
- ¹³¹⁶ • Start with this one because its the most boring,
- ¹³¹⁷ • i.e. if QCD didnt change with energy scale all plots would be like this one

¹³¹⁸ Figure (7.2) notes:

- ¹³¹⁹ • njets,
- ¹³²⁰ • Explicitly shows that the break-down of the perturbative series gets worse at higher energies,
- ¹³²¹ • The contributions from higher-order corrections increase as the energy increases,

¹³²² Figure (7.3) notes:

- ¹³²³ • dy plot,
- ¹³²⁴ • O(10) increase in cross-section as we go to large rapidities,

- 1327 • More energy in initial state means we can get more jets further in to the outer
1328 regions of y-space,
1329 • The increase seen is *exactly* the large logs we capture at play

1330 Figure (7.4) notes:

- 1331 • $dm_j j$ plot,
1332 • $O(10)$ increase in cross-section as we go to large invariant masses,
1333 • Invariant masses again correlate with the logs we resum (show this explicitly if
1334 you havent already),
1335 • Similar to figure (7.3)

1336 Figure (7.5a-7.5c) notes:

- 1337 • pT distributions,
1338 • Heavy tails...soooo?
1339 • More energy in initial state means we can get more jets further in to the outer
1340 regions of y-space,
1341 • What effect would a shower have on these distributions? Plenty of spare pT to
1342 radiate.

1343 Figure (7.6a-7.6c) notes:

- 1344 • Not much more to say about these - mostly covered in dy plots,

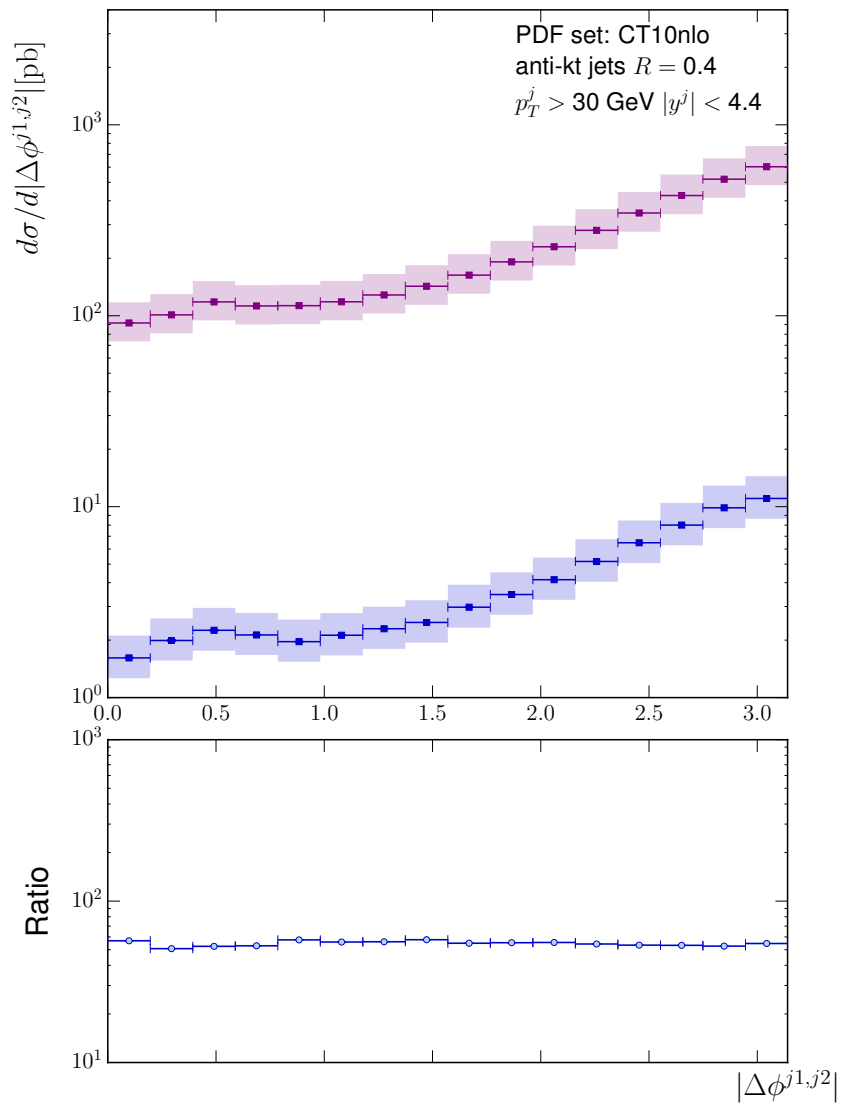


Figure 7.1: 12a

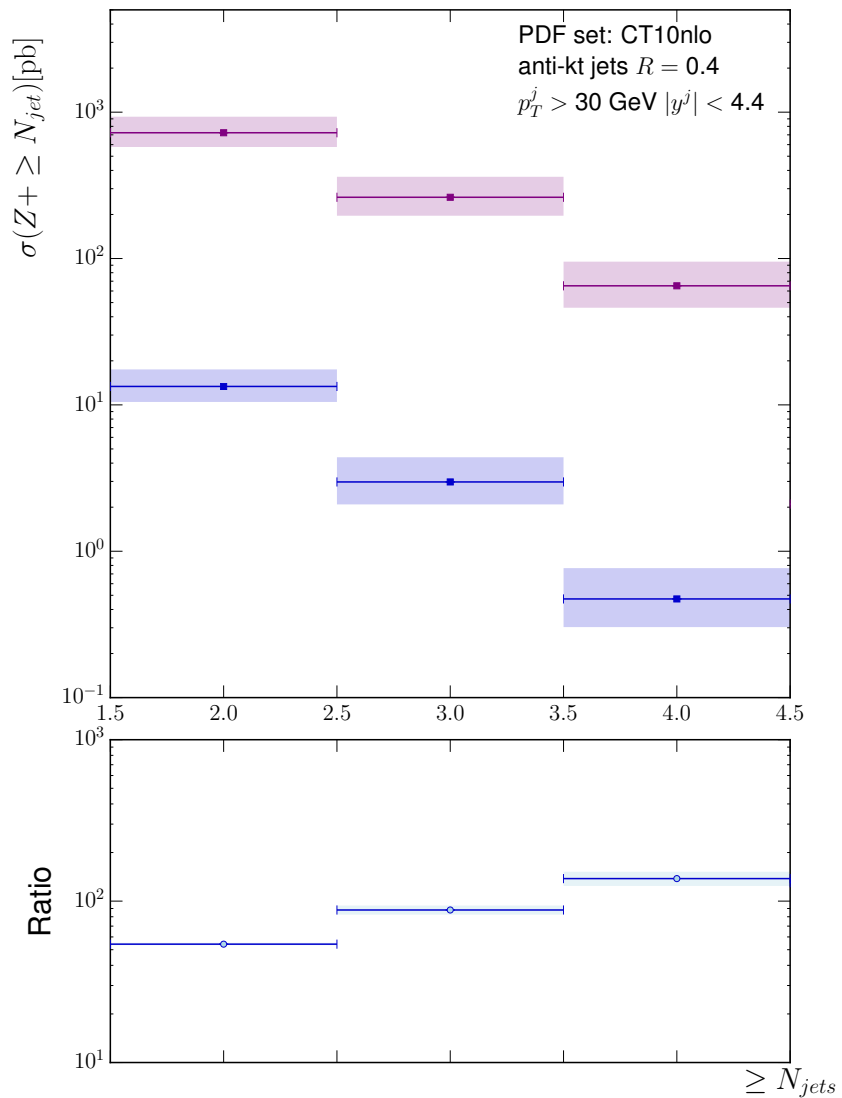


Figure 7.2: 12a

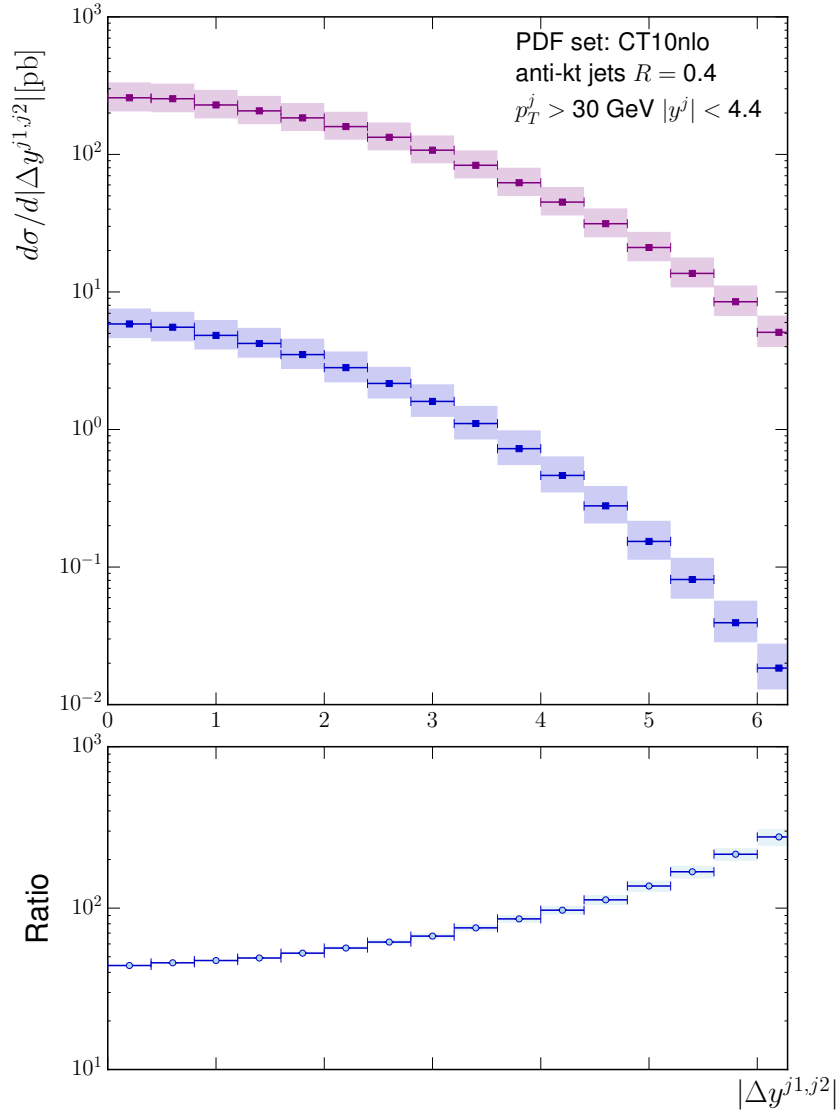


Figure 7.3: 11a

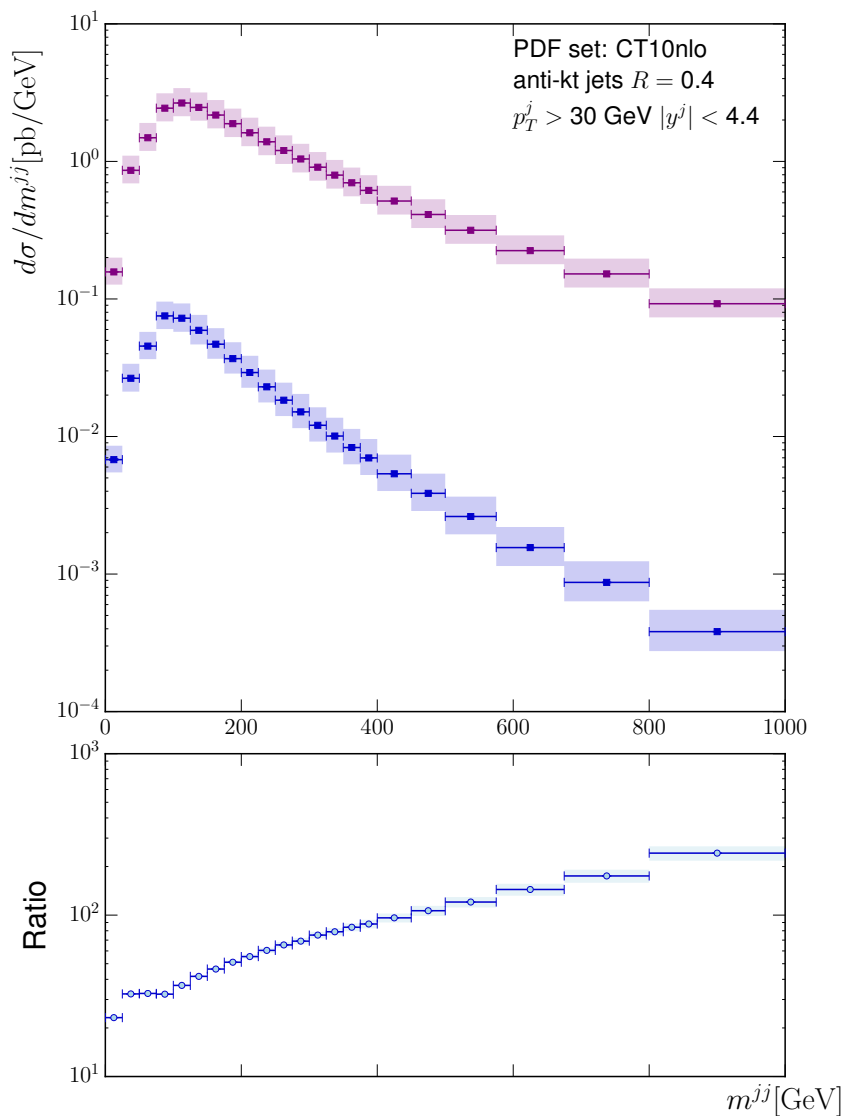
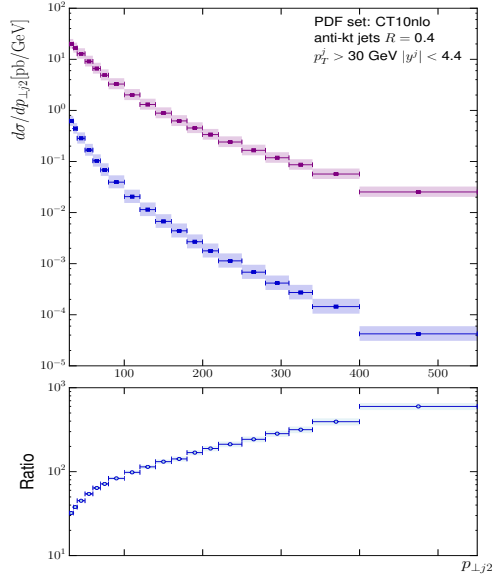
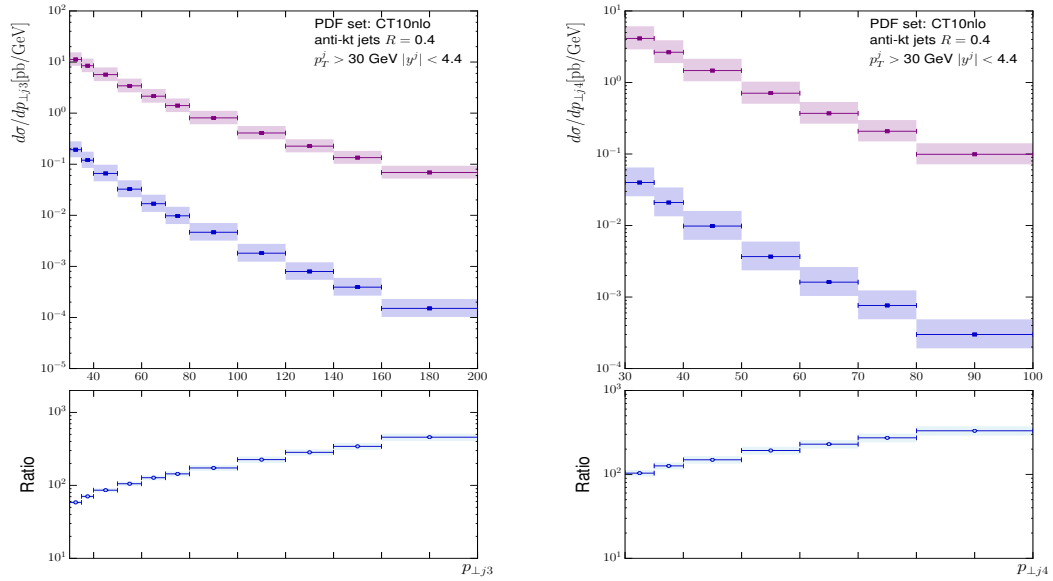


Figure 7.4: 11b



(a)



(b)

(c)

Figure 7.5

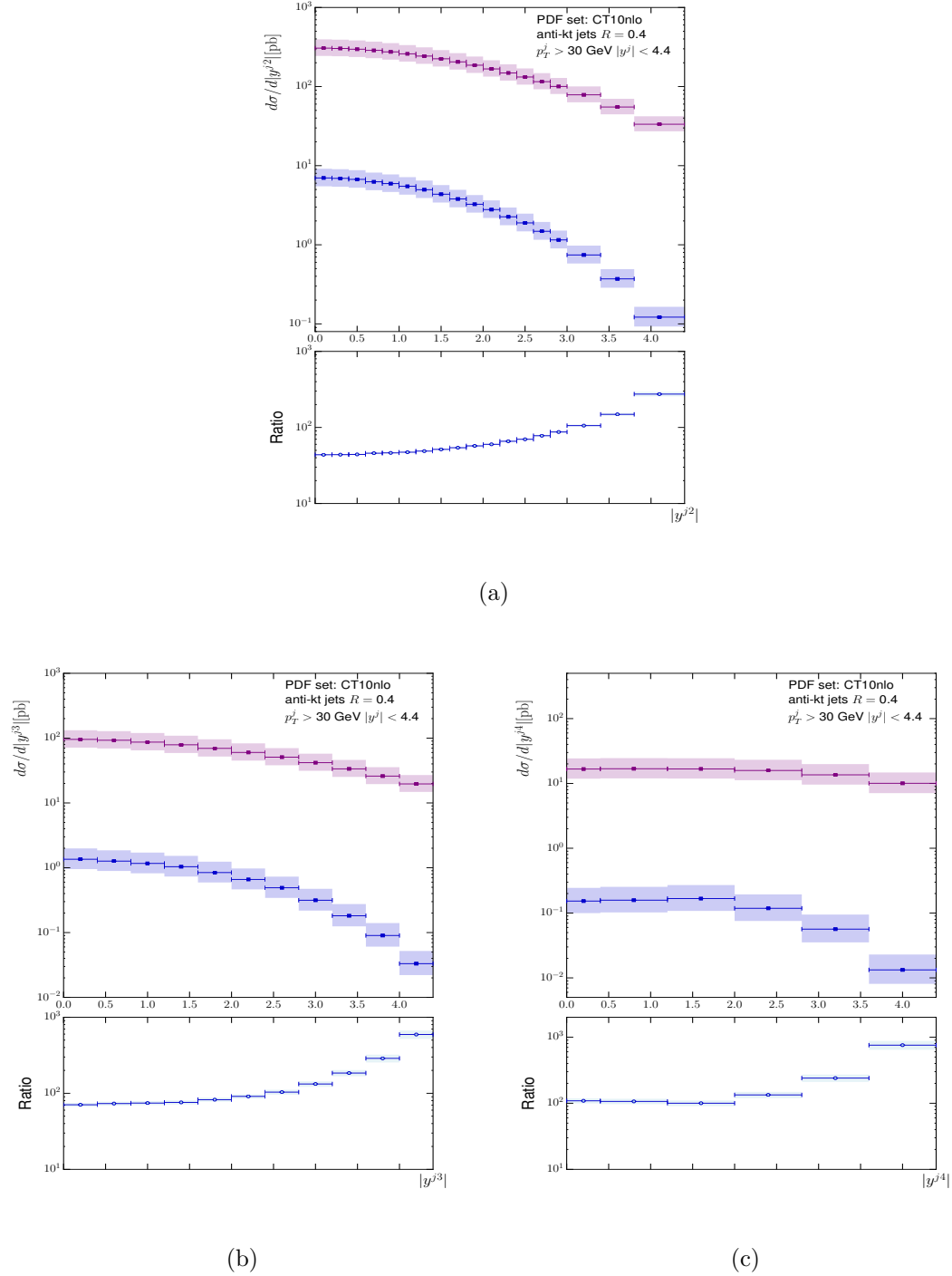


Figure 7.6

1345 Chapter 8

1346 Conclusions and Outlook

¹³⁴⁷ Appendix A

¹³⁴⁸ The Faddeev-Popov Trick

¹³⁴⁹ All that remains to be done is to evaluate the gluon propagator. As in QED when
¹³⁵⁰ trying to compute the propagator of a massless gauge boson we can use the work of
¹³⁵¹ Faddeev and Popov. The functional integral we want to evaluate is in the form:

$$\int DA e^{-\frac{i}{4} \int d^4x F_{\mu\nu}^a F^{a\mu\nu}}. \quad (\text{A.1})$$

¹³⁵² Where $DA = \prod_x \prod_{a,\mu} dA_\mu^a$. As briefly outlined above we would like to perform a
¹³⁵³ functional integration over all possible gauge choices and then pick out the subset of
¹³⁵⁴ gauges we are interested in by enforcing the gauge condition $G(A) = 0$ to eliminate
¹³⁵⁵ over-counting. This constraint may be written as [?]:

$$\int D\alpha(x) \delta(G(A^\alpha)) \text{Det} \left(\frac{\delta G(A^\alpha)}{\delta \alpha(x)} \right) = 1. \quad (\text{A.2})$$

¹³⁵⁶ Where $A_\mu^\alpha = A_\mu - \frac{1}{g_s} \partial_\mu \alpha(x)$. Making a gauge transformation ($A_\mu \rightarrow A_\mu^\alpha$) and inserting
¹³⁵⁷ equation (18):

$$\int DA e^{-\frac{i}{4} \int d^4x F_{\mu\nu}^a F^{a\mu\nu}} = \int DA \int D\alpha(x) \delta(G(A^\alpha)) \text{Det} \left(\frac{\delta G(A^\alpha)}{\delta \alpha(x)} \right) e^{-\frac{i}{4} \int d^4x F_{\mu\nu}^a F^{a\mu\nu}}, \quad (\text{A.3a})$$

$$= \int D\alpha(x) \int DA \delta(G(A^\alpha)) \text{Det} \left(\frac{\delta G(A^\alpha)}{\delta \alpha(x)} \right) e^{-\frac{i}{4} \int d^4x F_{\mu\nu}^a F^{a\mu\nu}}. \quad (\text{A.3b})$$

¹³⁵⁸ We are free to change the functional integration variable to A_μ^α since everything is gauge
¹³⁵⁹ invariant leading to an integrand which *only* depends on A_μ^α . We can therefore simply

1360 relabel back to A_μ :

$$= \left(\int D\alpha(x) \right) \int DA \delta(G(A)) \text{Det} \left(\frac{\delta G(A)}{\delta \alpha(x)} \right) e^{-\frac{i}{4} \int d^4x F_{\mu\nu}^a F^{a\mu\nu}}. \quad (\text{A.4})$$

1361 The functional integration can now just be factored out as a constant and we can choose
1362 the function $G(A)$ as a generalisation of the Lorentz gauge: $G(A) = \partial^\mu A_\mu^a - \omega^a$. This
1363 choice leads us to the correct gluon propagator - along with our free parameter, ξ :

$$\langle 0 | A_a(x) A_b(y) | 0 \rangle = G_F^{\mu\nu}(x-y) = \int \frac{d^4x}{(2\pi)^4} e^{-ik \cdot (x-y)} \delta_{ab} \frac{-i}{k^2 + i\epsilon} \left(g^{\mu\nu} - (1-\xi) \frac{k^\mu k^\nu}{k^2} \right). \quad (\text{A.5})$$

1364 but because the QCD gauge transformation is more involved than the QED equivalent
1365 the determinant term still depends on A_μ :

$$\text{Det} \left(\frac{\delta G(A)}{\delta \alpha(x)} \right) = \text{Det} \left(\frac{\partial_\mu D^\mu}{g_s} \right). \quad (\text{A.6})$$

1366 We can however simply invent another type of field and choose to write out determinant
1367 as

$$\text{Det} \left(\frac{\delta G(A)}{\delta \alpha(x)} \right) = \int D\chi D\bar{\chi} e^{i \int d^4x \bar{\chi} (-\partial_\mu D_\mu) \chi}. \quad (\text{A.7})$$

1368 These non-physical modes are called the Faddeev-Popov ghosts/anti-ghosts and are a
1369 consequence of enforcing gauge invariance - they are represented by the final term in
1370 equation (12a).

¹³⁷¹ Bibliography

- 1372 [1] AAD, G., ET AL. Measurement of dijet production with a veto on additional central jet
1373 activity in pp collisions at $\sqrt{s} = 7$ TeV using the ATLAS detector. *JHEP* 09 (2011), 053.
- 1374 [2] AAD, G., ET AL. Measurement of the production cross section for Z/γ^* in association
1375 with jets in pp collisions at $\sqrt{s} = 7$ TeV with the ATLAS detector. *Phys. Rev. D* 85 (2012),
1376 032009.
- 1377 [3] AAD, G., ET AL. Measurement of the production cross section of jets in association with
1378 a Z boson in pp collisions at $\sqrt{s} = 7$ TeV with the ATLAS detector. *JHEP* 1307 (2013),
1379 032.
- 1380 [4] AAD, G., ET AL. A measurement of the ratio of the production cross sections for W and
1381 Z bosons in association with jets with the ATLAS detector. *Eur. Phys. J. C* 74, 12 (2014),
1382 3168.
- 1383 [5] AAD, G., ET AL. Measurements of jet vetoes and azimuthal decorrelations in dijet events
1384 produced in pp collisions at $\sqrt{s} = 7$ TeV using the ATLAS detector. *Eur. Phys. J. C* 74,
1385 11 (2014), 3117.
- 1386 [6] AAD, G., ET AL. Measurements of the W production cross sections in association with
1387 jets with the ATLAS detector. *Eur. Phys. J. C* 75, 2 (2015), 82.
- 1388 [7] AAD, G., ET AL. Search for high-mass diboson resonances with boson-tagged jets in
1389 proton-proton collisions at $\sqrt{s} = 8$ TeV with the ATLAS detector. *JHEP* 12 (2015), 055.
- 1390 [8] ABAZOV, V. M., ET AL. Studies of W boson plus jets production in $p\bar{p}$ collisions at
1391 $\sqrt{s} = 1.96$ TeV. *Phys. Rev. D* 88, 9 (2013), 092001.
- 1392 [9] ALIOLI, S., NASON, P., OLEARI, C., AND RE, E. A general framework for implementing
1393 NLO calculations in shower Monte Carlo programs: the POWHEG BOX. *JHEP* 06 (2010),
1394 043.
- 1395 [10] ALIOLI, S., NASON, P., OLEARI, C., AND RE, E. Vector boson plus one jet production
1396 in POWHEG. *JHEP* 01 (2011), 095.
- 1397 [11] ALWALL, J., ET AL. Comparative study of various algorithms for the merging of parton
1398 showers and matrix elements in hadronic collisions. *Eur. Phys. J. C* 53 (2008), 473–500.
- 1399 [12] ALWALL, J., FREDERIX, R., FRIXIONE, S., HIRSCHI, V., MALTONI, F., MATTELAER,
1400 O., SHAO, H. S., STELZER, T., TORIELLI, P., AND ZARO, M. The automated
1401 computation of tree-level and next-to-leading order differential cross sections, and their
1402 matching to parton shower simulations. *JHEP* 07 (2014), 079.
- 1403 [13] ALWALL, J., HERQUET, M., MALTONI, F., MATTELAER, O., AND STELZER, T.
1404 MadGraph 5 : Going Beyond. *JHEP* 06 (2011), 128.

BIBLIOGRAPHY

- 1405 [14] ANDERSEN, J. R., LONNBLAD, L., AND SMILLIE, J. M. A Parton Shower for High Energy
1406 Jets. *JHEP* 07 (2011), 110.
- 1407 [15] ANDERSEN, J. R., AND SMILLIE, J. M. Constructing All-Order Corrections to Multi-Jet
1408 Rates. *JHEP* 1001 (2010), 039.
- 1409 [16] ANDERSEN, J. R., AND SMILLIE, J. M. The Factorisation of the t-channel Pole in Quark-
1410 Gluon Scattering. *Phys.Rev. D81* (2010), 114021.
- 1411 [17] ANDERSSON, B., MOHANTY, S., AND SODERBERG, F. Recent developments in the Lund
1412 model. In *36th Annual Winter School on Nuclear and Particle Physics (PINP 2002)*
1413 and *8th St. Petersburg School on Theoretical Physics St. Petersburg, Russia, February*
1414 *25-March 3, 2002* (2002).
- 1415 [18] BALITSKY, I., AND LIPATOV, L. The Pomeranchuk Singularity in Quantum
1416 Chromodynamics. *Sov.J.Nucl.Phys.* 28 (1978), 822–829.
- 1417 [19] BERGER, C. F., BERN, Z., DIXON, L. J., FEBRES CORDERO, F., FORDE, D.,
1418 GLEISBERG, T., ITA, H., KOSOWER, D. A., AND MAITRE, D. Next-to-Leading Order
1419 QCD Predictions for $Z, \gamma^* + 3$ -Jet Distributions at the Tevatron. *Phys. Rev. D82* (2010),
1420 074002.
- 1421 [20] BERINGER, J., ET AL. Review of Particle Physics (RPP). *Phys. Rev. D86* (2012), 010001.
- 1422 [21] BERN, Z., OZEREN, K., DIXON, L. J., HOECHE, S., FEBRES CORDERO, F., ITA, H.,
1423 KOSOWER, D., AND MAITRE, D. High multiplicity processes at NLO with BlackHat and
1424 Sherpa. *PoS LL2012* (2012), 018.
- 1425 [22] BUTTERWORTH, J. M., DAVISON, A. R., RUBIN, M., AND SALAM, G. P. Jet substructure
1426 as a new Higgs search channel at the LHC. *Phys. Rev. Lett.* 100 (2008), 242001.
- 1427 [23] CACCIARI, M., DREYER, F. A., KARLBERG, A., SALAM, G. P., AND ZANDERIGHI,
1428 G. Fully Differential Vector-Boson-Fusion Higgs Production at Next-to-Next-to-Leading
1429 Order. *Phys. Rev. Lett.* 115, 8 (2015), 082002.
- 1430 [24] CACCIARI, M., SALAM, G. P., AND SOYEZ, G. The Anti-k(t) jet clustering algorithm.
1431 *JHEP* 0804 (2008), 063.
- 1432 [25] CAMPBELL, J. M., ELLIS, R. K., NASON, P., AND ZANDERIGHI, G. W and Z bosons in
1433 association with two jets using the POWHEG method. *JHEP* 08 (2013), 005.
- 1434 [26] CAPORALE, F., IVANOV, D. Yu., MURDACA, B., AND PAPA, A. Mueller-Navelet small-
1435 cone jets at LHC in next-to-leading BFKL. *Nucl. Phys. B877* (2013), 73–94.
- 1436 [27] CHATRCHYAN, S., ET AL. Jet Production Rates in Association with W and Z Bosons in
1437 pp Collisions at $\sqrt{s} = 7$ TeV. *JHEP* 01 (2012), 010.
- 1438 [28] CHATRCHYAN, S., ET AL. Measurement of the inclusive production cross sections for
1439 forward jets and for dijet events with one forward and one central jet in pp collisions at
1440 $\sqrt{s} = 7$ TeV. *JHEP* 06 (2012), 036.
- 1441 [29] CHATRCHYAN, S., ET AL. Ratios of dijet production cross sections as a function of the
1442 absolute difference in rapidity between jets in proton-proton collisions at $\sqrt{s} = 7$ TeV.
1443 *Eur. Phys. J. C72* (2012), 2216.
- 1444 [30] CHATRCHYAN, S., ET AL. Event shapes and azimuthal correlations in $Z +$ jets events in
1445 pp collisions at $\sqrt{s} = 7$ TeV. *Phys. Lett. B722* (2013), 238–261.
- 1446 [31] CHATRCHYAN, S., ET AL. Measurement of the ratio of the inclusive 3-jet cross section to
1447 the inclusive 2-jet cross section in pp collisions at $\sqrt{s} = 7$ TeV and first determination of
1448 the strong coupling constant in the TeV range. *Eur. Phys. J. C73*, 10 (2013), 2604.

- 1449 [32] COLFERAI, D., SCHWENNSEN, F., SZYMANOWSKI, L., AND WALLON, S. Mueller Navelet
1450 jets at LHC - complete NLL BFKL calculation. *JHEP* **12** (2010), 026.
- 1451 [33] CORCELLA, G., KNOWLES, I. G., MARCHESEINI, G., MORETTI, S., ODAGIRI, K.,
1452 RICHARDSON, P., SEYMOUR, M. H., AND WEBBER, B. R. HERWIG 6: An Event
1453 generator for hadron emission reactions with interfering gluons (including supersymmetric
1454 processes). *JHEP* **01** (2001), 010.
- 1455 [34] DUCLOUE, B., SZYMANOWSKI, L., AND WALLON, S. Mueller-Navelet jets at LHC: the
1456 first complete NLL BFKL study. *PoS QNP2012* (2012), 165.
- 1457 [35] FIELD, R. *Applications of Perturbative Quantum Chromodynamics*. Addison Wesley
1458 Longman Publishing Co., 1989.
- 1459 [36] FREDERIX, R., FRIXIONE, S., PAPAEFSTATHIOU, A., PRESTEL, S., AND TORRIELLI, P.
1460 A study of multi-jet production in association with an electroweak vector boson.
- 1461 [37] FRIXIONE, S., NASON, P., AND OLEARI, C. Matching NLO QCD computations with
1462 Parton Shower simulations: the POWHEG method. *JHEP* **11** (2007), 070.
- 1463 [38] FRIXIONE, S., STOECKLI, F., TORRIELLI, P., WEBBER, B. R., AND WHITE, C. D. The
1464 MCaNLO 4.0 Event Generator.
- 1465 [39] FRIXIONE, S., AND WEBBER, B. R. Matching NLO QCD computations and parton
1466 shower simulations. *JHEP* **06** (2002), 029.
- 1467 [40] FROLOV, S., AND SLAVNOV, A. An invariant regularization of the standard model. *Physics
1468 Letters B* **309**, 3 (1993), 344 – 350.
- 1469 [41] GEHRMANN, T., GRAZZINI, M., KALLWEIT, S., MAIERHFER, P., VON MANTEUFFEL,
1470 A., POZZORINI, S., RATHLEV, D., AND TANCREDI, L. W^+W^- Production at Hadron
1471 Colliders in Next to Next to Leading Order QCD. *Phys. Rev. Lett.* **113**, 21 (2014), 212001.
- 1472 [42] GLEISBERG, T., HOECHE, S., KRAUSS, F., SCHONHERR, M., SCHUMANN, S., SIEGERT,
1473 F., AND WINTER, J. Event generation with SHERPA 1.1. *JHEP* **02** (2009), 007.
- 1474 [43] GRAZZINI, M., KALLWEIT, S., AND RATHLEV, D. W and Z production at the LHC in
1475 NNLO QCD. *JHEP* **07** (2015), 085.
- 1476 [44] GRIFFITHS, D. *Introduction to Elementary Particles*. Physics Textbook. Wiley, 2008.
- 1477 [45] HOECHE, S., KRAUSS, F., SCHONHERR, M., AND SIEGERT, F. QCD matrix elements +
1478 parton showers: The NLO case. *JHEP* **04** (2013), 027.
- 1479 [46] HCHE, S., KUTTIMALAI, S., SCHUMANN, S., AND SIEGERT, F. Beyond Standard Model
1480 calculations with Sherpa. *Eur. Phys. J. C* **75**, 3 (2015), 135.
- 1481 [47] ITA, H., BERN, Z., DIXON, L. J., FEBRES CORDERO, F., KOSOWER, D. A., AND
1482 MAITRE, D. Precise Predictions for Z + 4 Jets at Hadron Colliders. *Phys. Rev. D* **85**
1483 (2012), 031501.
- 1484 [48] JUNG, H., ET AL. The CCFM Monte Carlo generator CASCADE version 2.2.03. *Eur.
1485 Phys. J. C* **70** (2010), 1237–1249.
- 1486 [49] JUNG, H., AND SALAM, G. P. Hadronic final state predictions from CCFM: The Hadron
1487 level Monte Carlo generator CASCADE. *Eur. Phys. J. C* **19** (2001), 351–360.
- 1488 [50] KHACHATRYAN, V., ET AL. Measurement of electroweak production of two jets in
1489 association with a Z boson in proton-proton collisions at $\sqrt{s} = 8$ TeV. *Eur. Phys. J.
1490 C* **75**, 2 (2015), 66.

BIBLIOGRAPHY

- 1491 [51] KHACHATRYAN, V., ET AL. Measurements of jet multiplicity and differential production
1492 cross sections of $Z +$ jets events in proton-proton collisions at $\sqrt{s} = 7$ TeV. *Phys. Rev.*
1493 *D91*, 5 (2015), 052008.
- 1494 [52] KUIPERS, J., UEDA, T., VERMASEREN, J. A. M., AND VOLINGA, J. Form version 4.0.
1495 *CoRR abs/1203.6543* (2012).
- 1496 [53] KURAEV, E. A., LIPATOV, L. N., AND FADIN, V. S. Multi - Reggeon processes in the
1497 Yang-Mills theory. *Sov. Phys. JETP* 44 (1976), 443–450.
- 1498 [54] LAVESSON, N., AND LONNBLAD, L. W+jets matrix elements and the dipole cascade.
1499 *JHEP* 07 (2005), 054.
- 1500 [55] LONNBLAD, L. ARIADNE version 4: A Program for simulation of QCD cascades
1501 implementing the color dipole model. *Comput. Phys. Commun.* 71 (1992), 15–31.
- 1502 [56] MANGANO, M. L., MORETTI, M., PICCININI, F., PITTAU, R., AND POLOSA, A. D.
1503 ALPGEN, a generator for hard multiparton processes in hadronic collisions. *JHEP* 07
1504 (2003), 001.
- 1505 [57] MUTA, T. *Foundations Of Quantum Chromodynamics: An Introduction to Perturbative*
1506 *Methods in Gauge Theories*. World Scientific lecture notes in physics. World Scientific
1507 Publishing Company Incorporated, 2010.
- 1508 [58] NASON, P. A New method for combining NLO QCD with shower Monte Carlo algorithms.
1509 *JHEP* 11 (2004), 040.
- 1510 [59] PAULI, W., AND VILLARS, F. On the invariant regularization in relativistic quantum
1511 theory. *Rev. Mod. Phys.* 21 (Jul 1949), 434–444.
- 1512 [60] RE, E. NLO corrections merged with parton showers for $Z+2$ jets production using the
1513 POWHEG method. *JHEP* 10 (2012), 031.
- 1514 [61] SALAM, G. P., AND SOYEZ, G. A Practical Seedless Infrared-Safe Cone jet algorithm.
1515 *JHEP* 05 (2007), 086.
- 1516 [62] SJOSTRAND, T., EDEN, P., FRIBERG, C., LONNBLAD, L., MIU, G., MRENNA, S., AND
1517 NORRBIN, E. High-energy physics event generation with PYTHIA 6.1. *Comput. Phys.*
1518 *Commun.* 135 (2001), 238–259.
- 1519 [63] SJOSTRAND, T., MRENNA, S., AND SKANDS, P. Z. A Brief Introduction to PYTHIA 8.1.
1520 *Comput. Phys. Commun.* 178 (2008), 852–867.
- 1521 [64] STERMAN, G. F. Partons, factorization and resummation, TASI 95. In *QCD and beyond. Proceedings, Theoretical Advanced Study Institute in Elementary Particle Physics, TASI-95, Boulder, USA, June 4-30, 1995* (1995).

¹⁵²⁴ Publications

¹⁵²⁵

¹⁵²⁶ Author Name(s). Title of publication. In *Where Published*, Year.

¹⁵²⁷

¹⁵²⁸ Author Name(s). Title of publication. In *Where Published*, Year.

¹⁵²⁹